UNIVERSITY OF OKLAHOMA

GRADUATE COLLEGE

IV-VI LEAD SALT MID-INFRARED LIGHT EMITTING DEVICE DESIGN,

FABRICATION AND CHARACTERIZATION

A DISSERTATION

SUBMITTED TO THE GRADUATE FACULTY

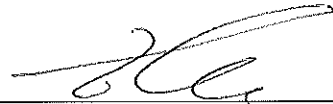in partial fulfillment of the requirements for the

Degree of

DOCTOR OF PHILOSOPHY
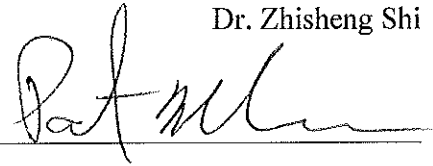
By

SHAIBAL MUKHERJEE
Norman, Oklahoma
2009

IV-VI LEAD SALT MID-INFRARED LIGHT EMITTING DEVICE DESIGN, FABRICATION AND CHARACTERIZATION

A DISSERTATION APPROVED FOR THE
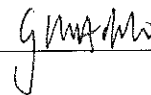## SCHOOL OF ELECTRICAL AND COMPUTER ENGINEERING

BY

_____

Dr. Zhisheng Shi

_____

Dr. Patrick J. McCann

_____

Dr. James J. Sluss

_____

Dr. Monty Tull

_____

Dr. George B. Richter-Addo

ACKNOWLEDGEMENTS

TABLE OF CONTENTS

LIST OF TABLES

LIST OF FIGURES

ABSTRACT

The research detailed by this dissertation has demonstrated the design, fabrication, and characterization of lead salt semiconductor mid-infrared light emitting devices. A scrupulous theoretical model has been described which estimates spectral gain from the quantum well (QW) structure based on IV-VI lead salt semiconductor material. The spectral gain of the QW structure, with both for finite and infinite well, for different crystal growth orientations is detailed. The purpose was to determine the best lead salt crystal orientation to fabricate opto-electronic devices.

Detailed experimental works concerning recent developments of IV-VI lead salt light emitting devices have been demonstrated. An electrically excited QW laser on [110] oriented lead salt substrate is reported for the first time in the literature. A brief description on the fabrications and characterizations of novel microstructures in the form of rod, tube and pillar, having enormous applications in MEMS and NEMS, is provided.

A theoretical exploration of spontaneous mid-infrared emission from IV-VI semiconductor photonic crystal defect microcavity is elaborated. The design is aimed to solve out challenges of the formation of resonating cavity for lead salt materials fabricated on Si(111) or BaF_2(111) substrates, commonly implemented to fabricate high temperature, continuous wave (CW) lasing devices. The band structure calculations of the periodic crystal are performed using plane wave expansion (PWE) method. Finite difference (FD) perturbation correction method and finite difference time domain

(FDTD) algorithms have been employed to analyze modal field distribution in the defect cavity.

A study on the measurement of minority carrier lifetime, which is one of the very important figures of merit to judge opto-electronic device performance, is illustrated. Photoconductive decay (PCD) method, a very popular and well-established methodology has been adopted to carry out the experimental work. The implementation of CaF_2 as a new surface passivation layer for MBE-grown PbSe single crystalline thin films on a $BaF_2(111)$ substrate has been done and the corresponding effect on device performance is compared. Minority carrier lifetimes and pulsed photoluminescence intensities from PbSe samples are observed to increase after CaF_2 surface passivation. However, the improvement is comparatively more significant at low temperature than at high temperature. This may indicate that surface passivation for Pb-salt materials are not as critical as its II-VI and III-V counterparts at high temperature of device operation. Therefore, device fabrication for Pb-salt materials at elevated temperature could be relatively more cost-effective with a higher-yield.

CHAPTER 1

INTRODUCTION

1.1.   Background

My doctoral research work is a perfect blend of theoretical and experimental study. It involved a broad spectrum of sub-topics in theoretical design and modeling of quantum wells (QWs), lasers and detectors and fabrication and characterization of real-time high-performance lead salt semiconductor mid-infrared optoelectronic devices. The crystal growth orientations of lead salt QWs play a crucial role in terms of achieving lower threshold characteristics which is extremely important to realize high temperature and long wavelength lasing devices. There is, at present, only a handful researchers working in lead salt materials in the world and no systematic study of complicated lead salt QWs for different crystal growth orientations is available in the literature. I undertook a scrupulous and extensive theoretical investigation for estimating the spectral gain from lead salt QWs for different growth orientations. In the course of identifying the influence of crystal orientation in QW behavior, I have studied a diverse set of sub-topics. Noteworthy among them are quantum well subband structure, spectral transitions associated with each of those subbands, quasi-Fermi energy level and density of states calculations, evaluation of overall QW spectral gain for different crystal orientations. I played a key role in the first successful fabrication of [110] oriented lead salt lasers and in the design of the first lead salt photonic crystal lasers on Si substrate.

Previously, it has been theoretically established by our opto-electronics group that the [110] growth orientation is the best crystal orientation for QW lead salt laser fabrication in terms of higher spectral gain and higher efficiency. But the numerical analysis was not accurate and was based on the approximation. However, there is a necessity to experimentally demonstrate the feasibility of a lasing cavity formation on a [110] oriented lead salt QW epitaxial layers. I took up the challenge and through a number of experimental studies, I could successfully demonstrate an electrically excited [110] lead salt QW laser for the first time in the literature. During this phase of work, through innovative ideas and comprehensive research, I could effectively fabricate various novel semiconductor microstructures in the form of solid rod, hollow tube and pillar, having massive applications in micro-electro-mechanical systems (MEMS) and nano-electro-mechanical systems (NEMS).

The most promising and popular growth substrate globally implemented to manufacture high temperature, and high power devices is silicon which has almost 78 times higher thermal conductivity than lead salt materials. Moreover, due to the fact that silicon can reduce manufacturing cost of device fabrication, it was extremely essential to tie up the already-established silicon technology with the lead salt technology to revolutionize the field of mid-infrared laser. However, the lasing cavity formation by means of cleaving mechanism is not feasible due to the dissimilarity in cleavage planes of silicon and lead salt materials. Thus, I have proposed and implemented the methodology of vastly popular photonic bandgap technique, by adopting which one do not need to undergo a cleaving process while making a Fabry-Perot laser resonating cavity. This part of my dissertation deals with the modeling and extensive numerical analysis of defect

microcavity lead salt photonic structure, for the first time in literature, by deploying two popular mathematical schemes - finite difference (FD) perturbation field correction method and finite difference time domain (FDTD) method.

The minority carrier lifetime is a key component influencing the opto-electronic properties of the semiconductors. In order to judge the epitaxial quality of MBE-grown samples, one needs to experimentally evaluate the carrier lifetime values. The final part of my research describes the appropriate foundation of the lifetime measurement set-up and innovative associated electrical circuit design. It is important to note here that the quality of thin film surface is tremendously vital from the fabrication and performance points of view of opto-electronic devices. Surface impurities on the exposed area of thin films degrade the semiconducting behavior of such devices. In order to alleviate the problem, I have proposed an idea, for the first time in literature, of implementing CaF_2 as a surface passivating layer for lead salt materials.

Research in the mid-infrared (MIR) optical spectral region (covering 2-30 μm wavelength region) has invoked a tremendous interest worldwide due to its wide-spread applications especially in the area of industrial chemical gas sensing[1]. Industrial hazardous and harmful gases like CO_2 (4.25μm), CO (4.6μm), CH_4 (3.3μm), N_2O (4.5μm), HF (2.52μm), O_3 (4.73μm) etc lie in this spectral zone and thereby necessitates the gas detection mandatory for health and safety concern. MIR light emitting devices are extensively employed for the monitoring of environmental pollution[2], industrial chemical processes, vehicle exhaust, and other harmful gases. Besides these, there are a number of other popular applications of these devices such as wireless point-to-point laser

communication at the atmospheric windows, laser surgery, non-invasive medical imaging, and military IR countermeasures. For all these purposes mainly for gas sensing applications, single-mode, electrically excited, tunable, continuous wave (CW) operation at thermo-electric cooler temperature with narrowest possible emission linewidth is desired. The gas sensing scheme is specifically based on allowing a very sharp and distinct laser light mode through the sample gas and the subsequent measurement of change in transmitted light intensity at IR photodetectors. Consequent light absorption is associated with the fundamental molecular vibration in the gas and this together with the sample gas parameters help to carry out quantitative analysis for a specific gas[3].

Various fabrication methodologies have been adopted to make these types of layered epitaxial structures. Liquid phase epitaxy (LPE) method was initially more widely used, followed by vacuum deposition techniques including vapor phase epitaxy (VPE), metal organic chemical vapor deposition (MOCVD), and molecular beam epitaxy (MBE). Among these methods, MBE has the unique advantage of epi-layer growth with precise and accurate control of layer composition and thickness. As a result of this precise control, MBE offered new opportunities for successful fabrication of micro- as well as nano-scale active layers, especially important in the development of quantum well (QW) lasers.

The fundamental reasoning behind designing QWs with thinner layers lies in the modification and confinement of electron and hole wave-functions, thereby modulating material parameters. As a basic criterion, QW lasers are capable of high optical gain even for a low current density. This is a direct consequence of (1) energy level quantization,

thereby lowering of the density of states in both the conduction and valence bands, and (2) increased carrier density due to the thinner layer structures as compared to the bulk crystal. The collection efficiency[4] of the carriers injected into the QWs also influences the optical gain. There are two primary types of QW structures proposed for improving both modal optical gain and collection efficiency: the single quantum well graded index separate confinement heterostructures (SQW-GRINSCH) and the multiple quantum well (MQW) structure[5].

The improvement of lead salt diode laser technology quickly followed III-V lasers. Lead salt materials, which constitute IV-VI binary compounds like PbS, PbSe, SrSe, SnSe, SnTe, PbTe etc, have a very small bandgap corresponding to emission inform the mid to far infrared, ranging from 3 - 30 μm. A tunable laser source is achieved as the bandgap energy is a strong function of ambient temperature, thus allowing the variation of emission wavelength in these materials, which is of utmost importance in ultrahigh resolution spectroscopy and gas sensing.

1.2.   State of the Art of MIR Semiconductor Laser

Emission in the mid-infrared (MIR) region of electromagnetic spectrum was observed in 1963, from III-V semiconductor materials (InAs and InSb) at wavelengths of 3.1 μm[6] and 5.3 μm[7]. In the following year, lasing emission from lead salt material (PbTe) was demonstrated at a higher wavelength[8]. In the next couple of decades, several MIR lasers were fabricated based on IV-VI lead chalcogenide materials such as PbS, PbTe, PbSe, PbSSe, PbSnTe, and PbSnSe etc.
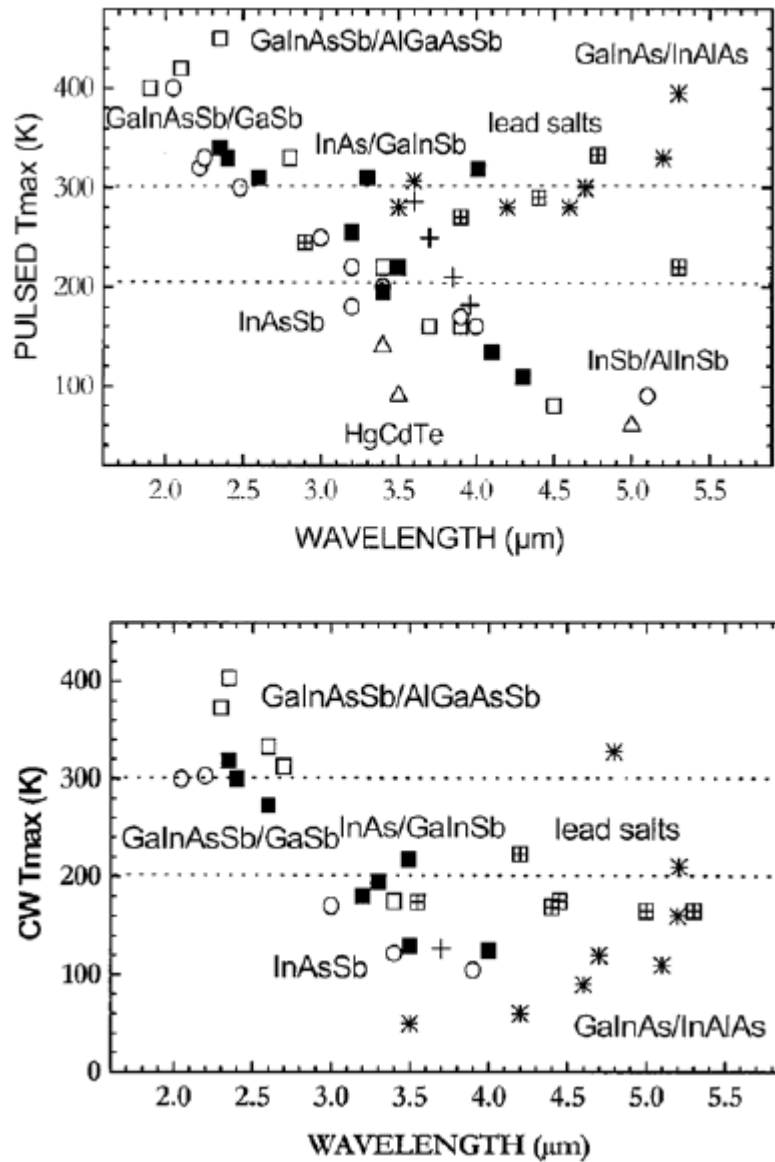
*Fig. 1.1: Maximum operating temperature of semiconductor laser diodes in the mid-IR; open circles: Sb-based DH lasers; open boxes: Sb-based type-I MQW lasers; solid boxes: Sb-based type-II MQW lasers; +: Sb-based type-II interband cascade lasers; *: GaInAs/AlInAs inter subband quantum cascade lasers; crossed box: lead salt lasers; open triangles: HgCdTe lasers[9].*

6

All these diode lasers were reported to be diffused diodes emitting in 4 – 30 μm wavelength range having the laser operation temperature of 4 – 77 K. With the advancement of epitaxial growth techniques, double heterostructures (DH) were fabricated. These structures brought in huge revolutions in the performance of lead salt lasers. Lead salt DH lasers served as the standard of MIR lasers till 1990. All these DH lasers were fabricated on lead salt substrates such as PbS, PbSe or PbTe, with active layers consisting of PbEuSSe for 3 – 4 μm[10], PbEuSeTe or PbEuSe for 4 – 8 μm range, and PbSnTe or PbSnSe for emission wavelengths beyond 8 μm. During that period, DH lasers based on III-V semiconductor materials were also gaining popularity as MIR light emitters. AlGaAsSb/GaInAsSb/AlGaAsSb DH lasers on fabricated on GaSb substrate and InAsPSb/InAsSb/InAsPSb DH lasers fabricated on InAs substrates demonstrated admirable performance at room temperature in the 2.0 - 2.5 μm wavelength range[11] [12]. The InGaAsSb/AlGaAsSb strained multiple quantum well (MQW) laser exhibited outstanding performance in continuous wave (CW) operation at and above room temperature with emission wavelength at 2.0 - 2.7 μm wavelength range[13]. Above 2.7 μm, GaSb-based type-II QW lasers[14] [15] [16], III-V quantum cascade (QC)[17] [18] [19] [20] [21], and IV-VI lead salt semiconductor lasers[22] [23] [24] [25] are the most promising approaches. Fig. 1.1 presents an overview of the current state of the art of MIR semiconductor lasers. The maximum operation temperatures in both the pulsed and CW modes of laser operation as a function of emission wavelengths are demonstrated in the figure.

1.3. Advantage of Lead Salt Materials in Opto-Electronic Applications

Table-1.1: Comparison of the current tuning range and linewidth of II-VI, III-V, and IV-VI semiconductors.

	III-V QC	Sb-based Type-II	**IV-VI Pb-salts**
dE/dT (cm^{-1}/K)	0.12	0.61	**2.76**
Current tuning range (cm^{-1})	1-2	N/A	**~ 30**
Line width (cm^{-1})	~some 10^{-3}	N/A	**10^{-4}**

Among all the leading approaches considered in making MIR lasers, IV-VI diode lasers are favorable candidates due to the following advantages populated in Table-1.1. Lead salts are direct bandgap semiconductors with nearly symmetric conduction and valence located at four equivalent L-valleys, displaying four-fold degeneracy within the Brillouin zone. Both the conduction band minima and valence band maxima exist as the center of the prolate ellipsoids of constant energy surfaces which are characterized by the longitudinal (m_l) and transverse (m_t) effective masses. Lead salt materials have a rock salt crystal structure and therefore have natural cleavage planes along {100}. Although they can also be grown along [111] and [110] orientations, these materials are usually grown on [100]-oriented substrates so as to have parallel facets along {100} acting as a Fabry-Perot cavity for the laser. The conduction and valence bands are non-parabolic, but at the L-points they are quite symmetric to each other, which in turn makes the difference between electron and hole effective mass almost negligible. With the use of $k \cdot p$ formalism[26], band structure calculations have been reported. The interaction between conduction and valence band edge levels is considered and the contribution of other distant bands is treated by higher order perturbation theory (popularly known as the six

band model). If the effect of distant bands is neglected, then the popular two-band model proposed by Kane is followed for evaluating the dispersion characteristics for these materials. While these materials are lead-salt, they do possess both ionic and covalent behavior; theoretical studies related to the bonding are discussed elsewhere[27]. The ternary and quaternary compounds of IV-VI materials are known to exist for all possible values of compositions of constituent elements. By varying the composition, one can easily achieve lattice constant variation which is of utmost significance for Pb-salt heterostructure multilayers consisting of lattice-matched epitaxial layers.

The lattice constants in these ternary and quaternary compounds are believed to obey Vegard's law[1]. Varying the QW widths, or layer thicknesses, and changing the operating temperatures can result in fine-tuning as is shown in Fig. 1.2 The temperature tuning coefficient is about five times larger than III-V materials. Unlike III-V materials, the energy bandgap of IV-VI materials increases with the temperature, and as a result, increasing the injection current will cause a blue-shift of both the gain peak and the energy band gap due to extra heating, resulting in the ease of laser emission tuning. Fig. 1.3 illustrates[28] the variation of lattice parameter with bandgap for various IV-VI semiconductor materials. The entire infrared spectral region from 3 μm to 20 μm is covered by compositional variation in these materials.
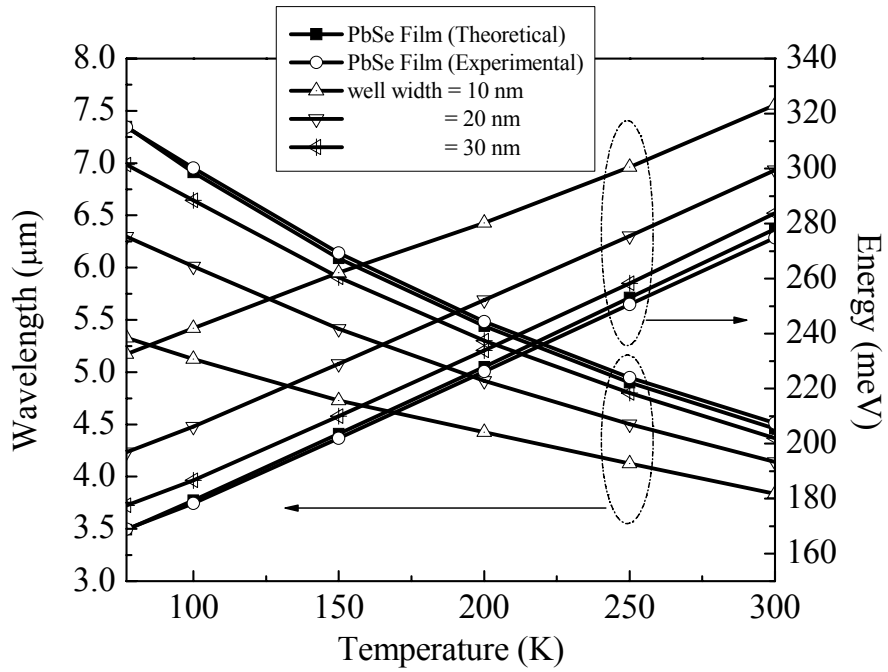
Fig. 1.2: Temperature dependent emission wavelengths of PbSe/PbSrSe QW structure.
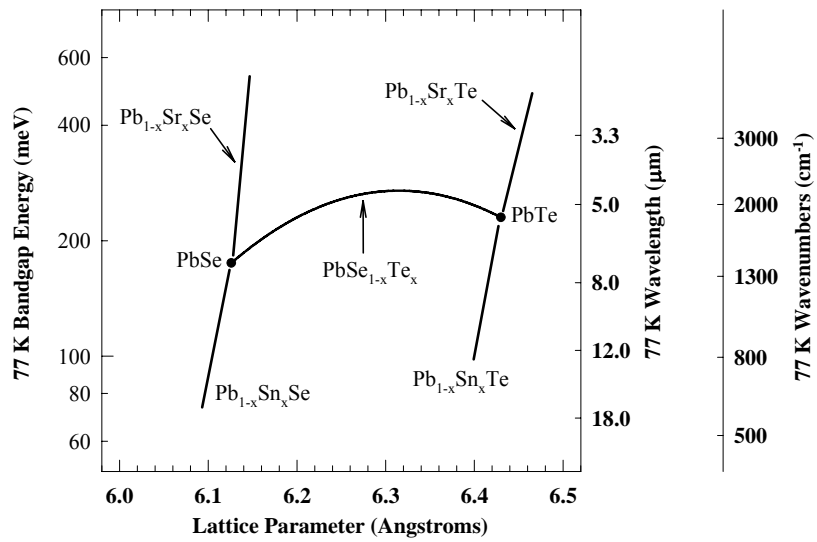
Fig. 1.3: Bandgap energy vs. lattice parameters of IV-VI materials. Source: P. J. McCann.

The lasing thresholds of commercially available lead salt lasers are considerably enhanced due to the existence of L-valley four-fold degeneracy both for conduction and valence bands. For conventional lead salt lasers, [100] growth orientation is most popular due to the ease of forming Fabry-Perot lasing cavity by cleaving. However, in case of [100] oriented edge-emitting QW lasers, the L-vally degeneracy does not get lifted. Thus, this crystal growth orientation is not quite suitable to realize high temperature and long wavelength lasing devices. In order to exploit the greatest advantage of IV-VI materials in terms of threshold reduction due to a low non-radiative recombination rate, one has to consider other feasible crystal growth orientations such as [111] and [110] orientations.

There has not been any systematic study of lead chalcogenide QWs for different crystal growth orientations. The prior theoretical study on QW gain conducted by our group had a basic limitation and therefore it requires an accurate and comprehensive study of QW gain for different crystal orientations. In this research work, a detailed numerical analysis of quantum sub-band structure and optical transitions associated with those subbands for overall QW gain calculation for different crystal growth orientations is presented.

In order to get rid of the existing challenges associated with the [100] orientation, the [110] growth orientation is chosen. Based on our group's prior knowledge, the [110] crystal orientation provides highest QW spectral gain. However, QW gain calculation conducted by our previous theoretical investigation was based on an assumption. Although for feasibility study, we attempted fabricating lasers on a [110]-oriented lead

salt substrates. Recently for the first time in the literature, electrically pumped pulsed lasing has been demonstrated on a [110] oriented PbSnSe substrate[29]. Novel chemo-mechanical polishing scheme for [110] oriented lead salt substrate required to make them epi-ready is reported. The fabrications of novel microstructures in the forms of pillars, tubes and rods which have vast applications in the field of micro-electromechanical systems (MEMS) and nano-electromechanical systems (NEMS) are detailed.

The best growth substrate for realizing high temperature devices is silicon (Si). Si has almost 78 times higher thermal conductivity than lead salt materials at 300 K. Also, by using Si one can reduce manufacturing cost of device fabrication as well as avail of the established device fabrication technologies on this substrate. However unlike lead salt materials, the natural cleavage plane for Si is (111). Therefore in order to fabricate lasing device, there is a necessity to adopt some valid technology which does not undergo a cleaving process while making a Fabry-Perot resonating cavity. The best solution in this regard is illustrated in Chapter 4 by implementing, for the first time in literature, the idea of well-known photonic bandgap (PBG) methodology, the physics of which does not depend on the crystal orientation.

Minority carrier lifetime is one of the very important figures of merit to judge the performance of opto-electronic devices such as lasers and detectors. Lifetime is one of the important parameters to judge the growth quality of lead salt materials grown by molecular beam epitaxy (MBE) method. This dissertation would detail the photoconductive decay (PCD) method, a very popular and well-established methodology

which is considered to experimentally measure minority carrier lifetime for lead salt material.

1.4. Thesis Contributions and Organization

The final goal of this research work is to realize lead salt mid-infrared light emitting devices mostly comprising quantum well (QW) structures on molecular beam epitaxy (MBE)-grown BaF_2 and Si substrates. In order to carry out the research, there is an obvious necessity to study the behavior and characteristics of IV-VI lead salt QW structures both theoretically as well as experimentally.

Chapter 2 would provide detailed study of lead salt QW behavior. The various QW parameters essential for device fabrication would be optimized. Commercial software modified to account for IV-VI materials has been devised to perform the theoretical study. Chapter 3 describes the first time achievement of electrically pumped QW lead salt MIR laser on a [110] oriented PbSnSe substrate. This chapter also details the successful fabrication of lead salt microstructures in the form pillars, rods, and tubes and their superior performances. Chapter 4 would provide a detailed investigation of PBG structure on lead salt materials. To the best of our knowledge this is the first time a defect microcavity PBG structure on lead salt materials is studied in literature. Chapter 5 describes a study on the measurement of minority carrier lifetime is described. PCD method has been considered to carry out the experimental work in this phase. The implementation of CaF_2 as a new surface passivation layer for MBE-grown PbSe single crystalline thin films on a $BaF_2(111)$ substrate has been done and the corresponding effect on device performance is compared. The purpose of this study is to investigate the

influence of surface passivation on the basic properties of semiconducting opto-electronic

devices including photoluminescence (PL) intensity and minority carrier lifetime.

1.5.   References

---

[1] P. C. Findlay, C. R. Pidgeon, R. Kotitschke, A. Hollingworth, B. N. Murdin, C. J. G. M. Langerak, A. F. G.van Der Meer, C. M. Ciesla, J. Oswald, A. Homer, G. Springholz, and G. Bauer, "Auger recombination dynamics of lead salts under picosecond free-electronlaser excitation," *Phys. Rev. B*, vol. 58, no. 19, pp. 12908-12915, 1998.

[2] Z. Feit, M. McDonald, R. J. Woods, V. Archambault, and P. Mak, "Low threshold PbEuSeTe/PbTe separate confinement buried heterostructures diode lasers," *Appl. Phys. Lett.*, vol. 68, no. 6, pp. 738-740, 1996.

[3] P. Werle, "A review of recent advances in semiconductor laser based gas monitors," Spectrochimica Acta A, vol. 54, pp. 197–238, 1998.

[4] S. R. Chinn, Jr. P. S. Zory, A. R. Reisinger, "A model for GRIN-SCH-SQW diode lasers," *IEEE J. Quant. Electron.*, vol. 24, pp. 2191-2214, 1988.

[5] J. P. Noblanc, "Trends in quantum well devices," *Surf. Sci.*, vol. 168, pp. 847-851, 1986.

[6] I. Melngailis, "Maser action in InAs diodes," *Appl. Phys. Lett.*, vol. 2, pp. 176-178, 1963.

[7] J. Phelan, A. R. Calawa, R. H. Rediker, R. J. Keyes, B. Lax, "Infrared InSb laser diode in high magnetic fields," *Appl. Phys. Lett.*, vol. 3, pp. 143-145, 1963.

[8] J. F. Butler, A. R. Calawa, R. J. Phelan, T. C. Harman, A. J. Strauss, R. H. Rediker, "PbTe diode laser," *Appl. Phys. Lett.*, vol. 5, pp. 75-77, 1964.

[9] C. Fischer and M. W. Sigrist, "Mid-IR Difference Frequency Generation," *Solid-State Mid-Infrared Laser Sources*, ed. I. T. Sorokina and K.L. Vodopyanov, Topics in Appl. Phys., vol. 89, pp. 97-140, Springer, 2003.

[10] D. L. Patin, C. M. Trush, "Wavelength coverage of lead-europium-selenide-telluride diode lasers," *Appl. Phys. Lett.*, vol. 45, pp. 193-195, 1984.

[11] C. Caneau, A. K. Srivastava, A. G. Dentai, J. L. Zyskind, M. A. Pollak, "Room-temperature GaInAsSb/AlGaAsSb DH injection lasers at 2.2 μm," *Electron. Lett.*, vol. 21, pp. 815-817, 1985.

[12] A.N. Baranov, T. N. Danilova, B. E. Dzhurtanov, A. N. Imenkov, S. G. KonM. Litvak, V. E. Umanskii, Yu. P. Yakovlev, "CW lasing in GaInAsSb/GaSb buried channel laser (T=20°C, λ=2.0 µm)," *Sov. Techn. Phys. Lett.*, vol. 14, pp. 727-729, 1988.

[13] A. Joullie, P. Christol, A. N. Barnov, and A. Vicet, "Mid-infrared 2-5 µm heterojunction laser diodes," *Solid-State Mid-Infrared Laser Sources*, ed. I. T. Sorokina and K.L. Vodopyanov, Topics in Appl. Phys., vol. 89, pp. 1-59, Springer, 2003.

[14] W. W. Bewley, I. Vurgaftman, C. S. Kim, M. Kim, C. L. Canedy, J. R. Meyer, J. D. Bruno, F. J. Towner, "Room-temperature "W" diode lasers emitting at λ ≈ 4.0 µm," *Appl. Phys. Lett.*, vol. 85, pp. 5544-5546, 2004.

[15] R. Q. Yang, C. J. Hill, B. Yang, J. K. Liu, "Room-temperature type-II interband cascade lasers near 4.1 µm," *Appl. Phys. Lett.*, vol. 83, pp. 2109-2111, 2003.

[16] R. Kaspi, A. Ongstad, G. C. Dente, J. Chavez, M. L. Tilton, D. Gianardi, "High power and high brightness from an optically pumped InAs/InGaSb type-II midinfrared laser with low confinement," *Appl. Phys. Lett.*, vol. 81, pp. 406-408, 2002.

[17] A. Evans, J. S. Yu, S. Slivken, M. Razeghi, "Continuous-wave operation of λ ~ 4.8 µm quantum-cascade lasers at room temperature," *Appl. Phys. Lett.*, vol. 85, pp. 2166-2168, 2004.

[18] A. Evans, J. S. Yu, J. David, L. Doris, K. Mi, S. Slivken, M. Razeghi, "High-temperature, high-power, continuous-wave operation of buried heterostructure quantum-cascade lasers," *Appl. Phys. Lett.*, vol. 84, pp. 314-316, 2004.

[19] M. Troccoli, D. Bour, S. Corzine, G. Hofler, A. Tandon, D. Mars, D. J. Smith, L. Diehl, F. Capasso, "Low-threshold continuous-wave operation of quantum-cascade lasers grown by metalorganic vapor phase epitaxy," *Appl. Phys. Lett.*, vol. 85, pp. 5842-5844, 2004.

[20] D. P. Xu, A. Mirabedini, M. D'Souza, S. Li, D. Botez, A. Lyakh, Y. -J. Shen, P. Zory, C. Gmachl, "Room-temperature, mid-infrared (λ=4.7µm) electroluminescence from single-stage intersubband GaAs-based edge emitters," *Appl. Phys. Lett.*, vol. 85, pp. 4573-4575, 2004.

[21] T. Aellen, S. Blaser, M. Beck, D. Hofstetter, J. Faist, E. Gini, "Continuous-wave distributed-feedback quantum-cascade lasers on a Peltier cooler," *Appl. Phys. Lett*., vol. 83, pp. 1929-1931, 2003.

[22] D. L. Partin, "Lead salt quantum well structures," *IEEE J. Quant. Electron*., vol. 24, pp. 1716-1726, 1988.

[23] M. Tacke, "New developments and applications of tunable IR lead salt lasers," *Infrared. Phys. Technol.*, vol. 36, pp. 447-463, 1995.

[24] Z. Shi, G. Xu, P. J. McCann, X. M. Fang, N. Dai, C. L. Felix, W. W. Bewley, I. Vurgaftman, J. R. Meyer, "IV-VI compound midinfrared high-reflectivity mirrors and vertical-cavity surface-emitting lasers grown by molecular-beam epitaxy," *Appl. Phys. Lett.*, vol. 76, pp. 3688-3690, 2000.

[25] Z. Shi, X. Lv, F. Zhao, A. Majumdar, D. Ray, R. Singh, X. J. Yan, "[110] Orientated Lead Salt Mid-Infrared Lasers," *Appl. Phys. Lett*., vol. 85, pp. 2999-3001, 2004.

[26] J. O. Dimmock, In *The physics of semimetals and narrow gap semiconductors*, D. L. Carter, R. T. Bate, Ed.; Supplement no 1 to the Journal of physics and chemistry of solids; Pergamon Press: Oxford, NY, vol. 32, pp. 1-568, 1971.

[27] A. L. Hagstrom, A. Fahlman, "The electronic structure of PbSe and its interaction with O_2 adsorbate layers," *Phys. Scr*., vol. 16, pp. 432-4355, 1977.

[28] P. J. McCann, H. Wu, N. Dai, "Growth and Characterization of IV-VI Semiconductor Multiple Quantum Well Structures," http://www.coe.ou.edu/sserg/, 2002.

[29] S. Mukherjee, D. Li, D. Ray, F. Zhao, S. L. Elizondo, S. Jain, J. Ma, Z. Shi, "Fabrication of an Electrically Pumped Lead-Chalcogenide Mid-Infrared Laser on a [110] Oriented PbSnSe Substrate," *IEEE Photon. Technol. Lett*., vol. 20, pp. 629-631, 2008.

CHAPTER 2

SPECTRAL GAIN CALCULATION FOR IV-VI QW STRUCTURE

2.1. Introduction

There has been tremendous advancement in the field of thin film fabrication technology due to the continuous progress and development of semiconductor growth techniques of molecular beam epitaxy (MBE). These advancements have greatly facilitated the fabrication of thin and well-controlled hetero-structures[1] with mono-atomic layer precision[2]. Based on early growths by MBE, various opto-electronic devices, namely field effect transistors (FETs), high-frequency oscillators, photo detectors, quantum well lasers were proposed. In most of these devices, carrier flow is allowed in two directions perpendicular to the growth direction. The confinement in the growth direction is generally provided by a well-restricted space. The two-dimensional (2D) flow of carriers is best exploited by QW lasers which generate high emission power with a low threshold level. The most popular QW structures are single quantum well (SQW), multiple quantum well (MQW), separate confinement hetero-structure single quantum well (SCH-SQW), and separate confinement hetero-structure multiple quantum well (otherwise known as "modified" MQW).

SQW   *MQW*

SCH-SQW   *"Modified" MQW*
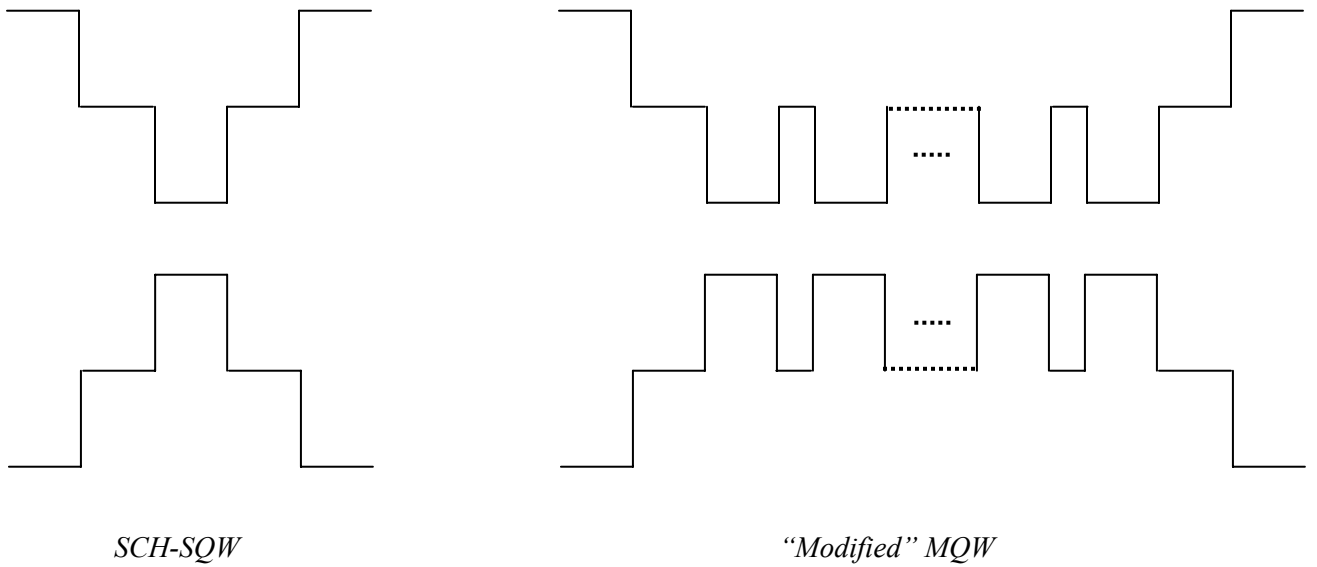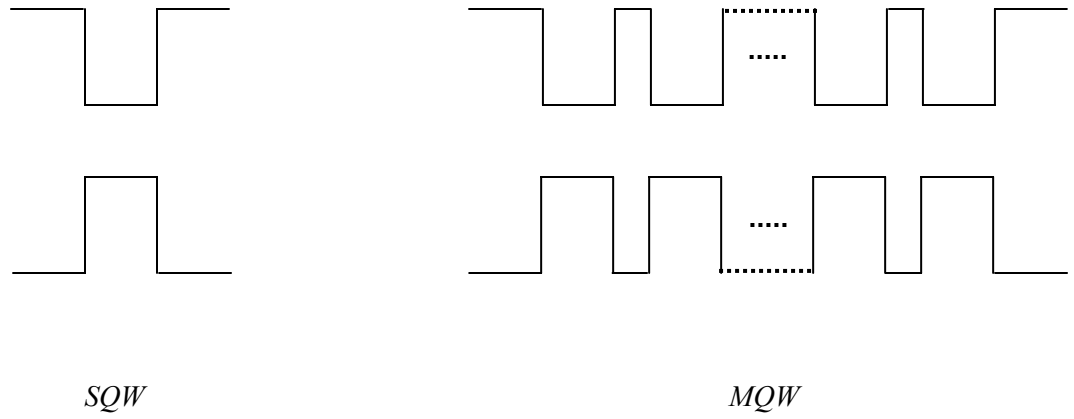
Fig. 2.1: Commonly used band alignment for quantum well structures.

2.1.1. Mathematical Analysis of Single QW Structure

In our simulation, we would consider basic SQW structure made up of PbSe active region sandwiched between two PbSrSe barrier layers. The APSYS software, a product of CROSSLIGHT Inc., has been used to carry out numerical simulations for QW structure. The general description of the QW theory used in our simulation is given in the

following. The specific details about how it applies, however, are available in the APSYS reference manual.

The basic quantum structure is comprised of a single epitaxial layer of material X sandwiched between two epi-layers of another material Y. Fig. 2.2 demonstrates the material Y has larger bandgap compared to that of X, and it has been presumed that the band discontinuities between these two materials confine carriers in material X. In this way, material X is a potential well for carriers and material Y is a potential barrier. Blue curves in Fig. 2.2 represent quasi-Fermi energy levels in the conduction and valence bands where green curves are quantum waves associated with individual subband energy level. The electron wave function can be expressed as

$$\psi = \sum_{X,Y} \exp(i\kappa_\perp . r) V_\kappa(r) \chi_n(z) \tag{2.1}$$

where $V_\kappa(r)$ is the Bloch wave function in the system, z is the vertical growth direction, $\chi_n(z)$ is the envelope wave function, $\kappa_\perp$ is the electron wave vector in the vertical direction. Envelope wave function, which is essential in calculating energy levels in the band structure, can be approximated[2] by

$$\left(-\frac{\hbar^2}{2m_{eff}(z)} \frac{\partial^2}{\partial z^2} + U(z) \right) \chi_n(z) = E_n \chi_n(z) \tag{2.2}$$

where $U(z)$ represents potential energy associated with carriers in the z-direction, $m_{eff}(z)$ is the effective carrier mass, E_n is the carrier confinement energy. The left hand side of equation (2.2) is sometimes written as $H\chi_n(z)$ where H is designated as the *Hamiltonian*

operator. The *Hamiltonian operator* (*H*) is directly related to the kinetic energy of electron. The basic conditions for the conservation of particle current[3] are that both $\chi_n(z)$ as well as $[1/m_{eff}(z)][\partial \chi_n(z)/ \partial z]$ should be continuous. The single potential well is illustrated in Fig. 2.3(a). The quantized energy level in the potential well together with the associated wave functions can be determined from the solution of the Schrödinger-like equation (2.2).
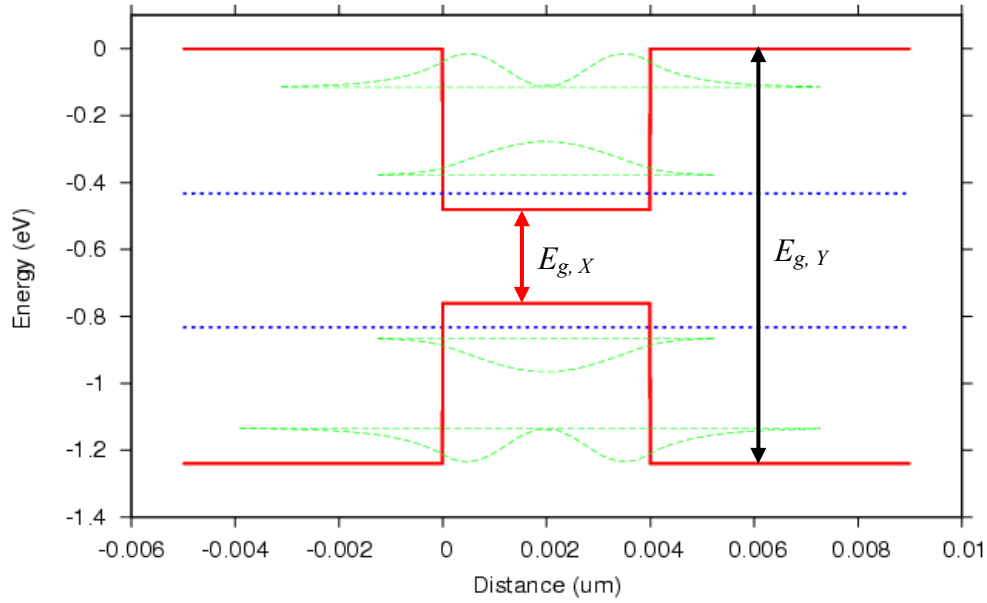
Fig. 2.2: Example of a single quantum well structure with corresponding quasi Fermi levels and quantum wave functions.

The solutions can be either even or odd based on the inversion symmetry at *z*=0. The solutions can be cited as

$$\begin{aligned}
\chi_n(z) &= X \cos kz, & \text{for } |z| &< w/2 \\
&= Y \exp[-\kappa(z - w/2)], & \text{for } z &> w/2 \\
&= Y \exp[+\kappa(z + w/2)], & \text{for } z &< -w/2
\end{aligned} \tag{2.3}$$

21

or

$$\chi_n(z) = \sin \kappa z, \qquad\qquad for \ |z| < w/2$$
$$= B\exp[-\kappa(z - w/2)], \quad for \ z > w/2$$
$$= B\exp[+\kappa(z + w/2)], \quad for \ z < -w/2$$

(2.4)

where

$$k = \frac{\sqrt{2m_{eff,well}E_n}}{\hbar}, \qquad \kappa = \frac{\sqrt{2m_{eff,barrier}(U_0 - E_n)}}{\hbar}, \qquad 0 < E_n < U_0$$

(2.5)

and effective carrier masses in the well as well as barrier can be designated as $m_{eff,well}$ and $m_{eff,barrier}$ respectively. k and κ are wave vectors parallel to the growth direction and U_0 represents the well depth. The energy levels in the band diagram are then evaluated from the following equations

$$\frac{m_{eff,barrier}}{m_{eff,well}} \tan\left(\frac{kw}{2}\right) = \frac{\kappa}{k},$$

(2.6)

and

$$\frac{m_{eff,barrier}}{m_{eff,well}} \cot\left(\frac{kw}{2}\right) = -\frac{\kappa}{k}$$

(2.7)

The above equations (2.6) and (2.7) can be solved to obtain conduction energy levels for electrons and valence energy levels for holes.

2.1.2. Energy Level Formulation for Single QW

Equations (2.6) and (2.7) representing energy levels in the single quantum well structure contain effective mass value of carriers that are independent of energy. The values of the effective masses are at the band extrema. There are two popular methods commonly deployed in calculating energy levels[4] in the quantum well. The first method uses Luttinger-Kohn "energy independent effective mass" calculation as

$$\{E_z(k) + U_0\}\chi = E_n\chi \tag{2.8}$$

where $E_z(k)$ designates energy dispersion in the periodic lattice at equivalent conditions and this following Kane's model[5] can be mathematically expressed for the conduction band by

$$E_z(k) = \frac{\hbar^2 k^2}{2m_{eff,well}}\left(1 - \gamma k^2\right) \tag{2.9}$$

$$\Rightarrow \quad k^2 = 0.5 \times \frac{\left[1 - \sqrt{1 - 8\gamma E_z m_{eff,well}/\hbar^2}\right]}{\gamma} \tag{2.10}$$

where γ is the system coefficient under investigation. The value of k from equation (2.10) is used in equations (2.6) and (2.7) to calculate energy levels.

The second one is known as "energy dependent effective mass" method. Here, the non-parabolicity nature of the conduction and valence bands are taken into account. The numerical results obtained by this approach are similar to the first one except the energy

dependent effective mass, which is used in equations (2.2), is expressed by the following

expression

$$m_{eff}(E_z) = \frac{\hbar^2 k}{\partial E_z(k)/\partial k}$$ (2.11)

2.1.3. Energy Level Formulation for Periodic QW

A periodic quantum well structure (as in Fig. 2.3(b)) can be thought of as an

accumulation of an array of potential wells or SQWs sequentially arranged in the growth

direction. Due to the quantization of electron and hole energy levels, a number of

subband levels are generated in the band structure. This, however, helps in the splitting of

single energy level. The distance in eV between the top and bottom energy levels of a

single subband is designated as energy broadening (ΔE). For a specific quantum well, the

energy broadening (ΔE) strongly depends on barrier height and thickness. There is

another important parameter associated with the quantization of carriers in the bands in

MQW structure; this is known as carrier coupling. A large coupling between carriers

improves the device performance. However, the two-dimensional (2D) nature of the

quantum well degrades with increasing coupling values due to deformation of the density

of states (DOS). Therefore to maintain both the 2D character of the quantum well as well

as a uniform carrier distribution, the following equation[6][7] is followed

$$\frac{\hbar}{\tau_{rec}} << \Delta E << \frac{\hbar}{\tau_{irt}}$$ (2.12)

where τ_{rec} is the recombination time for carrier during the occurrence of stimulated

emission from the material and τ_{irt} is the intraband relaxation time.

As in Fig. 2.3(b), the lattice constant of the periodic potential well is $a = b + w$. The periodicity in the potential well can be demonstrated as

$$U(z) = U(z + a) = U(z + 2a) = ...$$ (2.13)

The energy levels in the periodic well are obtained by solving the equation (2.2) both inside ($-b < z < 0$) and outside ($0 \leq z \leq w$) the potential well. The solutions would be as follows

$$\chi_n(z) = A\exp[i(k - m)z] + B\exp[-i(k + m)z], \qquad 0 \leq z \leq w$$ (2.14)

$$\chi_n(z) = C\exp[(\kappa - im)z] + B\exp[-(\kappa + im)z], \qquad -b < z < 0$$ (2.15)

where A, B, C, D are arbitrary constants and $m = 2\pi/\lambda$, where λ is the de Broglie wavelength.

(a)   (b)
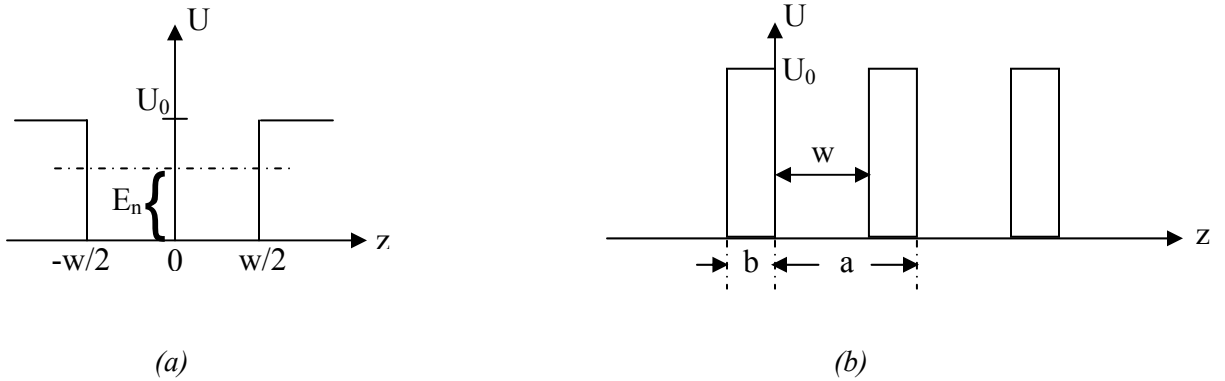
Fig. 2.3: (a) Single symmetric square quantum well, (b) periodic quantum well according to Kronig-Penney model.

2.2.   Energy Levels in PbSe/PbSrSe SQW Structure

PbSe or PbSrSe are direct bandgap semiconductors where band minima exist at four equivalent L-valley points of the Brillouin zone (as shown in Fig. 2.4). The constant energy surfaces which are elliptical in nature have major axes in the [111] direction. The dispersion relation both for the conduction as well as the valence bands for the lead salt material can be written with the help of Kane's model[8] as

$$E = -0.5E_g \pm \sqrt{0.25E_g^2 + P_t^2 k_t^2 + P_l^2 k_l^2} \qquad (2.16)$$

where the positive (+) sign stands for the conduction band and negative (-) stands for the valence band. The origin of the energy level is considered at the bottom of the conduction band for the lead salt material with a bandgap of E_g. k_t and k_l are the transverse and longitudinal wave vectors respectively where P_t^2 and P_l^2 are the transverse and longitudinal momentum matrix elements which are related with the effective masses m_t and m_l by the following equation[8]

$$P_{l,t}^2 = \frac{\hbar^2 E_G}{2m_{l,t}} \qquad (2.17)$$
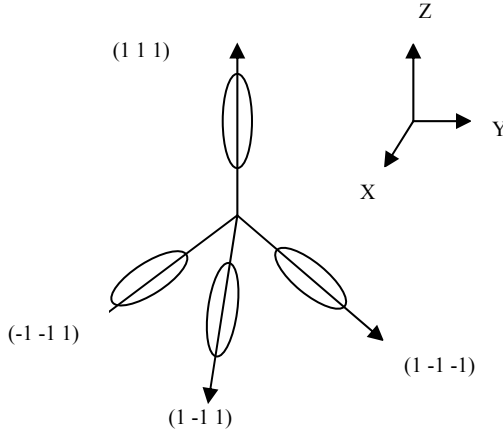
Fig. 2.4: Illustration of IV-VI material L-valley energy minima.

Equation (2.17) shows a direct relationship between the bandgap and effective mass of the lead salt material. The change in the energy bandgap with composition (x) and temperature (T) is therefore reflected in the change in effective mass[9]. The energy and wave vector relation along the growth (z) direction is similarly depicted following equation (3.16) by

$$E_z = -0.5E_g \pm \sqrt{0.25E_g^2 + P_z^2 k^2} \qquad (2.18)$$

where $P_z^2 = \dfrac{\hbar^2 E_g}{2m_{well}}$. From equations (2.16) and (2.18), the relation between wave vector (k) with its transverse and longitudinal components can be written as

$$\frac{k^2}{m_{well}} = \frac{k_l^2}{m_l} + \frac{k_t^2}{m_t} \qquad (2.19)$$

k_l and k_t can be represented in terms of k as

$$\begin{aligned} k_l &= k\cos\theta \\ k_t &= k\sin\theta \end{aligned} \qquad (2.20)$$

27

where θ is the angle between the growth direction and major axis of the elliptical constant energy surfaces. From the previous two equations (2.19) and (2.20), one can obtain

$$\frac{1}{m_{well}} = \frac{\cos^2\theta}{m_l} + \frac{\sin^2\theta}{m_t} \tag{2.21}$$

Therefore, the dispersion relation in the growth (z) direction can be represented as

$$E_z = -0.5E_g \pm \sqrt{0.25E_g^2 + \frac{\hbar^2 E_g}{2m_{well}}k^2} \tag{2.22}$$

The value of m_{well} used in this formula is taken from equation (2.21). Dispersion relation near conduction and valence band edge can be simplified by expanding the term under square root in equation (2.22) up to the 2nd order of wave vector (k) and can be written as

$$E_z = \frac{\hbar^2 k^2}{2m_{well}} \tag{2.23}$$

The above equation demonstrates parabolic dispersion relation for lead chalcogenide materials in the z-direction ($k_\perp = 0$). Although dispersion (E-k) relation away from the band edge is strongly non-parabolic in nature. This non-parabolicity in the distant energy bands is considered by taking higher order terms of k into account. For example, the E-k relation comprising of 4th order terms of wave vector can be given as

$$E_z = \frac{\hbar^2 k^2}{2m_{well}}\left(1 - \frac{\hbar^2 k^2}{2m_{well}E_g}\right) \tag{2.24}$$

28

both for the conduction as well as valence bands. The origin of the energy axis is taken at the energy minima and maxima of conduction and valence band respectively.

In case of the parabolic band, the effective mass is considered to be independent of energy. However, to deal with non-parabolic bands two approaches are generally utilized: the energy dependence of effective mass and the Luttinger-Kohn method. By the first approach, of the energy dependencies can be calculated by using equations (2.11) and (2.22) as shown below

$$m_{well}\left(E_z\right) = m_{well}\left(1 + \frac{2E_z}{E_G}\right) \tag{2.25}$$

The second method i.e. the Luttinger-Kohn approach necessitates the value for the system parameter γ as can be seen in equations (2.9) and (2.10). The value of γ is easily obtained from equations (2.9) and (2.24) and is written as

$$\gamma = \frac{\hbar^2}{2m_{well}E_G} \tag{2.26}$$

Thus dispersion relation in this case can be evaluated from equations (2.10) and (2.26) and this is given by

$$k = \sqrt{\frac{m_{well}E_g\left(1 - \sqrt{1 - 4E_z/E_g}\right)}{\hbar^2}} \tag{2.27}$$

The real value of wave vector is obtained as long as $\sqrt{1 - 4E_z/E_g} \geq 0$, which on the other hand limits the dispersion calculation up to a maximum energy level of ¼ E_g. The

limitation for this is caused because the derivation of Luttinger-Kohn equation (2.8) is based on 2nd order perturbation theory[4]. The limitation can be lifted by determining the dispersion relation for higher order of wave vector as elaborated elsewhere[10].

2.3.   Characteristics of IV-VI Materials

The knowledge of barrier potential (U_0), effective masses of well (m_{well}) and barrier ($m_{barrier}$), thickness of an individual layer in a multi-layered structure are essential parameters to know before the evaluation of energy levels and quasi Fermi level calculations of any quantum well. The normalized quasi Fermi level in the conduction band for lead salt material can be given by[11]

$$F = \frac{(E_F - E_C)}{k_B T}$$
$$= \ln \frac{N}{A_F N_C} + \sum_{i=1}^{\infty} \frac{A_i}{A_F^{2i}} \left(\frac{N}{N_C} \right)^i$$

(2.28)

Here E_F and E_C denote the Fermi and conduction energy value for a carrier concentration of N, k_B is the Boltzmann's constant, T is temperature in K, N_C is the density of states at the bottom of the conduction band, A_F is the bandgap factor which is expressed by the following series

$$A_F = 1 + \frac{3.750}{\varepsilon_g} + \frac{3.281}{\varepsilon_g^2} - \frac{2.461}{\varepsilon_g^3}$$

(2.29)

The normalized quasi Fermi level is expressed as

$$A_F = 1 + \frac{3.750}{\varepsilon_g} + \frac{3.281}{\varepsilon_g^2} - \frac{2.461}{\varepsilon_g^3} \tag{2.30}$$

where ε_g is the normalized bandgap[12].

In general, the QW structure fabricated in our opto-electronics laboratory is comprised of a PbSe (6.126 Å) layer sandwiched between top and bottom PbSrSe confinement layers. This structure is very significant because it can be epitaxially grown either on a BaF$_2$ (lattice constant = 6.196 Å) substrate or on a Si (lattice constant = 5.431 Å) using a CaF$_2$ (lattice constant = 5.464 Å) buffer layer. Mathematical expressions of bandgap for PbSe[9] and Pb$_{1-x}$Sr$_x$Se[13] are cited respectively as

$$E_g^{PbSe}(T) = 125 + \sqrt{400 + 0.256 \times T^2} \tag{2.31}$$

$$E_g^{PbSrSe}(x,T) = 0.150 + 3.608x - 1.314x^2 + \left(0.430 - 3.093x + 6.495x^2\right) \times T \tag{2.32}$$

$$\left(for\ 0 \leq x \leq 0.276,\ 0 < T \leq 350K\right)$$

Equation (2.32) describes the increase of energy bandgap in PbSrSe with the increase in Sr composition. The bulk PbSe bandgap at 300 K is 0.2807 eV. In order to obtain better optical confinement inside the well region of QW structure, the Sr composition (x) should be made as high as possible. However, the epitaxial quality of the MBE-grown Pb$_{1-x}$Sr$_x$Se layer deteriorates with the increase of Sr composition (i.e. higher x) in the material. The maximum obtainable Sr composition with a satisfying PbSrSe growth quality would produce a barrier height of 0.496 eV. The offset energy i.e. the

difference in the energy levels in conduction (CB) and valence band (VB) (i.e. 0.496 -

0.2807 = 0.2153 eV) is assumed to be equally divided between electrons and holes[14].

Previous equations demonstrate the dependence of carrier effective masses on x and T due to the variation of energy bandgap. Thus the four effective masses namely $m_{c,t}$ (conduction band, transverse), $m_{v,t}$ (valence band, transverse), $m_{c,l}$ (conduction band, longitudinal), and $m_{v,l}$ (valence band, longitudinal) may be given as[15]:

Table-2.1: Longitudinal and transverse effective masses used in the calculations of quantized states of electrons and holes in PbSe/PbSrSe MQW structures. (m_0 is the mass of a free electron)

	PbSe (4.2 K)	PbSrSe (4.2 K)	PbSe (295 K)	PbSrSe (295 K)
$m_{c,l}(m_0)$	0.070	0.070	0.113	0.113
$m_{c,t}(m_0)$	0.042	0.042	0.069	0.069
$m_{v,l}(m_0)$	0.068	0.068	0.108	0.108
$m_{v,t}(m_0)$	0.040	0.040	0.054	0.054

Effective mass values at 77 K and 300 K for PbSe/PbSrSe structure are considered to be same as that at 4.2 K and 295 K respectively. Table-2.2 shows the effective masses for different orientations for the energy minima shown in Fig. 2.4. In the table m_t and m_l represents transverse and longitudinal effective masses of electrons and holes, respectively. When growing QW structures along the [111] orientation, in which the effective mass m_l in the longitudinal valley is heavier then that of the three transverse valleys, the subband energies of the transverse valley increase faster. As a

result, the 1-1 subband transition of the longitudinal valley becomes the lowest, and the degeneracy is therefore lifted. Similarly, the [110]-orientation will partially lift the degeneracy. All four energy valleys in the [100] orientation, however, will remain degenerate. For QW structures, when degeneracy is lifted off in the [111] and [110] orientations, the gain is determined by the angle in equation (2.21) and the quasi Fermi energy levels.

Table-2.2: Effective mass along different orientations for L-valley energy minima.

Suraface Orientation	m_x	m_y	m_z	Degeneracy
[100]	m_t	$\dfrac{m_t + 2m_l}{3}$	$\dfrac{3m_t m_l}{m_t + 2m_l}$	4
[110]	m_t	$\dfrac{2m_t + m_l}{3}$	$\dfrac{3m_t m_l}{2m_t + m_l}$	2
	m_t	m_l	m_t	2
[111]	m_t	m_t	m_l	1
	m_t	$\dfrac{m_t + 8m_l}{9}$	$\dfrac{9m_t m_l}{m_t + 8m_l}$	3

In general, the most significant physical parameters on which the QW gain depends are well width and well height. Therefore we divided this report and studied the effect of the crystal growth orientation on subband energy distribution as well as overall QW gain for different well widths for two different well heights: (1) Infinite well height and (2) Finite well height. For the first case, we have considered PbSrSe bandgap of 10000 cm^{-1} (1.24 eV). In practice, the maximum obtainable PbSrSe bandgap with a satisfying PbSrSe growth quality is 4000 cm^{-1} (= 0.496 eV). Thus for the second case, we

have chosen PbSrSe bandgap of 4000 cm^{-1}. The offset energy i.e. the difference in the energy levels in conduction (CB) and valence band (VB) is assumed to be equally divided between electrons and holes[14].

2.4. QW Gain Formulation

The carriers in the QW are confined in the *z*-direction and free to move in *xy*-plane. Therefore, the total energy of a carrier in such a system is the discrete energy value at $\kappa_\perp = 0$, in addition to the energy in *xy*-plane. The energy-momentum relation for QW charge carriers can be written as:

$$E = E_{xy} + E_n \qquad (2.33)$$

where integer *n* represents a discrete energy level E_n, *E* is the total energy of the carrier in the *n*th subband, and E_{xy} is the kinetic energy of the carrier in the two-dimensional (2D) *xy*-plane.

2.4.1. Density of States in QW

The density of states (DOS) in terms of energy, *E* can be represented as[16]:

$$\rho = \frac{\kappa_\perp d\kappa_\perp}{\pi dE(\kappa_\perp)} \qquad (2.34)$$

where,

$$E = \frac{\hbar^2 \kappa_\perp^2}{2m_{eff,well}} + E_n \qquad (2.35)$$

34

Thus, DOS for carriers in SQW can be written as:

$$\rho = \sum_{n=1}^{\infty} \frac{m_{eff,well}}{\pi\hbar^2} H(E - E_n) \qquad (2.36)$$

$m_{eff,well}$ is carrier effective mass in well as described in equation 2.10. $H(E)$ is the Heaviside function which is equal to unity when $E>0$ and is zero when $E<0$.

2.4.2. Momentum Matrix Elements for QW

The optical transition probability of carriers is proportional to momentum matrix element or dipole moment. The optical matrix elements in QW structure are polarization dependent and can be written for transverse electric (TE) and transverse magnetic (TM) mode as[17]:

$$\left|M_{QW,n}\right|^2_{avg} = \frac{3}{4}\left|M_B\right|^2_{avg}\left(1 + \frac{E_n}{E}\right), \text{ for TE mode} \qquad (2.37)$$

and
$$\left|M_{QW,n}\right|^2_{avg} = \frac{3}{4}\left|M_B\right|^2_{avg}\left(1 - \frac{E_n}{E}\right), \text{ for TM mode} \qquad (2.38)$$

where the momentum matrix element ($\left|M_B\right|^2_{avg}$) for conventional three-dimensional lead salt laser is given by[18] [19]:

$$\left|M_B\right|^2_{avg} = \frac{4}{6}m_0 E_g\left(\frac{m_0}{m_l} + \frac{2m_0}{m_t}\right) \qquad (2.39)$$

m_l and m_t are described in section 2.2.

35

2.4.3. QW Gain

The quantum well gain calculation involves solving a 4 × 4 Hamiltonian[20] of the Luttinger-Kohn model. The quantum well subband structure is solved based on entailing the envelope function approximation[21]. In a simple method, the local gain inside the quantum well due to an electronic transition from level p in conduction band to level q in the valence band can be expressed in terms of a product of probability of optical transition (P_{pq}) and reduced density of states (ρ_{pq}). The mathematical equation can be represented as[22]:

$$g_{pq}\left(E_{pq}^0\right) = \int P_{pq}\left(\frac{\varepsilon}{nc}\right)\rho_{pq}\, dE_{pq}$$

$$= \int \left(\frac{2\pi}{\hbar}\right)\left|H_{pq}\right|^2 \left(F_q - F_p\right)\delta\left(E_{pq} - \hbar\omega\right)\left(\frac{\varepsilon}{nc}\right)\rho_{pq}\, dE_{pq}$$

$$= \left(\frac{2\pi}{\hbar}\right)\left|H_{pq}\right|^2 \left(F_q' - F_p'\right)\left(\frac{\varepsilon}{nc}\right)\rho_{pq} \tag{2.40}$$

where ρ_p, ρ_q are the density of states for the pth and the qth levels, n is the real part of the refractive index at the angular emission frequency ω, c the velocity of light, ε the permittivity of the dielectric medium, F_p and F_q are the Fermi functions for the pth and the qth level, F_p' and F_q' are the integrated Fermi functions of the respective levels, H_{pq} the Hamiltonian matrix elements between pth and qth states.

$$\rho_{pq} = \rho_{pq}^0 h\left(\hbar\omega - E_{pq}^0\right) \tag{2.41}$$

$$\left|H_{pq}\right| = \left(\frac{q}{m_0}\right)\left(\frac{2\hbar\omega}{4\varepsilon\varepsilon_0\omega^2}\right)\left|M_B\right|^2_{avg} \tag{2.42}$$

where ε_0 the permittivity of free space.

The variation of gain in a PbSe/PbSrSe SQW at 300 K with wavelengths for three different crystal orientations is illustrated in the following discussion. In our calculations, we have considered five different well widths (1 nm, 2 nm, 3 nm, 4 nm, and 5 nm) of finite QW system. The effective mass values for different crystal orientations are obtained from Table-2.1 and Table-2.2. The numerical calculation is based on a constant sheet carrier density, the product of well width and bulk carrier concentration. The bandgap energy for PbSrSe barrier is considered to be 0.496 eV and 1.24 eV for finite and infinite potential barrier respectively, where the barrier width is kept constant at 30 nm.

2.5. Lead Salt SQW with Infinite Potential Barrier Height

In a QW structure, energy levels in the conduction and valence bands are quantized. These quantized energy levels are lifted from the band edges into the corresponding bands; therefore this necessitates the consideration of band non-parabolicity effect[4] especially for thin wells. This becomes quite significant for IV-VI semiconductors due to the strong non-parabolicity of the bands[14].

In this section, the subband energy levels for the PbSrSe/PbSe/PbSrSe system will be evaluated for three different MBE growth orientations (i.e. [100], [111], and [110]) each for a well thickness of 1 nm. The barrier width and height considered are 30 nm and

1.24 eV respectively. The subband energy levels can be obtained by solving equations 3.5 - 3.7 considering $U_0 = 0.9593$ eV and effective mass values are obtained from Table-2.1 and 2.2.

2.5.1. [111] Crystal Orientation

For [111] orientation, a single L-valley lies along the [111] growth direction i.e. is normal to the (111) plane in reciprocal k-space and the other three L-valleys are at oblique angles. Therefore two different effective masses for charge carriers exist for potential variations along the [111] direction, one for the single normal valley, and one for the three oblique valleys as shown in Table-2.2. The subband energy levels are therefore classified in two groups, one is for the normal valley and the other is for the oblique valley, as illustrated in Fig. 2.5.

Fig. 2.5: Subband energy levels for a 1 nm wide QW (having infinite well height) in the [111] direction for (a) normal, and (b) oblique valleys.
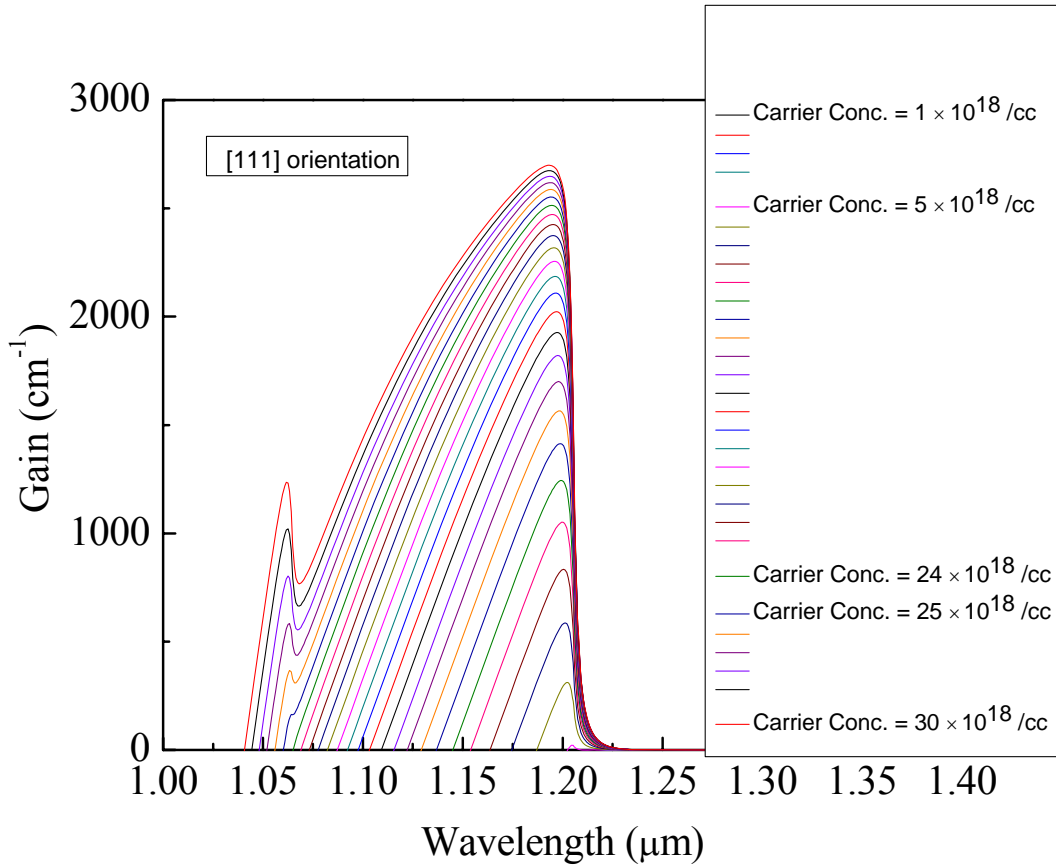
Fig. 2.6: Calculated lead salt QW (having infinite well height) gain for [111] crystal orientation for different carrier concentrations.

Fig. 2.5 demonstrates subband energy level distribution in conduction band (CB) and valence band (VB) in a QW structure having well width of 1 nm. Normal and oblique subband valleys are designated by letters "N" and "O" respectively. In the figure, "$N_{1, C}$" denotes 1st normal conduction subband valley and "$N_{1, V}$" denotes 1st normal valence subband valley. Similarly, "$O_{1, C}$" denotes 1st oblique conduction subband valley and "$O_{1, V}$" denotes 1st oblique valence subband valley. Electronic transition from every conduction subband valley to valence subband valley for both normal as well as oblique valleys is calculated. QW spectral gain for different carrier concentrations at a temperature of 300 K is illustrated in Fig. 2.6. Arrow marks in Fig. 2.5 indicate electronic

transitions contributing in QW gain as shown in Fig. 2.6. As seen in Fig. 2.6, QW gain (~ 29.579 cm^{-1}) starts showing up at a carrier concentration = 5×10^{18} /cc. A single peak occurs in the QW gain curve for lower carrier concentration ($\leq 24 \times 10^{18}$ /cc). The electron transition responsible for that gain peak, occurring at 1.039 eV for a carrier concentration = 30×10^{18} /cc, is from 1st normal conduction subband valley to 1st normal valence subband valley and that transition is symbolized by $N_{1, C} => N_{1, V}$ (indicated by arrow "1" in Fig. 2.5). A second shoulder in the gain curve starts showing up at a carrier concentration = 25×10^{18} /cc. It becomes prominent with the increase in carrier density. That second peak, occurring at 1.168 eV for a carrier concentration = 30×10^{18} /cc, is caused by the electronic transition from 1st oblique conduction subband valley to 1st oblique valence subband valley and that transition is symbolized by $O_{1, C} => O_{1, V}$ (indicated by arrow "2" in Fig. 2.5).

2.5.2. [110] Crystal Orientation

M1$_{2, C}$	0.796 eV		M2$_{2, C}$	0.910 eV	
M1$_{1, C}$	0.394 eV		M2$_{1, C}$	0.432 eV	

"1"   "2"

M1$_{1, V}$ ------ 0.411 eV   M2$_{1, V}$ ------ 0.468 eV
M1$_{2, V}$ ------ 0.845 eV

(a)   (b)
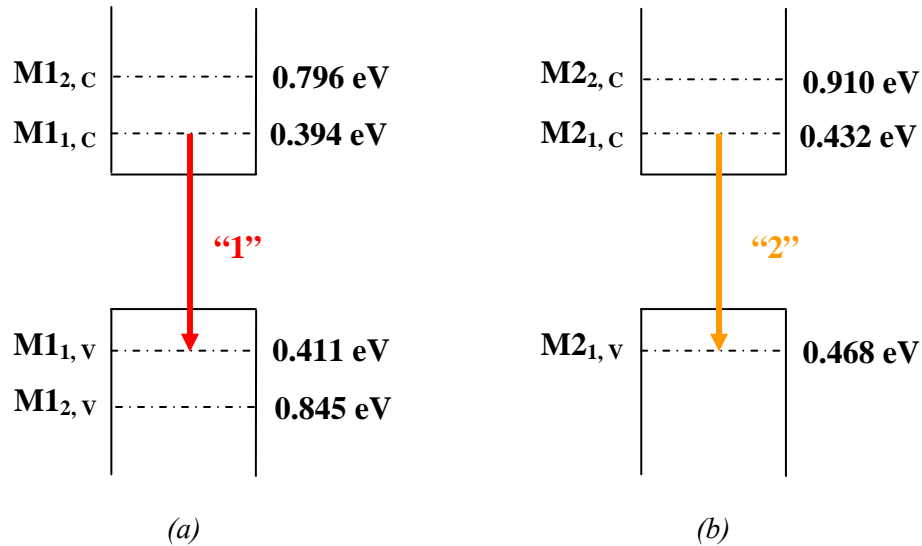
Fig. 2.7: Subband energy levels for a 1 nm wide QW (having infinite well height) in the [110] direction for (a) M1 valley, and (b) M2 valley.

Similarly for the [110] crystal orientation, the L-valley degeneracy is partially lifted forming two different 2-fold degeneracy groups. Those two different groups, having different effective carrier mass values (as shown in Table-2.2), are designated as M1 and M2 valleys. The distribution of subband valley energy levels for a QW structure with well width of 1 nm is described in Fig. 2.7. In the figure, "$M1_{1, C}$" denotes 1st M1 conduction subband valley and "$M1_{1, V}$" denotes 1st M1 valence subband valley. Similarly, "$M2_{1, C}$" denotes 1st M2 conduction subband valley and "$M2_{1, V}$" denotes 1st M2 valence subband valley.
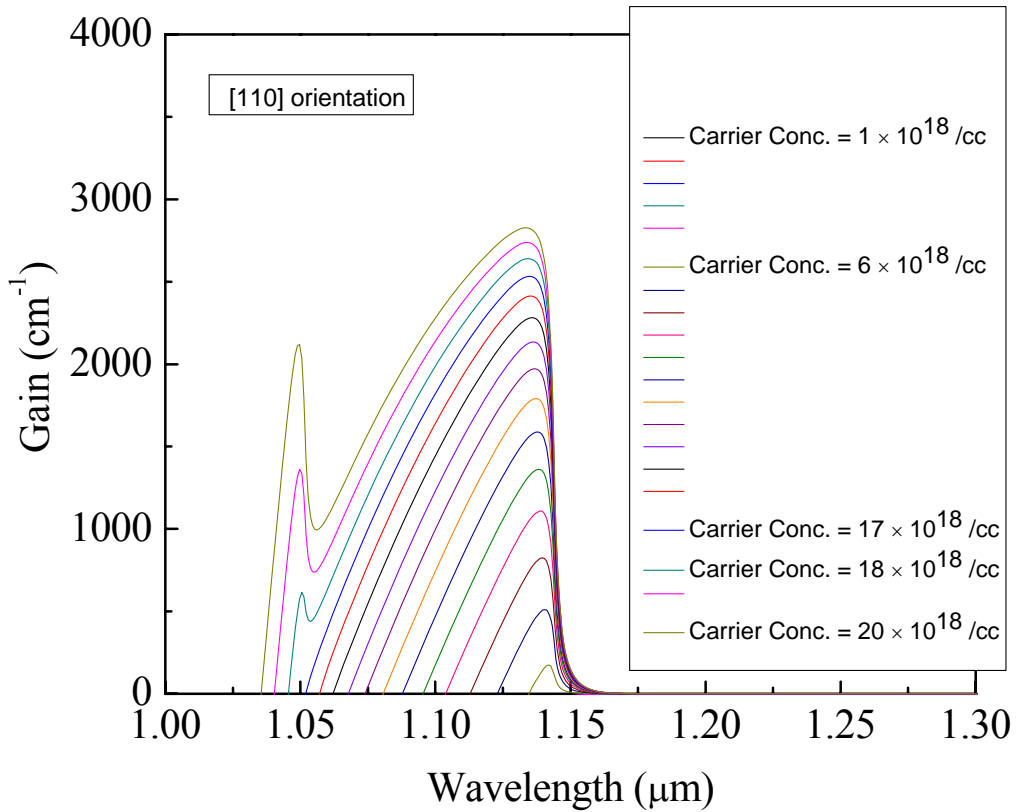
Fig. 2.8: Calculated lead salt QW (having infinite well height) gain for [110] crystal orientation for different carrier concentrations.

QW spectral gain for different carrier concentrations at a temperature of 300 K is illustrated in Fig. 2.8. As seen in figure, QW gain starts showing up (~ 175.579 cm^{-1}) at a carrier concentration = 6×10^{18} /cc. A single peak occurs in the QW gain curve for lower carrier concentration ($\leq 17 \times 10^{18}$ /cc). The electron transition responsible for that gain peak, occurring at 1.093 eV for a carrier concentration = 20×10^{18} /cc, is from 1st M1 conduction subband valley to 1st M1 valence subband valley and that transition is symbolized by M1$_{1, C}$ => M1$_{1, V}$. A second shoulder in the gain curve starts showing up at a carrier concentration = 18×10^{18} /cc. That second peak, occurring at 1.182 eV for a carrier concentration = 20×10^{18} /cc, is caused by the electronic transition from 1st M2 conduction subband valley to 1st M2 valence subband valley and that transition is symbolized by M2$_{1, C}$ => M2$_{1, V}$.

2.5.3. [100] Crystal Orientation
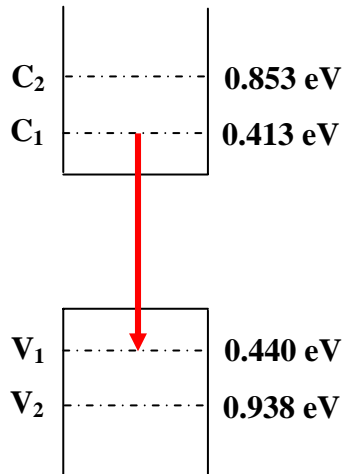
Fig. 2.9: Subband energy levels for a 1 nm wide QW (having infinite well height) in the [100] direction.

Fig. 2.9 demonstrates subband energy level distribution in CB and VB in a [100] oriented lead salt QW structure having well width of 1 nm. Due to the absence of L-

valley degeneracy lifting, always a single peak occurs in the gain curve as shown in Fig. 2.10. The red arrow in Fig. 2.9 indicates the electronic transition responsible for [100] oriented lead salt QW gain. In the figure, "C_1" denotes 1st conduction subband valley and "V_1" denotes 1st valence subband valley. As illustrated in Fig. 2.10, QW gain starts showing up (~ 904.437 cm^{-1}) at a carrier concentration = 10×10^{18} /cc. The single peak occurring in the QW gain curve is caused by the electron transition from C_1 to V_1. The transition energy is calculated to be 1.136 eV and is symbolized by $C_1 \Rightarrow V_1$.
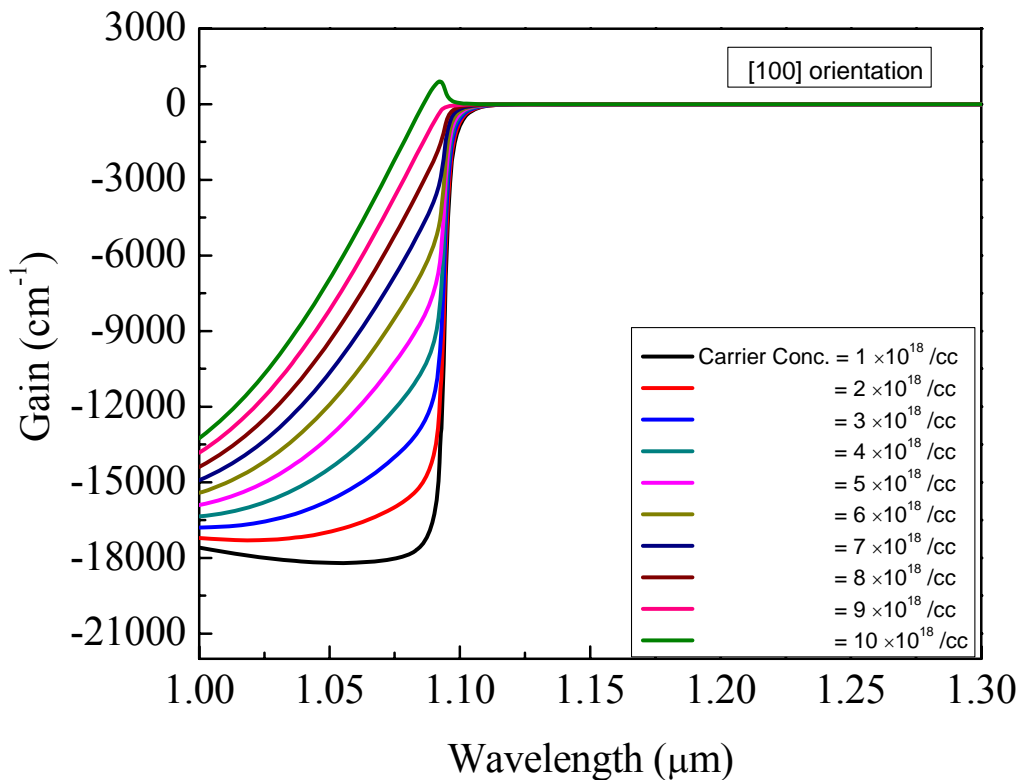
Fig. 2.10: Calculated lead salt QW (having infinite well height) gain for [100] crystal orientation for different carrier concentrations.

2.5.4. Effect of Crystal Orientation on QW Gain (Infinite Case)
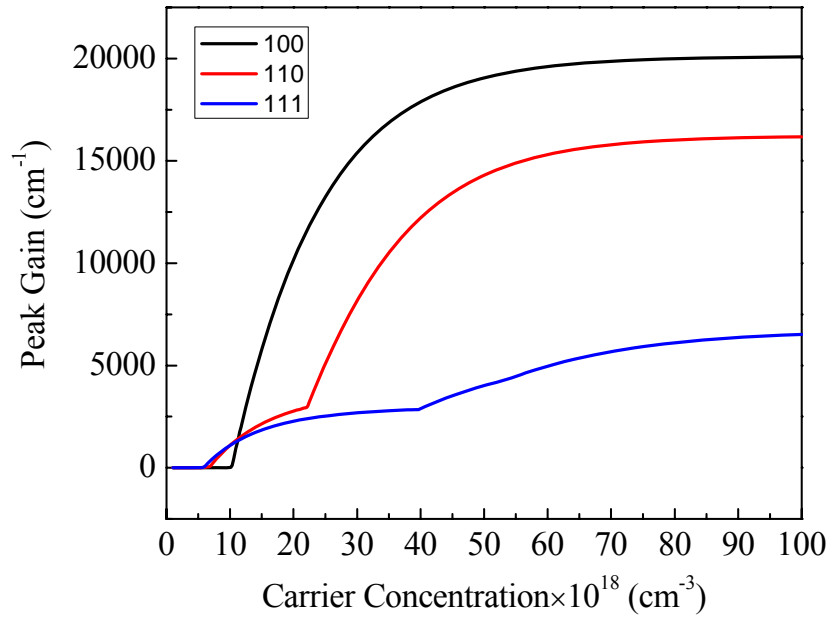
(a)
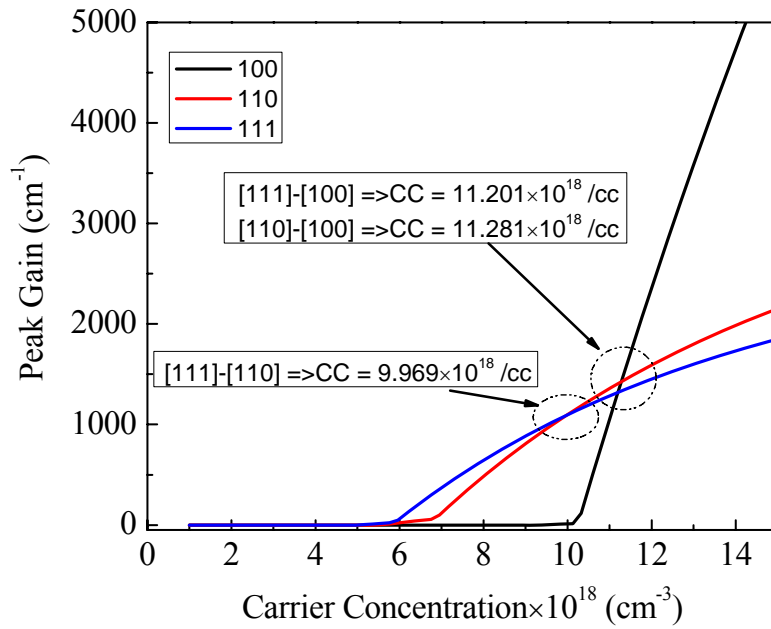
(b)

Fig. 2.11: Calculated peak gain variation for lead salt QW (having infinite well height and well width = 1 nm) structure with different crystal orientations for different carrier concentrations at (a) broad range, (b) short range.

It can be observed from Fig. 2.6 and 2.8 that both [111] and [110] oriented QW produce more than one peak in the gain curve by increasing carrier concentration. This happens due to the existence of L-valley degeneracy splitting, which leads to the formation of two-fold subband valley distribution of energy levels, for those two orientations. It would be interesting to identify the maximum carrier concentration at which a single subband valley transition contributes in overall QW gain for those two crystal orientations. The calculated results show that for [111] crystal orientation, the maximum carrier concentration at which a single subband valley contributes in overall QW gain is 17×10^{18} /cc. The peak gain at this carrier concentration is 2528.673 cm^{-1} and the electronic transition responsible for this gain occurs at 1.093 eV. For [100] crystal orientations, there is no such degeneracy lifting and therefore all electronic transitions occur at the same energy level and contribute in a single gain peak. Peak gains of lead salt SQW structure at 300 K for different carrier concentrations have been calculated for three crystal orientations as demonstrated in Fig. 2.11. From figure, it can be stated that the gain thresholds for [111], [110], and [100] orientations at 300 K are 5×10^{18} /cc, 6×10^{18} /cc, and 10×10^{18} /cc respectively. It is interesting to note that the QW gain threshold is minimum for [111] crystal orientation. This is caused by the complete L-valley degeneracy lifting occurring for this crystal orientation. This consequently helps in generating population inversion phenomenon, which results in producing QW gain by electron-hole recombination mechanism, at lower carrier concentration. Due to the effect of partial degeneracy lifting off method, [110] orientation has lower threshold than [100] orientation, which does not lift off L-valley degeneracy. After the gain threshold value of carrier concentration, [111] orientation generates the maximum QW gain as demonstrated

in Fig. 2.11. After the carrier concentration reaches a value of 9.969×10^{18} /cc, the spectral gain for [110] orientation becomes higher than that for [111] orientation. After crossing the gain threshold carrier concentration, the spectral gain value for [100] orientation increases faster than other two crystal orientations. The gain for [100] orientation becomes higher than both [111] and [110] orientations after the carrier concentration reaches values of 11.201×10^{18} /cc and 11.281×10^{18} /cc respectively.

2.6. Lead Salt SQW with Finite Potential Barrier Height

A similar description concerning the distribution of the subband energy levels for the finite well height PbSrSe/PbSe/PbSrSe QW system would be described here for three different growth orientations. The comparative analysis on the finite well width QW gain conducted for different crystal orientations is critically important from the perspective of a more real world device fabrication aspect. Five different well thicknesses of 1 nm, 2 nm, 3 nm, 4 nm, and 5 nm are considered in this case. The barrier width and height considered are kept constant at 30 nm and 0.496 eV respectively. The subband energy levels can be obtained by solving equations 2.5 - 2.7 considering $U_0 = 0.2153$ eV and effective mass values are obtained from Table-2.1 and 2.2.

2.6.1. [111] Crystal Orientation

Fig. 2.12: Calculated lead salt QW (having finite well height and well width = 1 nm) gain for [111] crystal orientation for different carrier concentrations.

As shown in Fig. 2.12, QW gain starts showing up (~ 434.735 cm^{-1}) at a carrier concentration = 5×10^{18} /cc. A single peak occurs in the QW gain curve for lower carrier concentration ($\leq 16 \times 10^{18}$ /cc). The electron transition responsible for that gain peak, occurring at 0.578 eV for a carrier concentration = 16×10^{18} /cc, is symbolized by $N_{1, C}$ => $N_{1, V}$ (indicated by arrow "1" in Fig. 2.13). A second shoulder in the gain curve starts showing up at a carrier concentration = 17×10^{18} /cc. It becomes prominent with the increase in carrier density. The electron transition responsible for the second peak,

occurring at 0.675 eV for a carrier concentration = 17×10^{18} /cc, is symbolized by $O_{1, C}$ => $O_{1, V}$ (indicated by arrow "2" in Fig. 2.13).
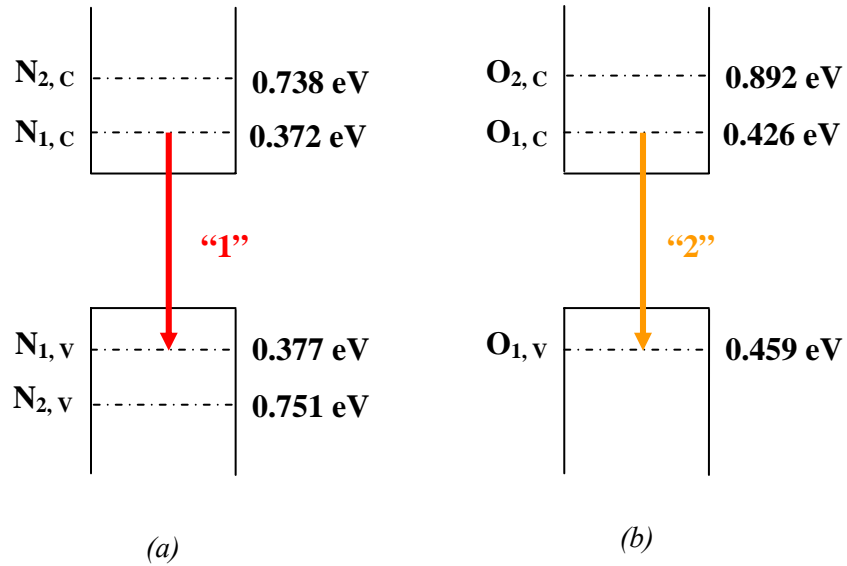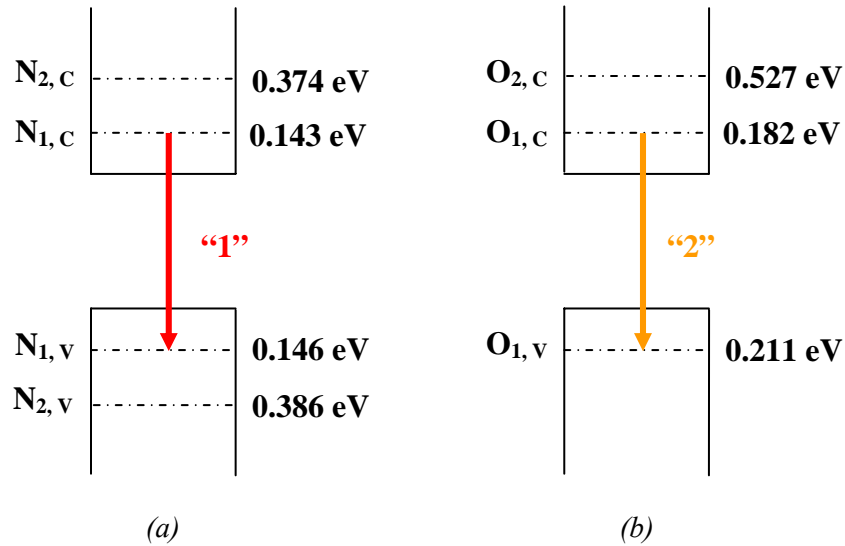

Fig. 2.13: Subband energy levels for a 1 nm wide QW (having finite well height) in the [111] direction for (a) normal, and (b) oblique valleys.

Fig. 2.14 illustrates the variation of QW gain with carrier concentrations for different well widths. Other QW parameters are kept constant in this study. One of the main purposes of this study is to identify the best lead salt crystal orientation which produces maximum gain when only one subband valley transition contributes in spectral gain. Peak gains of QW having different well widths are populated in Table-2.3. The maximum carrier concentration for which a single subband valley transition contributes in spectral gain (identified by the single gain peak in Fig. 2.14) for a QW structure with fixed well width is given by the 2nd column in Table-2.3. The corresponding transition energy is given in the 3rd column. When carrier concentration exceeds this condition, then another subband valley transition ($O_{1, C}$ => $O_{1, V}$ transition as shown in Fig. 2.13) starts

contributing in overall QW spectral gain. This is visualized by second peak in gain curve (Fig. 2.14).

Fig. 2.14: Calculated lead salt QW (having finite well height and different well widths) gain (vertically shifted) for [111] crystal orientation for different carrier concentrations.

The minimum carrier concentration for which two subband valley transitions contribute in spectral gain (identified by the double gain peak in Fig. 2.14) is given by the 4th column in Table-2.3. The corresponding transition energies are given in the 5th column. Colors in individual boxes in the table signify the corresponding transition energies indicated by arrow marks in Fig. 2.13. The formation of subband energy level is dependent on well width. As well width increases, subband energy levels get closer to the conduction and valence band edges. This is illustrated by the reduction of values of

49

transition energies, given in the 3rd and the 5th columns of the following table, with the increase in quantum well width. Therefore for a fixed carrier concentration, the probability of populating more than one subband energy level is more for QW having larger well widths.

Table-2.3: Peak gain and corresponding subband valley transition for [111] oriented QW structure having different well widths.

Well width (nm)	Peak gain when single subband valley contributing QW gain at maximum carrier concentration	Corresponding transition energy in subband valley	Peak gain when two subband valleys contributing QW gain at minimum carrier concentration	Corresponding transition energy in subband valley
1	3941.016 cm^{-1} at 16 × 10^{18} /cc	0.578 eV	4074.276 cm^{-1} and 762.425 cm^{-1} at 17 × 10^{18} /cc	0.578 eV 0.675 eV
2	913.162 cm^{-1} at 7 × 10^{18} /cc	0.459 eV	1170.945 cm^{-1} and 727.471 cm^{-1} at 8 × 10^{18} /cc	0.459 eV 0.489 eV
3	527.034 cm^{-1} at 6 × 10^{18} /cc	0.418 eV	761.879 cm^{-1} and 585.745 cm^{-1} at 7 × 10^{18} /cc	0.419 eV 0.443 eV
4	272.802 cm^{-1} at 5 × 10^{18} /cc	0.392 eV	500.546 cm^{-1} and 237.575 cm^{-1} at 6 × 10^{18} /cc	0.392 eV 0.416 eV
5	316.221 cm^{-1} at 5 × 10^{18} /cc	0.371 eV	509.558 cm^{-1} and 42.889 cm^{-1} at 6 × 10^{18} /cc	0.372 eV 0.395 eV

This phenomenon is explicitly verified by Table-2.3. It can be observed that for a QW with well width = 1 nm, single subband valley transition occurs for a maximum carrier concentration of 16×10^{18} /cc; whereas for a well width of 2 nm, the similar phenomenon occurs when the carrier concentration reaches a value of 7×10^{18} /cc.

2.6.2. [110] Crystal Orientation
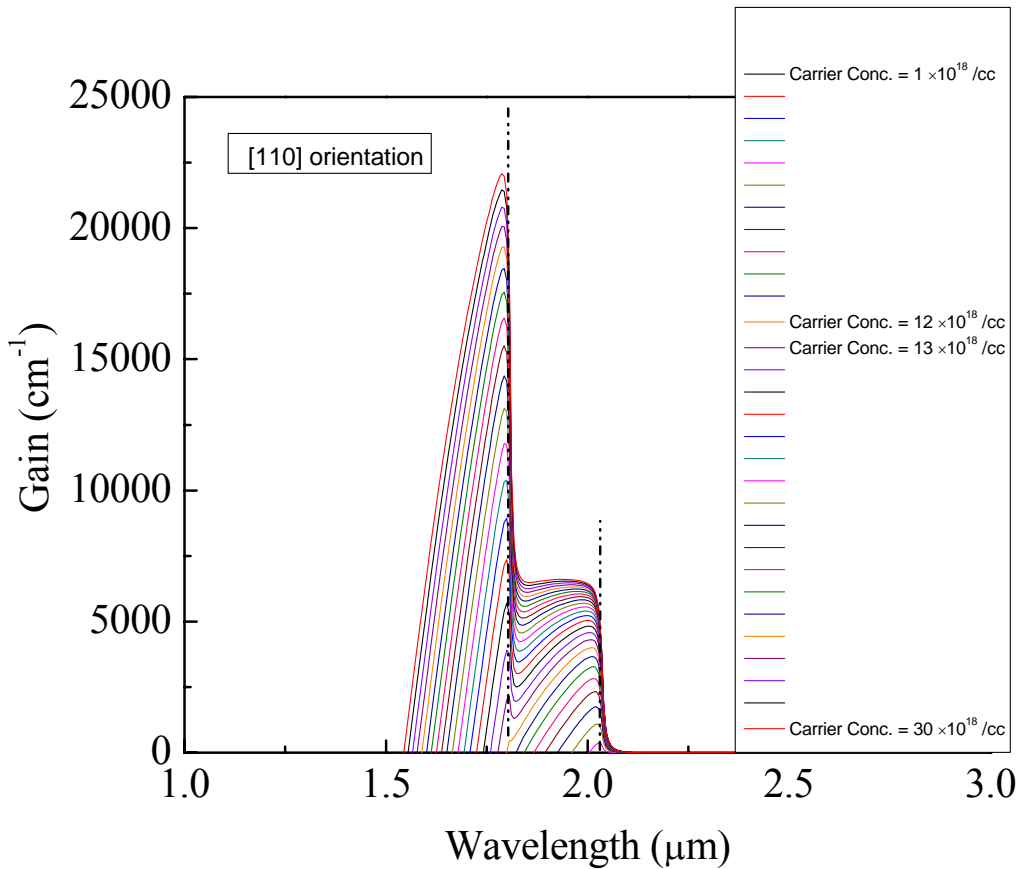
Fig. 2.15: Calculated lead salt QW (having finite well height and well width = 1 nm) gain for [110] crystal orientation for different carrier concentrations.

As shown in Fig. 2.15, QW gain starts showing up ($\sim$ 368.651 cm^{-1}) at a carrier concentration = 5×10^{18} /cc. A single peak occurs in the QW gain curve for lower carrier concentration ($\leq 12 \times 10^{18}$ /cc). The electron transition responsible for that single gain

peak, occurring at 0.617 eV for a carrier concentration = 12×10^{18} /cc, is symbolized by $M1_{1, C} \Rightarrow M1_{1, V}$ (indicated by arrow "1" in Fig. 2.16). A second shoulder in the gain curve starts showing up when the carrier concentration reaches a value of 13×10^{18} /cc. It becomes prominent with the increase in carrier density. The electron transition responsible for the second peak, occurring at 0.689 eV for a carrier concentration = 13×10^{18} /cc, is symbolized by $M2_{1, C} \Rightarrow M2_{1, V}$ (indicated by arrow "2" in Fig. 2.16).

$M1_{2, C}$	0.431 eV		$M2_{2, C}$	0.545 eV
$M1_{1, C}$	0.158 eV		$M2_{1, C}$	0.187 eV
"1"			"2"	
$M1_{1, V}$	0.171 eV		$M2_{1, V}$	0.218 eV
$M1_{2, V}$	0.480 eV			
(a)			(b)	
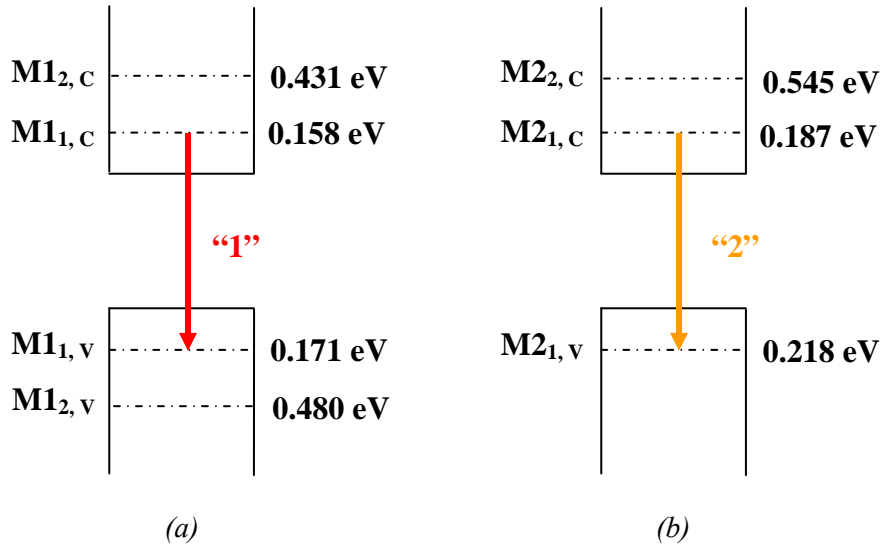
Fig. 2.16: Subband energy levels for a 1 nm wide QW (having finite well height) in the [110] direction for (a) M1 valley, and (b) M2 valley.

Fig. 2.17 depicts the variation of the [110] oriented lead salt QW gain with carrier concentrations for different well widths. Peak gains of QW having different well widths are populated in Table-2.4. Similar to the [111] orientation, the maximum carrier concentration for which a single subband valley transition contributes in spectral gain (identified by the single gain peak in Fig. 2.17) for a [110] oriented QW structure with fixed well width is given by the 2nd column in Table-2.4. The corresponding transition energy is given in the 3rd column. When carrier concentration exceeds this condition, then

another subband valley transition (M2$_{1, C}$ => M2$_{1, V}$ transition as shown in Fig. 2.16) starts contributing in overall QW spectral gain. This is visualized by second peak in gain curve (Fig. 2.17).
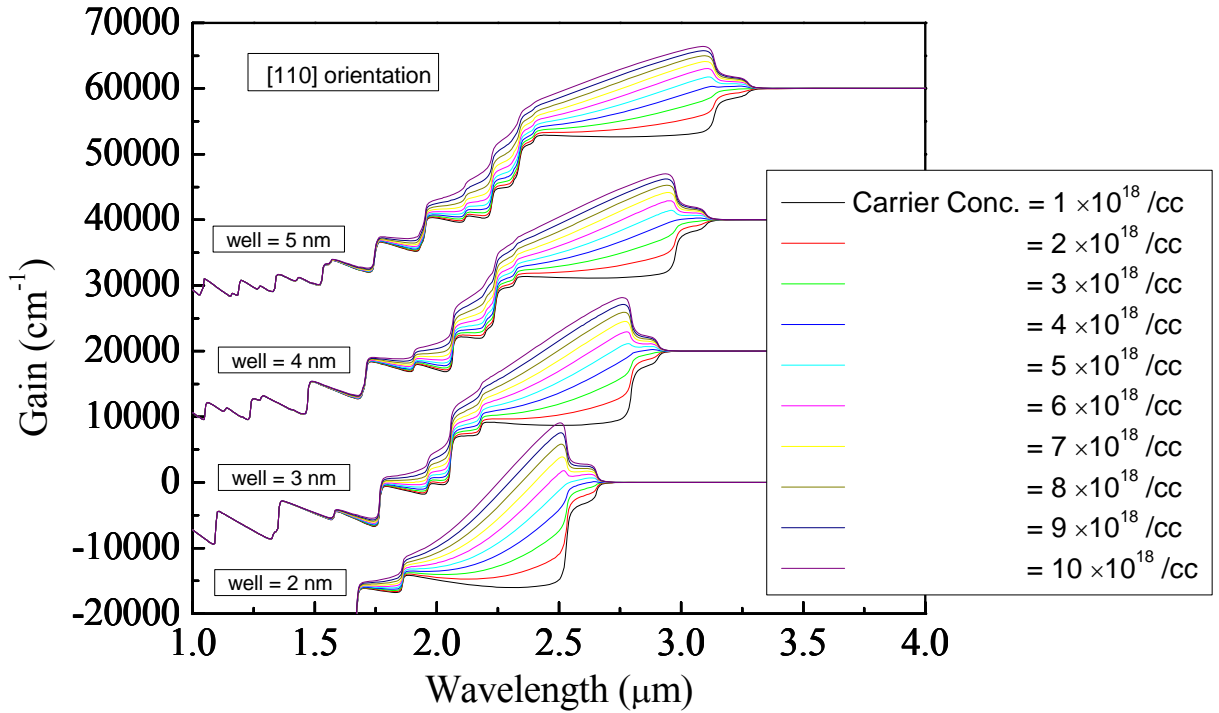
Fig. 2.17: Calculated lead salt QW (having finite well height and different well widths) gain (vertically shifted) for [110] crystal orientation for different carrier concentrations.

The minimum carrier concentration for which two subband valley transitions contribute in QW spectral gain (identified by the double gain peak in Fig. 2.17) is given by the 4th column in Table-2.4. The corresponding transition energies are given in the 5th column. Colors in individual boxes in the table signify the corresponding transition energies indicated by arrow marks in Fig. 2.16. Similar to the [111] orientation as well width increases, subband energy levels get closer to the conduction and valence band

edges. This is illustrated by the reduction of values of transition energies, given in the 3rd and 5th columns of the following table, with the increase in well width.

Table-2.4: Peak gain and corresponding subband valley transition for [110] oriented QW structure having different well widths.

Well width (nm)	Peak gain when single subband valley contributing QW gain at maximum carrier concentration	Corresponding transition energy in subband valley	Peak gain when two subband valleys contributing QW gain at minimum carrier concentration	Corresponding transition energy in subband valley
1	4027.854 cm^{-1} at 12 × 10^{18} /cc	0.617 eV	4300.928 cm^{-1} and 2177.771 cm^{-1} at 13 × 10^{18} /cc	0.617 eV 0.689 eV
2	704.533 cm^{-1} at 5 × 10^{18} /cc	0.470 eV	1228.837 cm^{-1} and 1873.293 cm^{-1} at 6 × 10^{18} /cc	0.471 eV 0.493 eV
3	221.191 cm^{-1} at 4 × 10^{18} /cc	0.429 eV	704.533 cm^{-1} and 1142.818 cm^{-1} at 5 × 10^{18} /cc	0.429 eV 0.445 eV
4	281.813 cm^{-1} at 4 × 10^{18} /cc	0.402 eV	679.410 cm^{-1} and 1404.697 cm^{-1} at 5 × 10^{18} /cc	0.403 eV 0.419 eV
5	-	-	375.751 cm^{-1} and 351.720 cm^{-1} at 4 × 10^{18} /cc	0.382 eV 0.397 eV

From Table-2.4, it can be observed that for a QW with well width = 1 nm, a single subband valley transition contributes in overall QW gain for a maximum carrier

concentration of 12×10^{18} /cc; whereas for a well width of 2 nm, the similar condition

occurs when the carrier concentration $= 5 \times 10^{18}$ /cc.

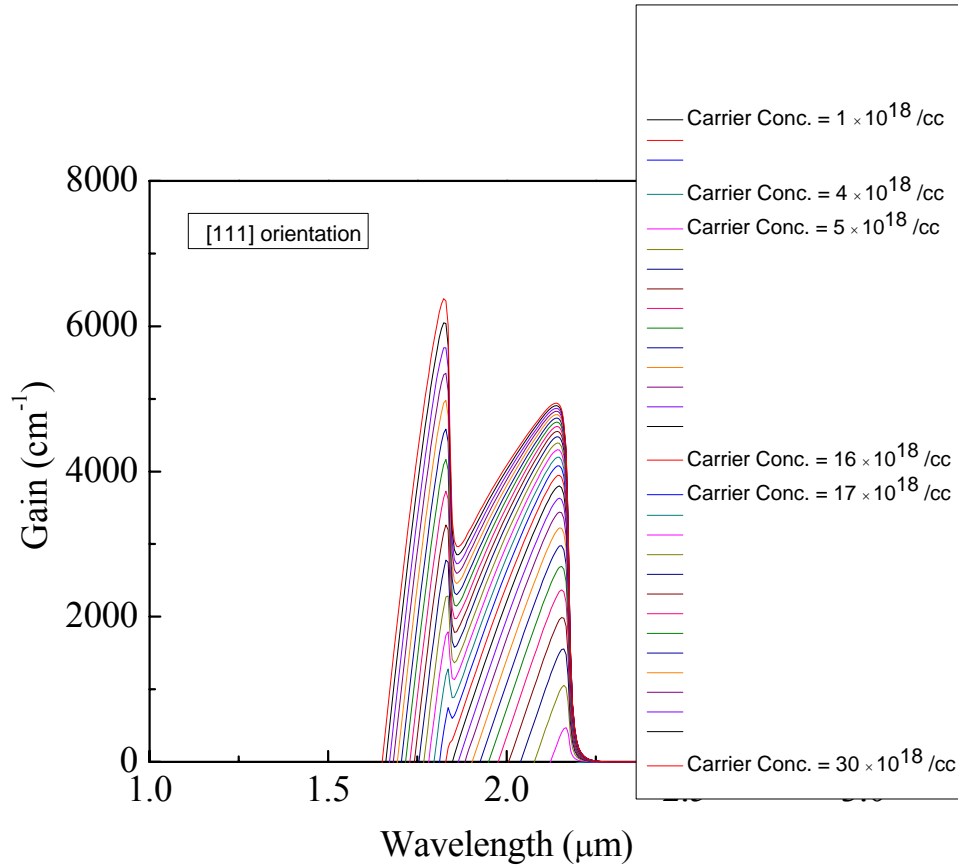### 2.6.3. [100] Crystal Orientation
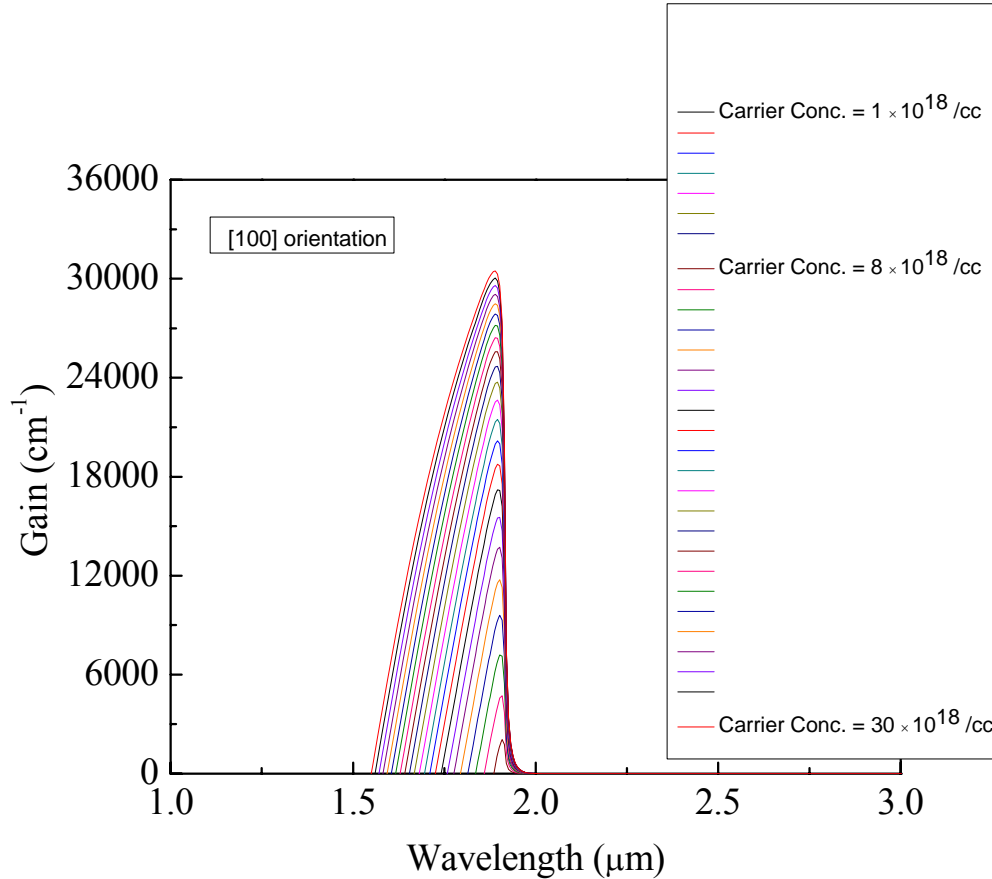
Fig. 2.18: Calculated lead salt QW (having finite well height and well width = 1 nm) gain for [100] crystal orientation for different carrier concentrations.

Fig. 2.19 describes subband energy level distribution in conduction and valence

bands in a [100] oriented lead salt QW structure having well width of 1 nm. Due to the

absence of L-valley degeneracy lifting, always a single peak occurs in the gain curve as

shown in Fig. 2.18. As illustrated in Fig. 2.18, QW gain starts showing up (~2143.091

cm^{-1}) at a carrier concentration $= 8 \times 10^{18}$ /cc. The single peak occurring in the QW gain

curve is caused by the electron transition which is symbolized by $C_1 \Rightarrow V_1$ as shown in Fig. 2.19. The corresponding transition energy is calculated to be 0.650 eV.
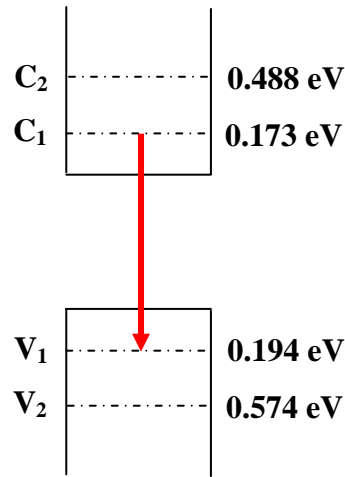
Fig. 2.19: Subband energy levels for a 1 nm wide QW (having finite well height) in the [100] direction.

Fig. 2.20 shows the [100] oriented lead salt QW gain variation with carrier concentrations for different well widths. Peak gains of QW having different well widths are populated in Table-2.5. The minimum carrier concentration for which a single subband valley transition contribute in QW spectral gain is given by the 2nd column in Table-2.5. The corresponding transition energy is provided in the 3rd column. Similar to other two crystal orientations as well width increases, subband energy levels get closer to the conduction and valence band edges. This is illustrated by the reduction of values of transition energies, given in the 3rd column of Table-2.5, with the increase in well width.
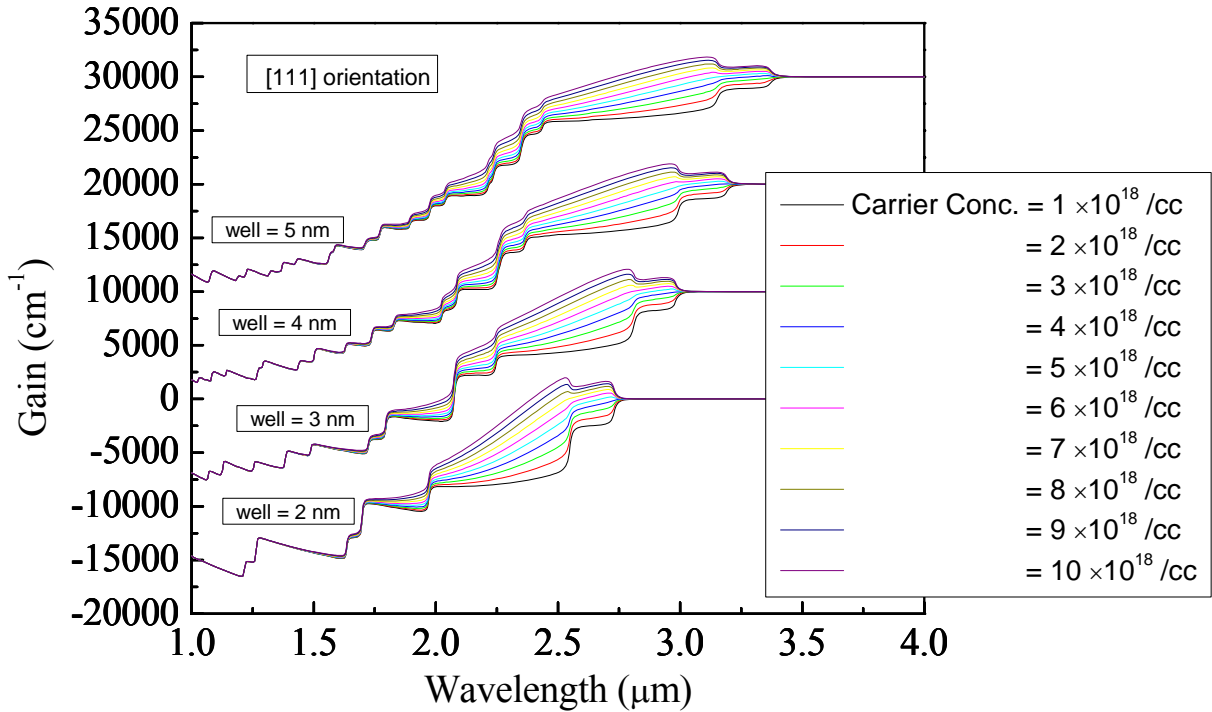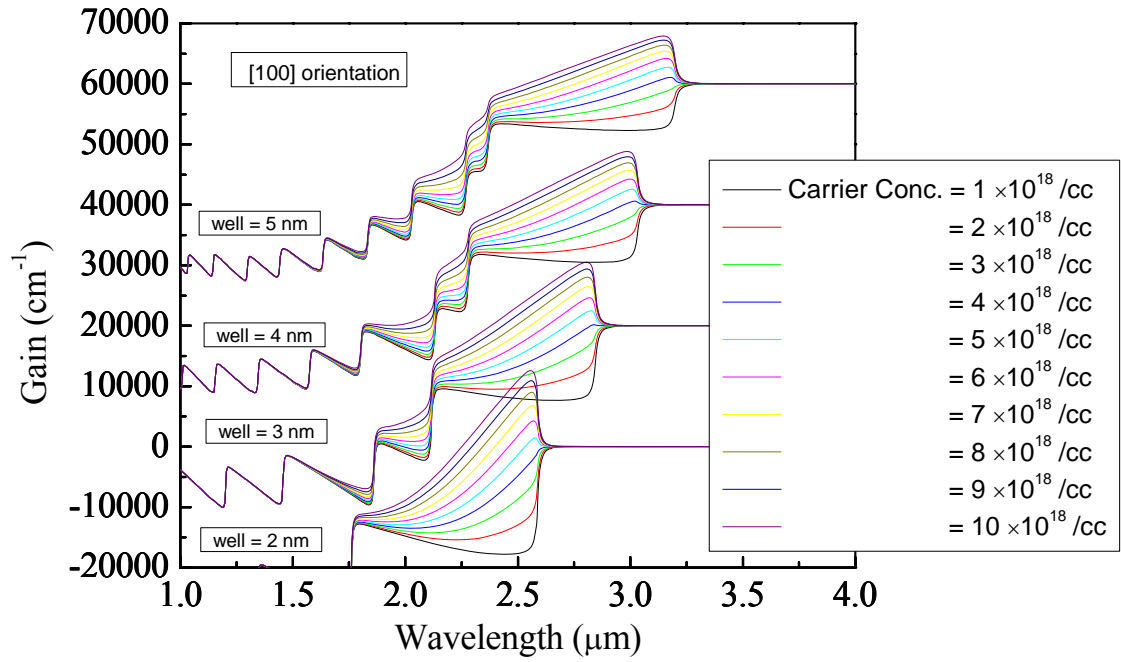
Fig. 2.20: Calculated lead salt QW (having finite well height and different well widths) gain (vertically shifted) for [100] crystal orientation for different carrier concentrations.

Table-2.5: Peak gain and corresponding subband valley transition for [100] oriented QW structure having different well widths.

Well width (nm)	Peak gain when single subband valleys contributing QW gain at minimum carrier concentration	Corresponding transition energy in subband valley
1	2143.091 cm^{-1} at 8×10^{18} /cc	0.650 eV
2	1483.889 cm^{-1} at 5×10^{18} /cc	0.482 eV
3	172.731 cm^{-1} at 4×10^{18} /cc	0.437 eV
4	644.457 cm^{-1} at 4×10^{18} /cc	0.411 eV
5	1054.069 cm^{-1} at 4×10^{18} /cc	0.391 eV

2.6.4. Effect of Crystal Orientation on QW Gain (Finite Case)

(a)

(b)
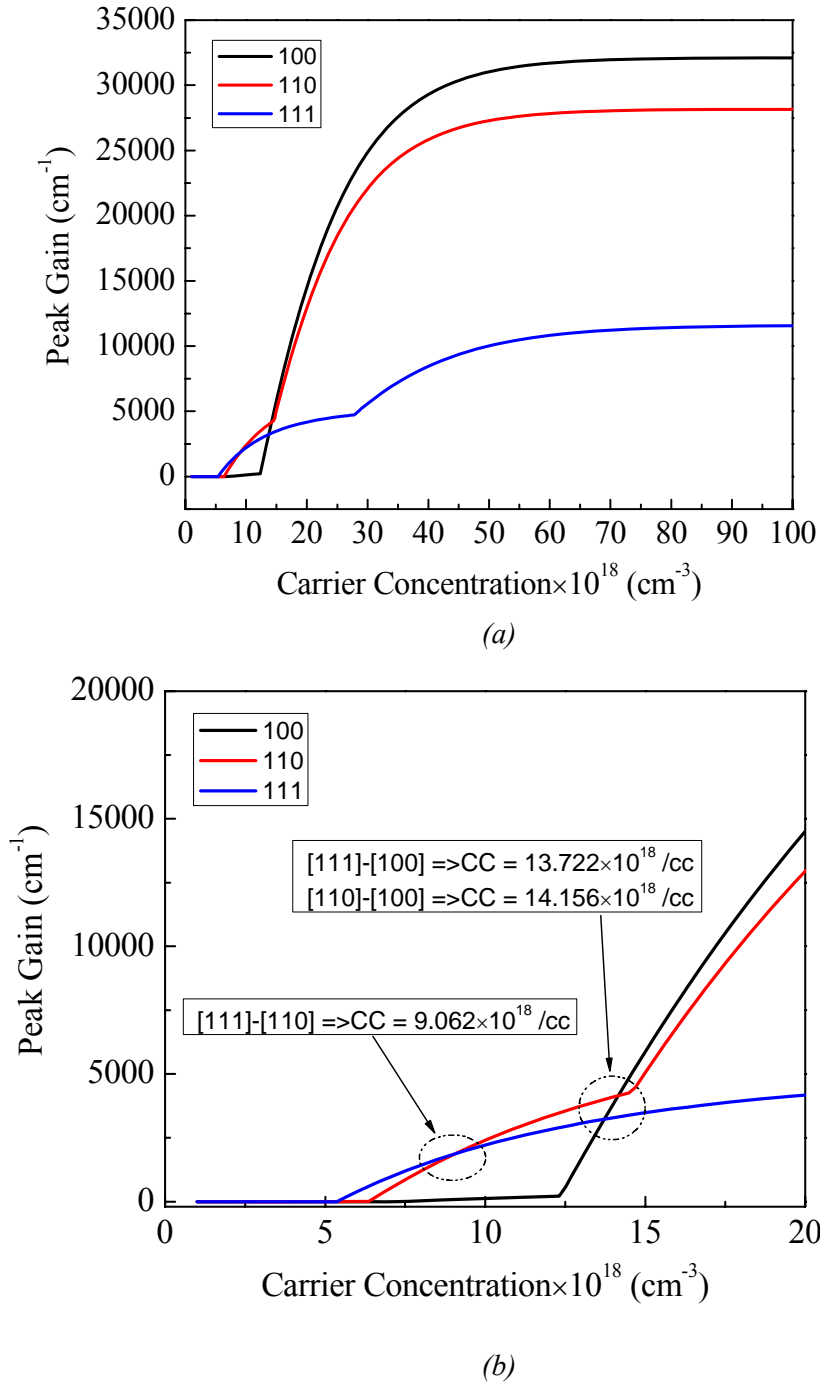
Fig. 2.21: Calculated peak gain variation for lead salt QW (having finite well height and well width = 1 nm) structure with different crystal orientations for different carrier concentrations at (a) broad range, (b) short range.

Peak gains of lead salt SQW structure (having finite well height and a well width of 1 nm) at 300 K for different carrier concentrations have been calculated for three crystal orientations as described in Fig. 2.21. From figure, it can be stated that the gain thresholds for [111], [110], and [100] orientations are 5.500×10^{18} /cc, 6.412×10^{18} /cc, and 12.328×10^{18} /cc respectively. The QW gain threshold is minimum for [111] crystal orientation. This is similar to the infinite case described in Section 2.5.4. After the gain threshold value of carrier concentration, [111] orientation generates the maximum QW gain as demonstrated in Fig. 2.11. After the carrier concentration reaches a value of 9.062×10^{18} /cc, the spectral gain for [110] orientation becomes higher than that for [111] orientation. After crossing the gain threshold carrier concentration, the spectral gain value for [100] orientation increases faster than other two crystal orientations. The gain for [100] orientation becomes higher than both [111] and [110] orientations after the carrier concentration reaches values of 13.722×10^{18} /cc and 14.156×10^{18} /cc respectively.

2.7. Gain of Practically Feasible QW Structure

Most QW structures with a very thin well width (few nm) considered in the previous section can not be fabricated in real world. For a very thin well width, the interface i.e., the surface between a well and an adjoining barrier in a QW structure poses huge challenges in terms of fabrication as well as device manufacturing point of view. Thus in this section, most common well widths practiced to fabrication QW structure are considered. In particular, well width values used for QW gain calculation in this phase are 5 nm, 10 nm, 15 nm, 20 nm and 25 nm.
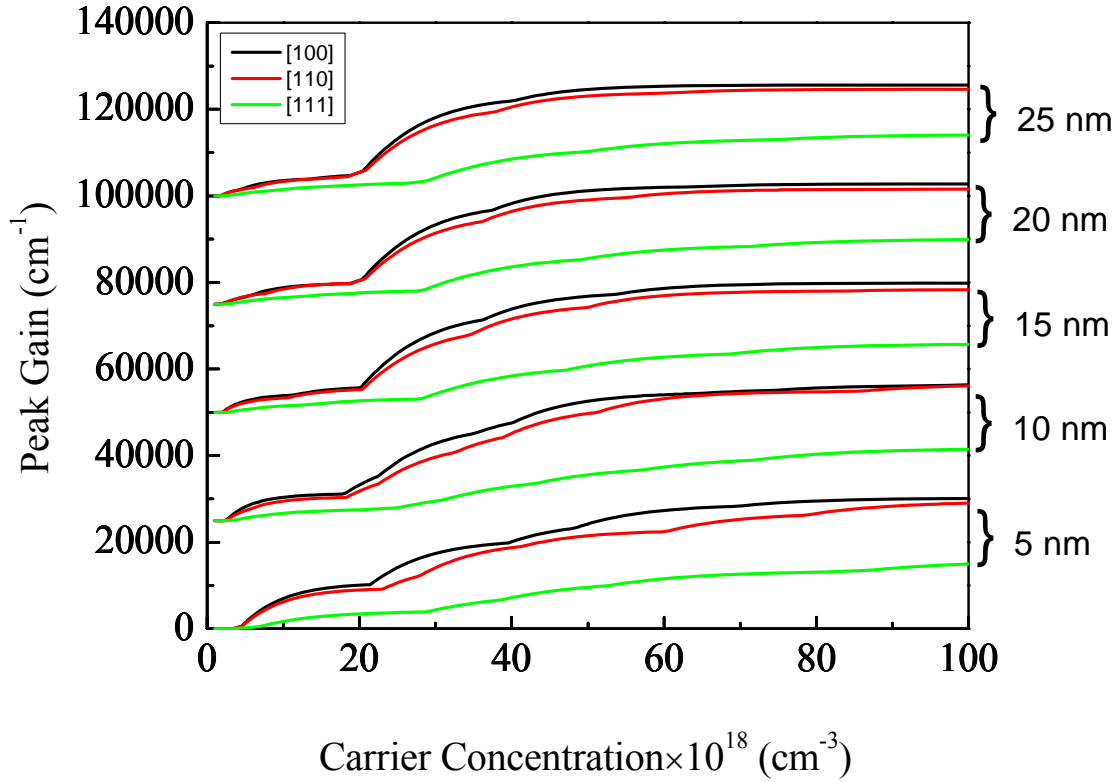
Fig. 2.22: Calculated peak gain variation for lead salt QW (having finite well height and different well widths) structure with different crystal orientations for different carrier concentrations.

Peak gains of lead salt SQW structure (having finite well height) with different well widths at 300 K have been formulated for different carrier concentrations as demonstrated in Fig. 2.22. All three different crystal orientations are considered in the gain calculations. QW gain threshold values for all these orientations are populated in Table-2.6. It can be observed that the gain threshold value is lowest for [111] orientation. L-valley degeneracy lifting is the reason for this phenomenon. Due to the partial lifting of degeneracy, [110] orientation has lower threshold than [100] orientation which does not show any degeneracy lifting. The best explanation of QW gain dependence on crystal orientation can be given as follows. Due to the existence of two different sets of effective masses for both [111] as well as [110] orientation, electronic transitions provide local

QW gain at different energy levels. But in case of [100] orientation, due to existence of 4-fold degeneracy all four subband valley transitions contribute QW gain at the same energy level. Therefore [100] crystal orientation gives out maximum QW gain. As seen in Section 2.2, QW gain is directly proportional to dipole moment or momentum matrix element. Smaller values of dipole moment for [111] orientation compared to that for [110] orientation could be a responsible factor for achieving higher QW gain from [110] oriented lead salt QW structures.

Table-2.6: Gain threshold values for lead salt QW structure having different well widths for different crystal orientations.

Well width (nm)	Threshold carrier concentration for [111]	Threshold carrier concentration for [110]	Threshold carrier concentration for [100]
5	2.678×10^{18} /cc	3.207×10^{18} /cc	3.393×10^{18} /cc
10	1.931×10^{18} /cc	2.061×10^{18} /cc	2.241×10^{18} /cc
15	1.632×10^{18} /cc	1.780×10^{18} /cc	1.780×10^{18} /cc
20	1.337×10^{18} /cc	1.597×10^{18} /cc	1.597×10^{18} /cc
25	1.302×10^{18} /cc	1.586×10^{18} /cc	1.586×10^{18} /cc

2.8.   Conclusions

A theoretical model has been presented which evaluates gain from the quantum well structure based on IV-VI lead salt semiconductor material. The calculation is carried out utilizing the very popular Kane's double band model. Low dimensional (of the order of nanometer) QW structure shows contrasting difference in the modal gain than its three dimensional counterparts. This happens due to the significant variation of L-valley degeneracy lifting for different crystal orientations. The modal gain of the QW structure for different growth orientation is calculated by keeping the injected sheet carrier charge density as constant. The carrier effective masses at L points in the Brillouin zone along [100], [110], and [111] orientations are implemented in generating modal gains for the respective QW orientations. The subband energy levels together with the corresponding quasi Fermi energy levels are evaluated and plotted for all three crystal orientations and QW parameters. Both finite and infinite wells are considered in this study to observe the effect of crystal directions on QW spectral gain from a practical and theoretical point of views.

2.9. References

---

[1] A. Yariv, "Optical Electronics," *Oxford Series in Electrical and Computer Engineering, ISBN-0030702895*, Saunders College Publishing: FL, pp. 1-552, 1991.

[2] C. Weisbuch, B. Vinter, "Quantum Semiconductor Structures: Fundamentals and Applications," *ISBN-0127426809*, Academic Press Inc.: Boston, CA, pp. 1-252, 1991.

[3] R. A. Morrow, "Establishment of an effective-mass Hamiltonian for abrupt heterojunctions," *Phys. Rev. B*, vol. 35, pp. 8074-8079, 1987.

[4] T. Hiroshima, R. Lang, "Effects of conduction-band nonparabolicity on quantized energy levels of a quantum well," *Appl. Phys. Lett*., vol. 49, pp. 456-457, 1986.

[5] J. O. Dimmock, "The physics of semimetals and narrow gap semiconductors," D. L. Carter, R. T. Bate, Ed., *Supplement no. 1 to the J. of phys. and chem.. of sol.*, Pergamon Press: Oxford, NY, vol. 32, pp. 1-568, 1971.

[6] A. Yariv, C. Lindsey, U. Sivan, "Approximate analytic solution for electronic wave functions and energies in coupled quantum wells," *J. Appl. Phys*., vol. 58, pp. 3669-3672, 1985.

[7] Y. Arakawa, A. Yariv, "Quantum well lasers-gain, spectra, dynamics," *IEEE J. Quant. Electron*., vol. QE-22, pp. 1887-1899, 1986.

[8] G. P. Agrawal, N. K. Dutta, "Long-Wavelength Semiconductor Lasers," *ISBN-0442209959,* Van Nostrand Reinhold: NY, pp. 1-473, 1986.

[9] H. Preier, "Recent advances in lead-chalcogenide diode lasers," *Appl. Phys*., vol. 20, pp. 189-206, 1979.

[10] J. M. Luttinger, W. Kohn, "Motion of electrons and holes in perturbed periodic fields," *Phys. Rev*., vol. 97, pp. 869-883, 1955.

[11] V. Altschul, E. Finkman, "Simple approximation for fermi energy in nonparabolic semiconductors," *Appl. Phys. Lett*., vol. 58, pp. 942-944, 1991.

[12] X. Lu, Z. Shi, "Theoretical investigations of [110] IV-VI lead salt edge-emitting lasers," *IEEE J. Quant. Electron.*, vol. 41, pp. 308-315, 2005.

[13] W. Z. Shen, H. F. Yang, L. F. Jiang, K. Wang, G. Yu, H. Z. Wu, P. J. McCann, "Band gaps, effective masses and refractive indices of PbSrSe thin films: key properties for mid-infrared optoelectronic device applications," *J. Appl. Phys.*, vol. 91, pp. 192-198, 2002.

[14] D. L. Partin, "Lead salt quantum well structures," *IEEE J. Quant. Electron.*, vol. 24, pp. 1716-1726, 1988.

[15] H. Z. Wu, N. Dai, M. B. Johnson, P. J. McCann, Z. Shi, "Unambiguous observation of subband transitions from longitudinal valley and oblique valleys in IV–VI multiple quantum wells," *Appl. Phys. Lett.*, vol. 78, pp. 2199-2201, 2001.

[16] Y. Arakawa, A. Yariv, "Theory of gain, modulation response, and spectral linewidth in AlGaAs quantum well lasers," *IEEE J. Quant. Electron.*, vol. 21, pp. 1666-1674, 1985.

[17] M. Asada, A. Kameyama, Y. Suematsu, "Gain and intervalence band absorption in quantum-well lasers," *IEEE J. Quant. Electron.*, vol. 20, pp. 745-753, 1984.

[18] N. K. Dutta, "Calculated threshold current of GaAs quantum well lasers," *J. Appl. Phys.*, vol. 53, pp. 7211-7214, 1982.

[19] D. Kasemset, C. -S. Hong, N. B. Patel, P. D. Dapkus, "Graded barrier single quantum well lasers-theory and experiment," *IEEE J Quant Electron*, vol. QE-19, pp. 1025-1030, 1983.

[20] S. L. Chuang, "Efficient band-structure calculation of strained quantum-wells," *Phys. Rev. B*, vol. 43, pp. 9649-9661, 1991.

[21] G. Bastard, "Superlattice band structure in the envelope-function approximation," *Phys. Rev.*, vol. 24, pp. 5693-5697, 1981.

[22] F. Wooten, "Optical properties of solids," New York and London: Academic, 1972.

CHAPTER 3

LEAD SALT LIGHT EMITTING DEVICES

3.1. Advantages of [110] Growth Orientation

The first IV-VI lead salt laser was realized on PbTe in 1964[1]. After two years i.e., in 1966 the first semiconductor laser was fabricated based on III-V GaAs structure. During that period of time, all lead salt semiconductor lasers were generally fabricated on [100]-orientated lead salt substrates. This had been practiced because the natural cleavage plane of lead salt materials is (100). Thus, two parallel facets, necessary to form a lasing Fabry-Perot cavity, can naturally be formed on lead salt structures grown on (100) plane. Previously, it has been theoretically established by our opto-electronics group that the [110] growth orientation is the best crystal orientation for QW lead salt laser fabrication[2]. Theoretical investigations for the [110] orientation showed higher gain as well as higher efficiency, compared to the conventional [100] orientated lasers. But the theoretical simulation was not accurate and was based on the approximation that the QW gain was five times the spectral gain of PbSe single layer. However, there is a necessity to demonstrate the feasibility of lasing cavity formation on a [110] oriented lead salt epilayers.

Lead chalcogenide materials have four L-valley degeneracy in the Brillouin zone. The electronic structure and energy level distribution in the crystal lattice structure have already been detailed in Chapter 2. Crystal growth of lead salt materials along [110]-orientation help in partially lifting off the degeneracy. In case of growth along [100]

direction, the energy valleys remain degenerated. Fig. 3.1 represents a comparative diagram demonstrating calculated peak gains along [111], [110] and [100] orientations along with the free carrier absorption loss ($\sigma_F N$). There it can be observed that the [111] growth orientation leads to the lowest value of threshold carrier concentration.
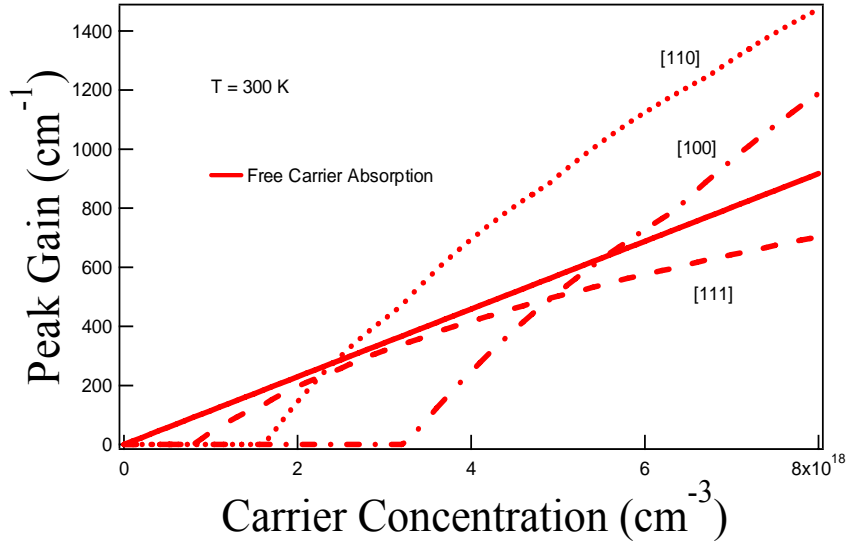
Fig. 3.1: Formulated peak gains for different lead salt QW orientations such as [111], [100], and [110] at different injected carrier concentrations at 300 K. The free carrier absorption in the material is represented by a solid line.

The low threshold laser operation is best suited for low loss lasing devices such as vertical cavity surface emitting laser (VCSEL). Therefore [111] crystal growth orientation is the best fit for fabricating such device structures. The rate of gain increment along [111] orientation is higher than that of the free carrier absorption loss. Thus for relatively high loss devices such as edge emitting laser, [111] orientation would tend to have gain saturation. In order to realize edge emitting laser, it necessitates choosing the crystal growth orientation which produces maximum gain. From Fig. 3.1, it can be seen

that the [110] orientation offers the maximum gain among all other possible crystal growth orientations considered for laser structure fabrication. Due to the lifting of degeneracy for structures with [111] and [110] orientations, less number of sub-valleys is filled. This, in turn, helps in separating quasi-Fermi levels to separate more from the band edges. This effect causes the reduction of threshold and the rise of the spectral gain. As the carrier concentration increases, more and more valleys start getting populated with electrons and holes and their recombination processes help in the increment of overall gain.
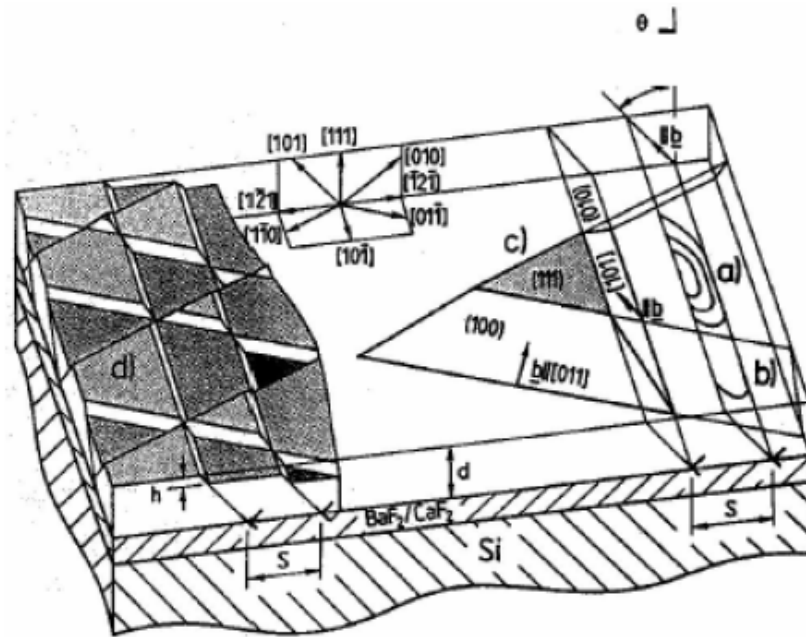
Fig. 3.2: Schematic representation of the distribution of the {100}<110> glide system for the rock salt (NaCl) type PbSe (111) layers (After H. Zogg, et al).

The other critical advantage of [110] orientation is its low dislocation density. As illustrated in Fig. 3.2, the mechanism of strain relaxation in IV-VI materials is the

67

dislocation glide. From Fig. 3.2, it can be inferred that the Burgers vectors are of type $a/2$ <110>. The primary glide planes for IV-VI lead chalcogenide materials are {100}, which are different than other zinc-blende type semiconductor materials. The {100} crystal planes are inclined to the [111]-oriented semiconductor surface. Thus, each time a mechanical strain generated inside the epitaxial layer structure (e.g., during MBE growth process or lattice mismatches in the multi-layer structure or temperature changes), this strain can get relaxed by dislocation glide on the {100} planes. This takes place because the Schmid factors[3] are high for [110] growth orientation. However, for [100] orientation, the Schmid factors for glide in primary {100} planes are absent. Therefore no glide mechanism can take place in the primary {100} planes.

3.2.   Preliminary Results from [110] Oriented Structures on BaF$_2$ Substrate

MBE growth along [110]-orientated BaF$_2$ substrates, which remained unexplored for a long time, was another promising phase for IV-VI semiconductor technology. The huge challenge for achieving this goal was to develop an optimized polishing recipe which would lead to form a scratch-less substrate for epitaxial growth. A chemo-mechanical polishing recipe for [110] BaF$_2$ substrate for MBE growth was developed by the OU group. This new development is extremely exciting and is undoubtedly a breakthrough for mid-IR lead salt semiconductor lasers. We have successfully accomplished the growth of PbSe/PbSrSe QW structures on polished [110] BaF$_2$ substrates. *In situ* reflection high energy electron diffraction (RHEED) during MBE growth demonstrated a high-quality two-dimensional (2D) growth mode of the lead salt material on the BaF$_2$ substrates.
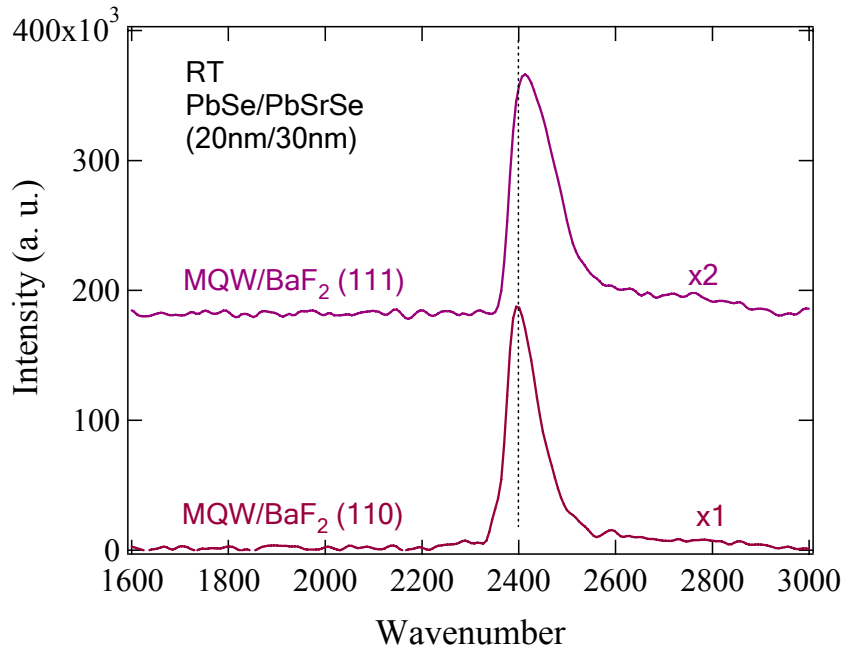
Fig. 3.3: Comparison of room temperature photoluminescence from samples on [110] and [111] BaF₂ substrates.
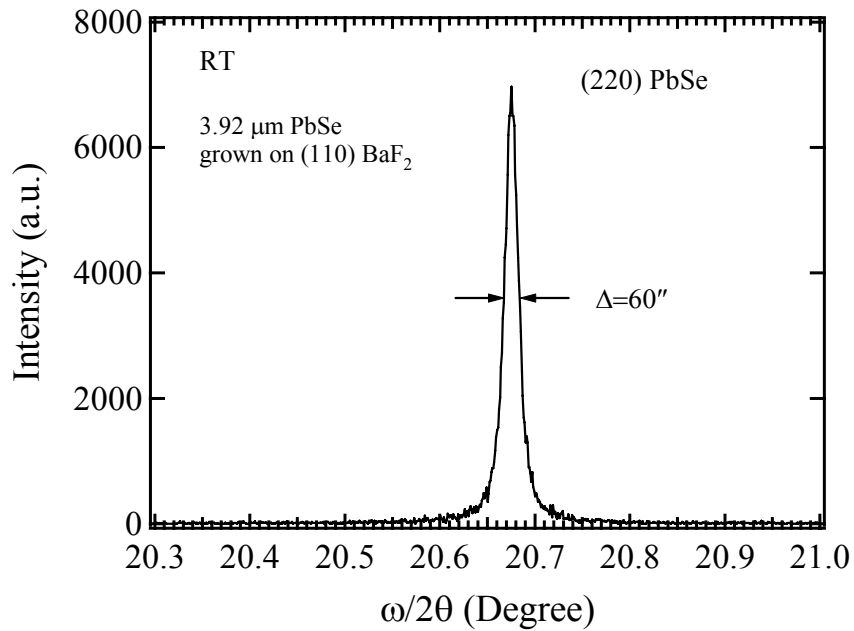
Fig 3.4: High resolution x-ray diffraction spectrum of the (220) reflection from a PbSe thin film on a (110) BaF₂ substrate.

69

Fig. 3.3 shows room temperature PL emission[4] from a seven pair PbSe (20 nm)/PbSrSe (30nm) QW structure grown on [110] BaF$_2$. The results are compared with the PL emission of the same structure on polished [111] cleaved substrate grown in the same MBE run. As can be seen that the PL intensity of [110] sample is about 1.5 times higher than that of [111] sample. This result indicates high material quality and is very encouraging for making infrared opto-electronic devices.

The (110) BaF$_2$ substrate and 3.9 µm (110) PbSe thin film were investigated with high reflection X-ray diffraction (HRXRD) of the symmetrical (220) reflections[5]. The measured full width at half maximum (FWHM) of (110) BaF$_2$ substrate was 23 arcsec, which is similar to the theoretical value of the FWHM. The (220) rocking curve of the PbSe thin film is shown in Fig. 3.4 and has a FWHM of 60 arcsec. This indicates that a high crystalline quality PbSe epitaxial layer was obtained. Typical linewidths of (222) rocking curves for PbSe thin films grown on (111) BaF$_2$ substrates are between 90 and 150 arcsec. The slight broadening of FWHM for PbSe single layer compared with the (110) BaF$_2$ substrates might be due to crystal size effects, non-uniform strain, and dislocations. The dislocation density of the PbSe thin film has been estimated from the rocking curve measurements[6] to be 1×10^7 cm^{-2}. The higher quality of (110) PbSe thin films should improve the performance of lead salt optoelectronic devices.

3.3.   [110] Oriented Electrically Pumped IV-VI Edge-emitting Laser

While cost effective, the fabrication of MIR lasers on BaF$_2$ substrates is tremendously challenging because these materials do not cleave along the same planes. BaF$_2$ has a natural cleavage plane of (111) while Pb-salt epi-layers cleave along (100).

The resultant fabrication has proven quite challenging, therefore, before reaching out to achieve our ultimate goal of demonstrating lead-salt lasers on inexpensive BaF_2 substrates, we have first elected to fabricate edge-emitters successfully on [110]-oriented lead-salt substrates[7], as the orientation is supposed to be the vital component for the lifting of degeneracy.

3.3.1. Surface Preparation for [110]-oriented PbSnSe Substrate for MBE Growth
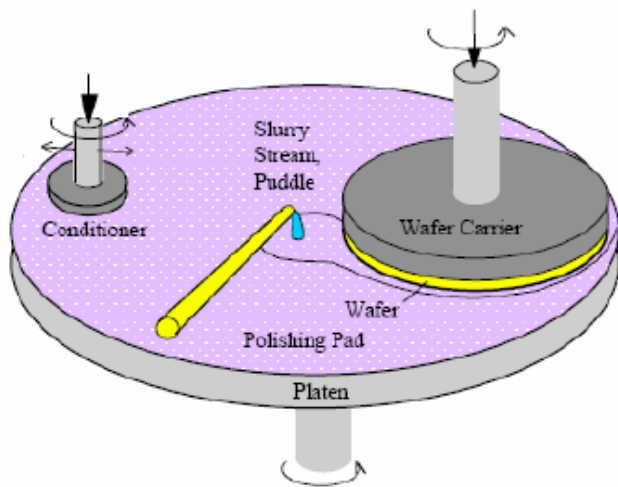
(a)

(b)

Fig. 3.5: (a) Schematic diagram of a rotating polisher, (b) Bench Top LabOne polishing machine used in clean-room for CMP polishing.

A thoroughly polished, smooth and uniform substrate is essential for the MBE growth of laser structures. A novel optimized procedure was adopted to polish a [110]-oriented PbSnSe substrate. The method consisted of both mechanical as well as chemical cycles. Chemical mechanical polishing (CMP)[8] is critically important for the semiconductor industry at the present moment. The polishing machine used during the process is demonstrated in Fig. 3.5. The substrates or wafers are mounted on a wafer-carrier at the time of polishing. The optimization is required in terms of external weights which need to be used directly on top of substrate holder. During polishing, the substrate and polishing pad rotates against each other while keeping the slurry in the middle of the pad and substrate.

The chemical cycles involved two steps with two different chemical recipes: CYCLE-A and CYCLE-B. The first cycle had higher etching rate than the second cycle. The goal was to remove the large surface non-uniformities at a faster rate with the first cycle. The chemical polishing solutions for [110] oriented lead salt materials were similar as used for [100] oriented lead chalcogenides. The polishing recipes which have been optimized in OU clean-room are subject to NDA (Non Disclosure Agreement).

As shown in Fig. 3.6(a), the unpolished PbSnSe wafer had numerous deep grooves and saw marks on the surface. As a first step, these shallow marks were mechanically removed using a Buehler Alpha Micropolish 5 μm alumina suspension on a glass plate, after which, the topical scratches were reduced to the range of 3-50 μm (Fig. 3.6(b)).
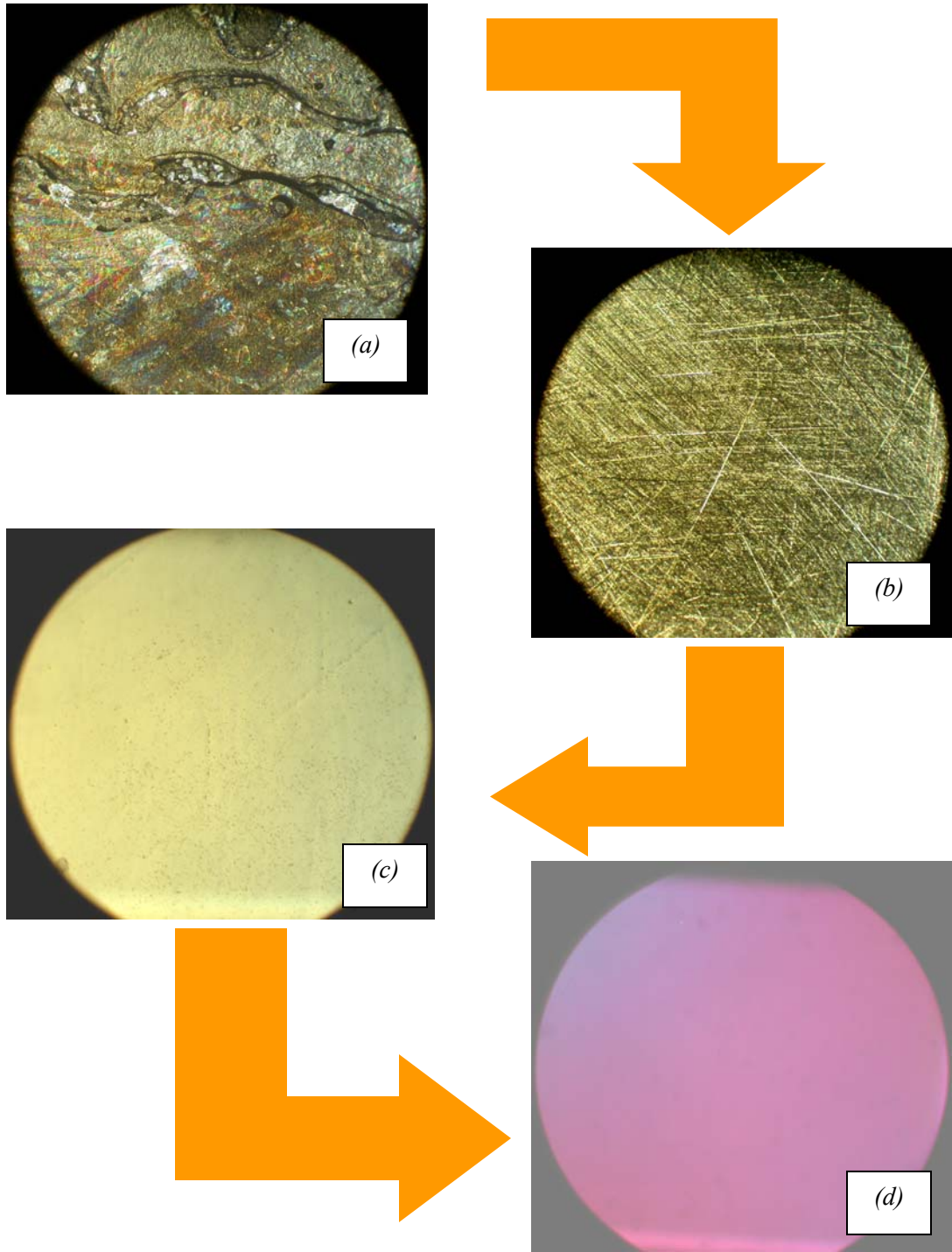
Fig. 3.6: Nomarski images of a [110]-oriented PbSnSe substrate (a) before polishing, (b) after mechanical polishing, (c) after CYCLE-A, (d) after CYCLE-B.

In order to remove the deeper scratches, the first step of mechanical polishing was followed by the first chemical cycle, CYCLE-A. The etching rate for this cycle was measured to be approximately 2-3 μm/minute, depending on the etching environment. These external factors include: the flow rate of polishing chemicals, the holder weight per unit wafer surface area, the grit size of the polishing cloth, and the rotational speed of polishing. The Nomarski image of the substrate surface after CYCLE-A is provided in Fig. 3.6(c). Aside from a few light scratches and slight non-uniformities along the surface, the majority of the deep scratches were removed. CYCLE-B was the final chemical polishing step. This final cycle was employed to remove the remaining light scratches and surface non-uniformities. The etching rate for this optimized polishing step was approximately 0.5 μm/minute.

As demonstrated in Fig. 3.6(d), the final polishing step resulted in a defect free, smooth, and uniform substrate. The final step of polishing was obtained when no light scattering from the substrate surface, under a narrow intense spot of Nomarski microscope, was observed by naked eye. As most lead salt materials are extremely soft, there is a practical difficulty remains associated in handling those during processing. Therefore, to alleviate those challenges, filter papers and chemically resistant sample holders were used during processing. After chemical polishing cycles the samples were thoroughly cleaned under flowing de-ionized (DI) water for about 30 minutes. The polished substrate was deemed epi-ready after scrupulous cleaning with electronic grade chemical reagents such as acetone, propanol, and methanol. The epi-ready substrate was then loaded inside the molecular beam epitaxy (MBE) chamber for laser structure growth. The custom designed MBE growth chamber used to grow epitaxial layer

structures is illustrated in Fig. 3.7. The two-dimensional uniformity of the substrate surface was confirmed by the streakiness of the reflected high energy electron diffraction (RHEED) pattern (as shown in Fig. 3.8(a)).

Fig. 3.7: Custom designed MBE growth chamber in opto-electronics lab at OU.
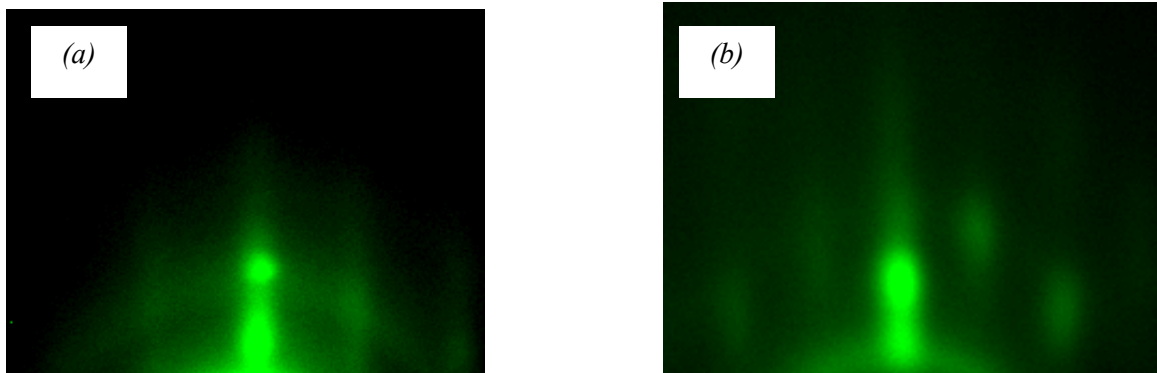
Fig. 3.8: RHEED patterns from (a) the PbSnSe polished substrate and (b) after MBE growth.

3.3.2. MBE Growth Structure and Device Fabrication

n-PbSe layer (150 nm)

Graded n-PbSrSe confinement layer (2.05 μm)

Active region (450 nm)

Graded p-PbSrSe confinement layer (2.05 μm)

p-PbSe layer (150 nm)

[110] PbSnSe substrate
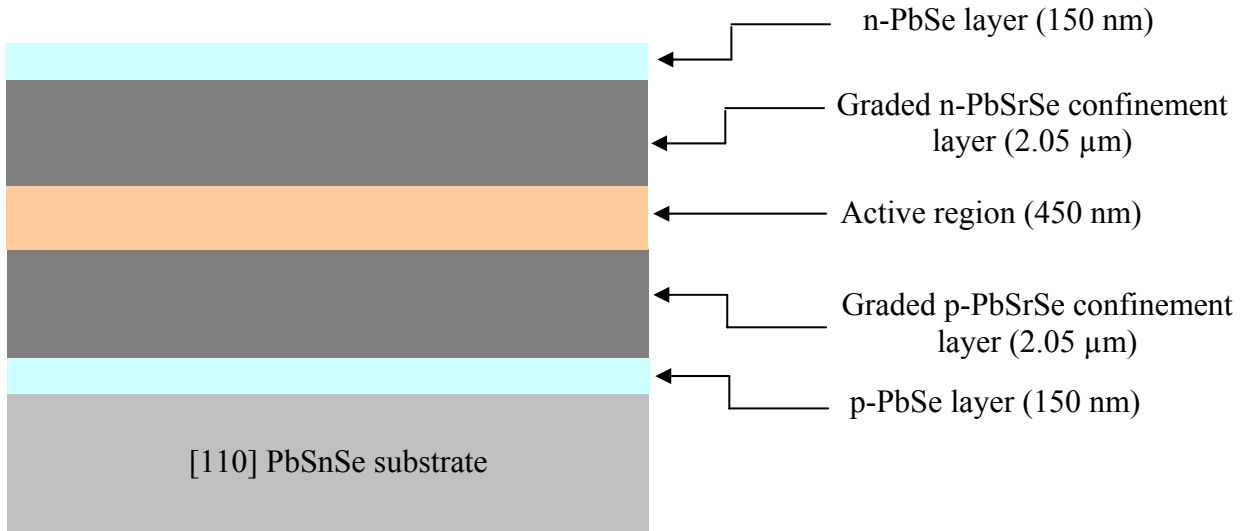
Fig. 3.9: Schematic structure of an electrically pumped multiple quantum well (MQW) IV-VI laser.

As depicted in Fig. 3.9, the resultant laser structure consisted of a 150 nm thick bottom p-PbSe cladding layer, followed by a 2.05 μm thick graded p-PbSrSe confinement layer, an active layer (thickness ~ 450 nm) consisting of 9 pairs of PbSe/Pb$_{0.97}$Sr$_{0.03}$Se multiple quantum wells (MQW), a 150 nm thick n-PbSe top confinement layer, terminated by a 150 nm thick n-PbSe top cladding layer. During the MBE growth, the PbSe growth rate of 1.30 μm/hr. with a substrate temperature of 375 ºC was maintained. The streaky RHEED pattern observed from the laser structure during the MBE process shown in Fig. 3.8(b) confirmed the two-dimensional nature of the semiconductor multilayer growth on the PbSnSe substrate. Other relevant information about the MBE growth is detailed elsewhere[9]. The {110} PbSnSe substrates used to grow

76

lasing structures were p-type doped and had hole concentrations roughly around $\sim 4 - 8 \times 10^{18}$ /cm^3.
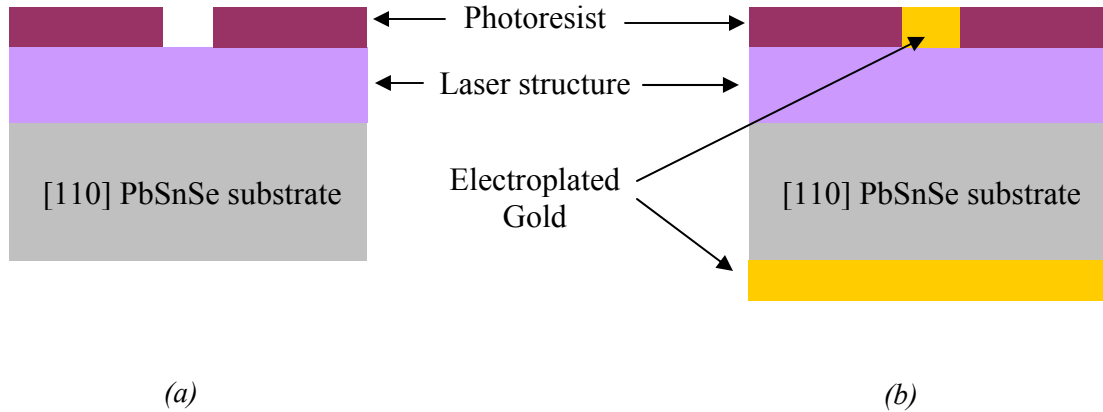
Fig. 3.10: Schematic diagram demonstrating processing steps during the fabrication of cleaved cavity lead salt laser on a [110] oriented PbSnSe substrate.

After the growth, the laser sample was thinned from the backside to approximately 230 μm. Thinning facilitates the cleaving, necessary for the formation of Fabry-Perot cavity mirrors. The laser sample was cleaved with lengths of approximately 300 μm along the natural cleavage (100) plane for lead salts, which intersects the (110) plane. The 20 μm stripe laser patterns were then created lithographically. Gold electroplating was carried out in order to a thick gold layer (thickness ~ 1 μm) required for the formation of top and bottom contacts. The mask aligner machine used to conduct all necessary photo-lithography procedures during the fabrication of lasing device is pictorially depicted in Fig. 3.11. The photolithographic steps are pictorially depicted in Fig. 3.10.

Fig 3.11: MAS 400 IR/VIS Mask Aligner in clean-room at OU for opto-lithography.
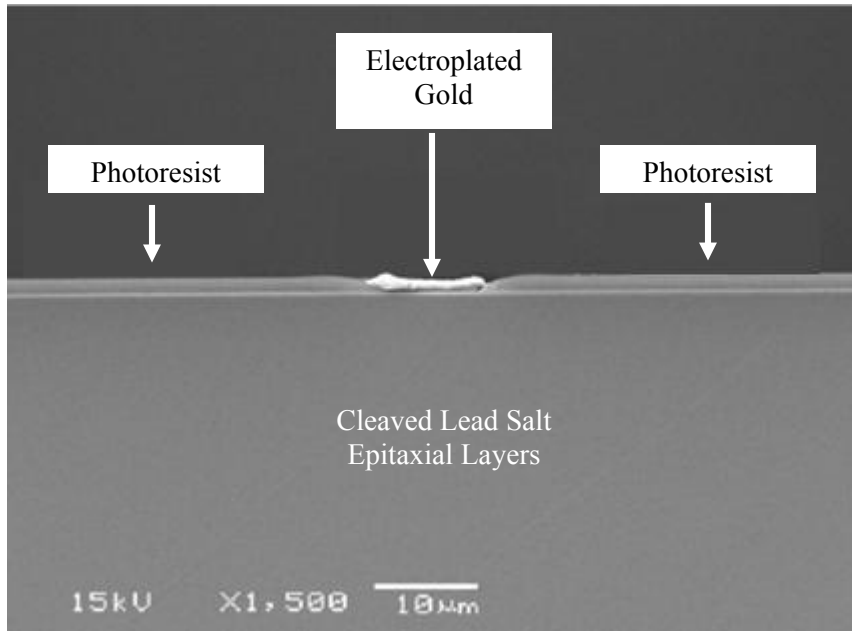
Fig 3.12: SEM image of cleaved cross section of a single laser chip with photoresist insulation.

The cleaving process for obtaining the Fabry-Perot lasing cavity was confirmed by the scanning electron microscope (SEM) image as shown in Fig. 3.12. It is important to note that the image was obtained from a dummy sample, it was not the same sample used for device measurement and characterization.
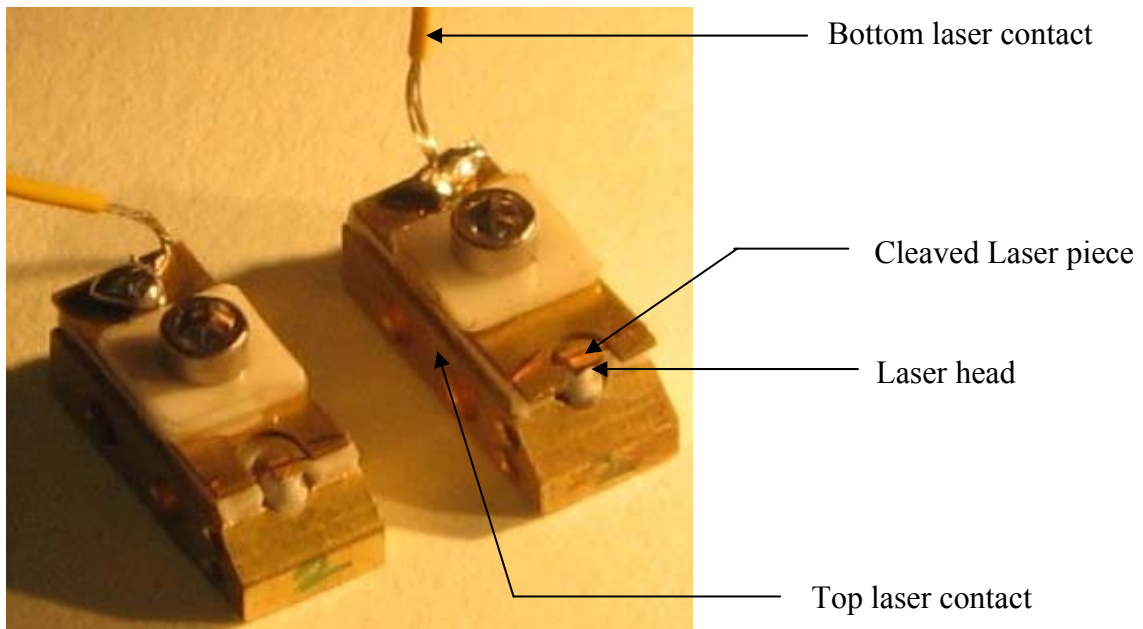
Fig. 3.13: Camera image of an edge emitting laser mounted on metallic housing.

After the cleaving process, the next step was mounting the single laser sample on top of a metallic laser head. A small solid copper pillar was chosen as the laser head as shown in Fig. 3.13. Indium electroplating was accomplished on the top surface of the copper pillar to enhance the adhesion of the laser piece with metal housing. The single laser sample was placed in an epi-side down fashion by vacuum tweezers on freshly indium-plated copper pillar. The process of mounting was thoroughly observed under

microscope. The bottom contact of the laser piece with housing was accomplished by indium-plated copper wire as illustrated in Fig. 3.13.

3.3.3. Lasing Device Characterization
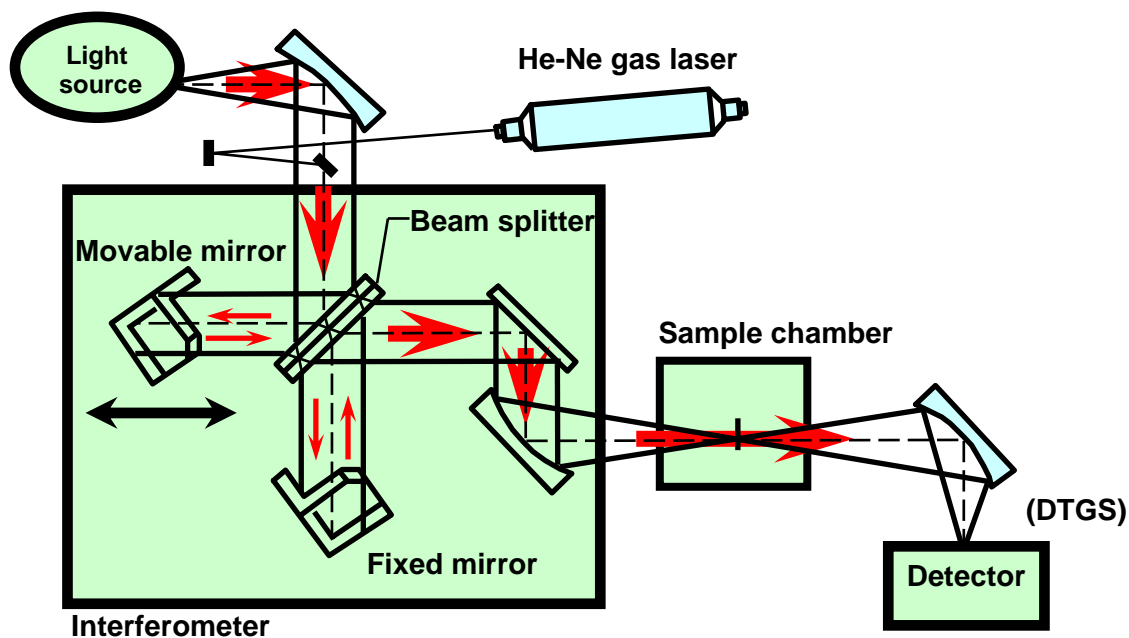
Fig. 3.14: Schematic diagram of the FTIR measurement set up in OU optical lab used for lasing device characterization.

The schematic diagram of a Fourier transform infrared (FTIR) spectroscopy system is pictorially depicted in Fig. 3.14. The working principle of FTIR spectroscopy is fundamentally based on the working methodology of Michelson interferometer, where one mirror is held in a fixed position relative to the beam splitter (BMS) and the second mirror scans back and forth relative to the BMS in a continuous manner. During the scanning, the path length of the infrared (IR) beam from the BMS to the moving mirror changes relative to the path length of the IR beam to the fixed mirror. These two IR

beams interfere at the other side of BMS and form an image at the detector. The Bruker IFS66/S FTIR measurement unit, equipped with a pulsed-mode and a continuous wave (CW) mode laser unit, in our OU optical lab, is illustrated in the Fig. 3.15.

Fig. 3.15: Bruker IFS66/S FTIR measurement system in OU optical lab.

Pulsed laser pumping was performed at a pulse repetition frequency (PRF) of 100 kHz, and the FTIR machine, equipped with a liquid nitrogen cooled Mercury-Cadmium-Telluride (MCT) photo-detector in conjunction with a pre-amplifier, was used to obtain time-resolved lasing spectra in step scan mode. The threshold current density was found to be 1.98 kA/cm^2, and it increased with increasing heat sink temperature. The device was excited with 500 ns width current pulses and the laser emission obtained from that above threshold was multimodal. At 77 K, the peak lasing emission wavelength was 5.8 μm at 350 mA injection current. A standard blackbody calibration was carried out to calibrate the emission power from the lasing device, and the collected data were plotted vs. injection current as shown in Fig. 3.16.
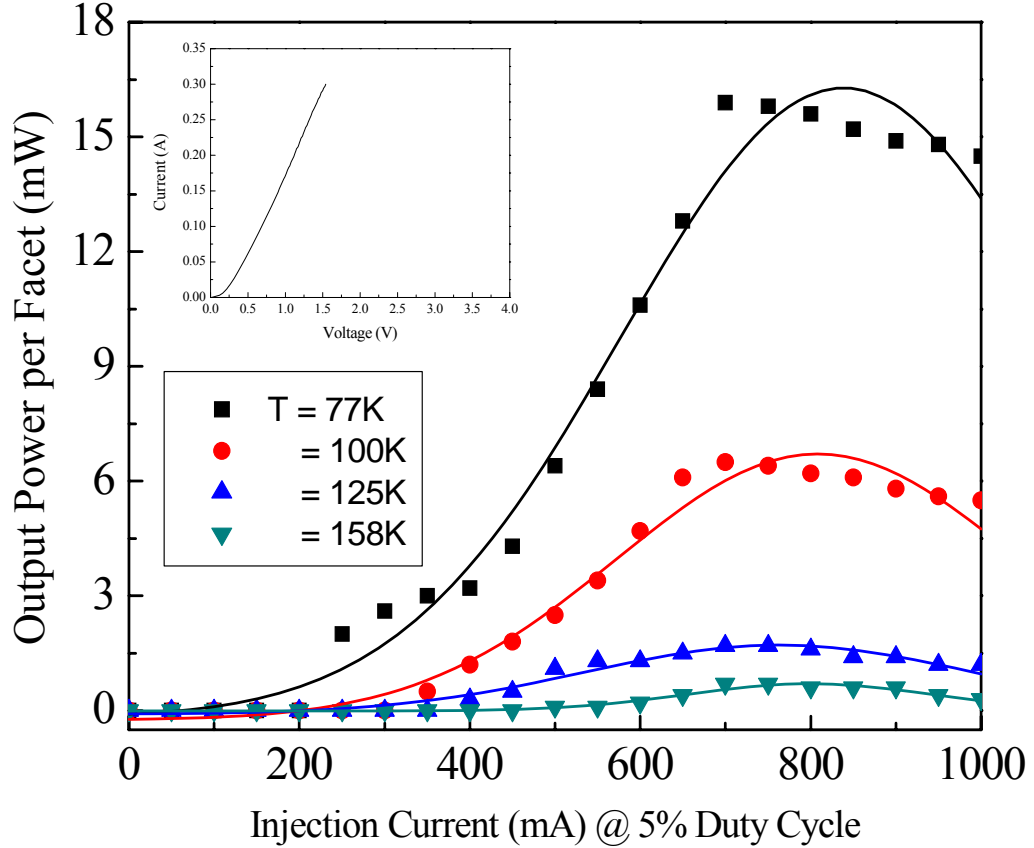
Fig. 3.16: Laser light output per facet vs. injection current (L-I) at several heat-sink temperatures. Inset: I-V characteristics of the laser diode at 77 K.

The inset provides the I-V characteristics of the device. The series resistance was measured to be 0.56 ohm. The lasing spectrum at λ = 5.2 μm at the highest achievable temperature of 158 K is shown in Fig. 3.17, from which the emission linewidth was determined to be 0.45 cm^{-1} when the device was excited by 500 mA current pulses. The larger value of linewidth can be attributed to the limitation of achieving a maximum FTIR optical resolution.
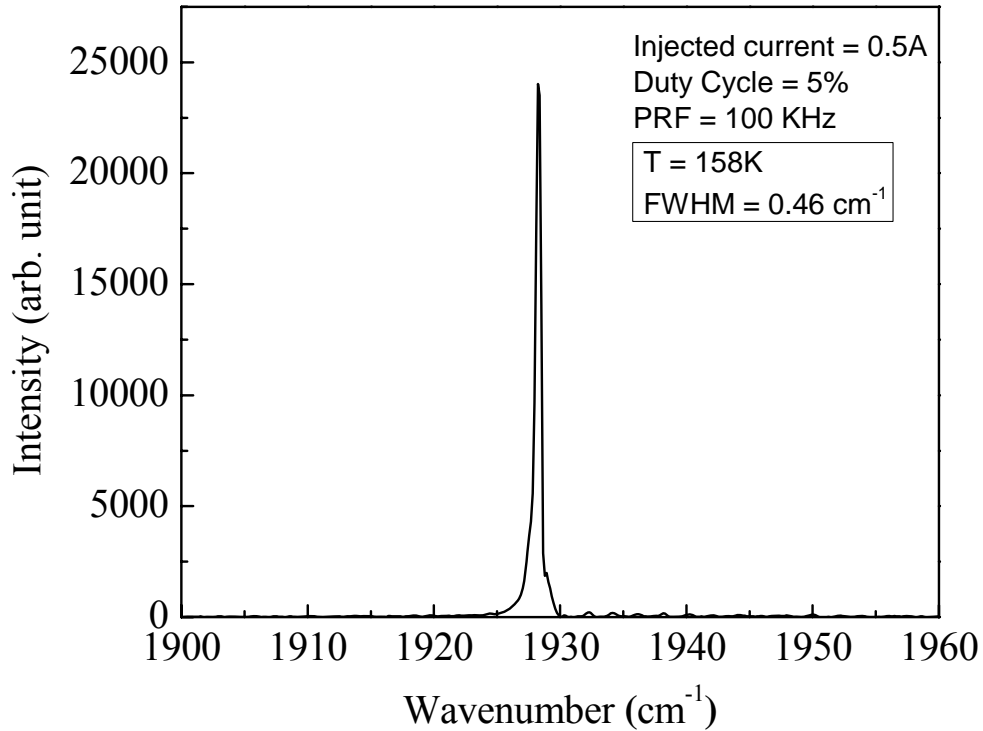
Fig. 3.17: Spectrum at 158 K of the laser structure of Fig. 3.9.

The peak laser emission shifted as the injection current increased. From the 350 to 800 mA current range, the tunability of peak emission was almost 0.14 cm^{-1}/mA, while above 800 mA, the tunability was 0.32 cm^{-1}/mA. The pulse-width was increased from 500 ns to 4.0 µs at a constant PRF of 100 kHz to observe the effect of it on laser emission. Emission power decreased with increasing pulse-width, and no emission was obtained above 4.0 µs i.e. 40% duty cycle of current pumping. Fig. 3.18 demonstrates a severe reduction in output optical power from the device at high value of pump duty cycle. The measured threshold current density was found to be as high as 2.3 kA/cm^2.
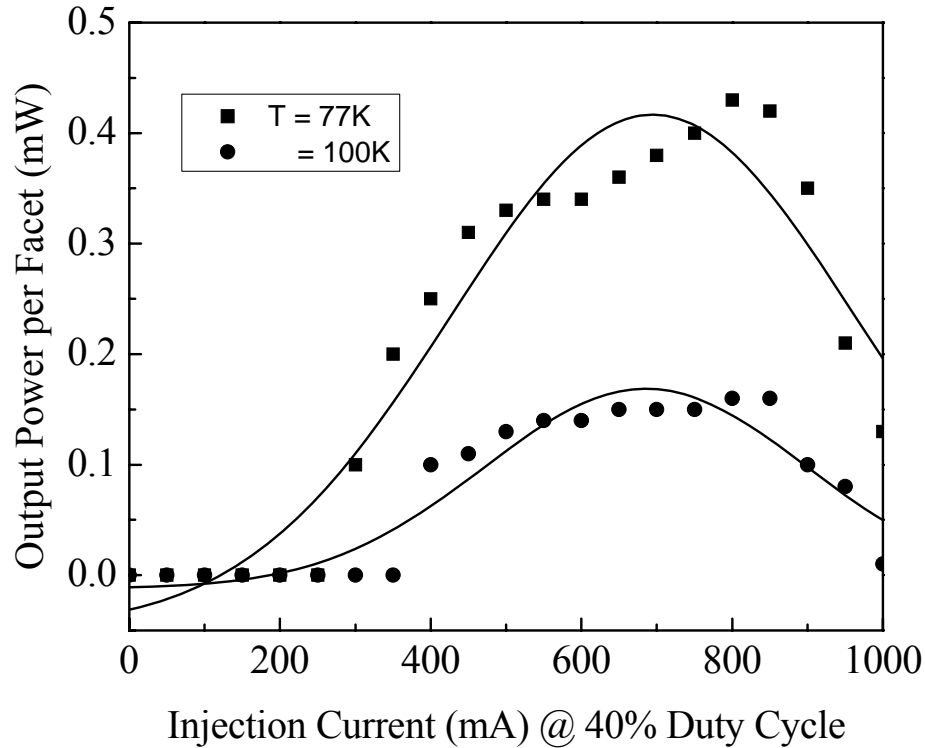
Fig. 3.18: Laser light output per facet vs. injection current (L-I) at T = 77 K and 100 K for a pump pulse-width of 4 µs.

3.3.4. Reliability of Lasing Emission

In order to examine the consistency and reliability of lasing emission over time, emissions were recorded from the device at different time intervals, keeping other parameters like heat-sink temperature and current injection constant. As shown in Fig. 3.19, the initial emission (black curve) was multi-modal. Even after the measurement was completed, the device was left on continuous current excitation so that the device had sufficient time for joule heating effects to take place. After 2 and 4 hrs time intervals, data collection was re-started, and at those times multi-modal lasing emission (blue curve) with a lesser number of peaks took place. Moreover, the maximum peak value

increased from the initially measured emission peak. When the time interval was increased to 14 and 16 hrs, no significant change (red curve) was observed in either the number of modes or the peak values.
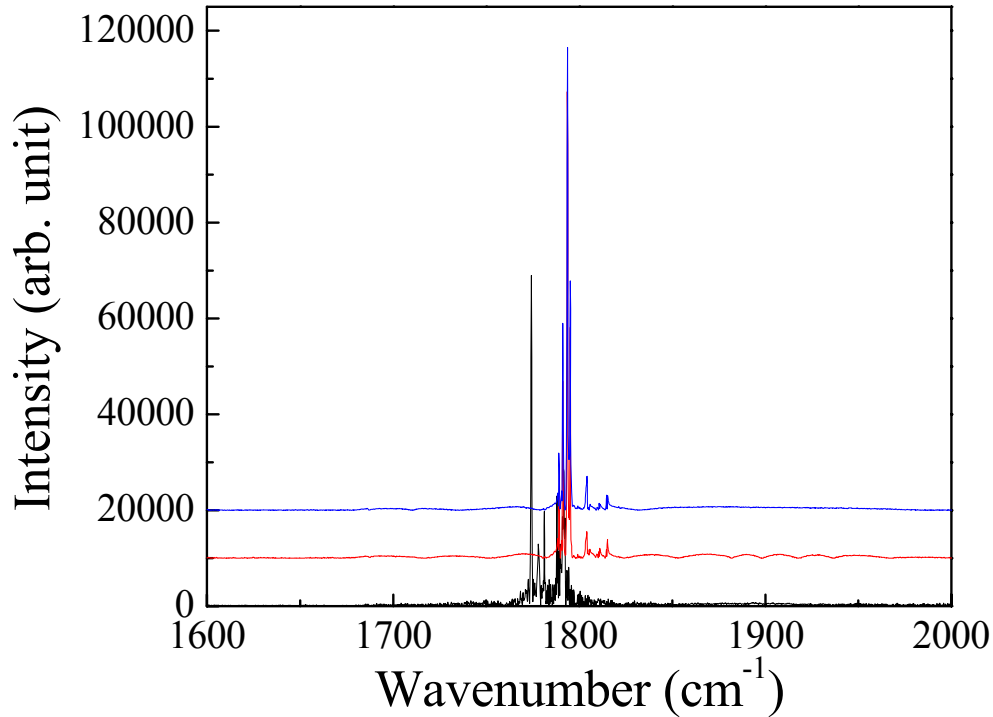
Fig. 3.19: Stimulated emission from the lasing device at different time intervals for a current injection of 500 mA at a 5% duty cycle and T = 100 K.

The total lasing power per facet was computed to be constant at ~ 2.43 mW, despite the change in the number of emission modes. As a plausible explanation, internal heat generation must have occurred in the sample which otherwise helped in shifting the modal emission from the IV-VI semiconductor structure. When the heat sink temperature was increased, the higher order lasing peaks underwent more loss compared to the lower order peaks. That should account for the smaller number of peaks obtained from the

lasing sample. Because the total emission power calculation (based on incorporating the integral area of all lasing modes) was found to be same, it can be inferred from the experiment that the emitted lasing power from IV-VI laser was indeed consistent with time.

3.4.   Fabrication of Free-standing Microstructures

3.4.1   Background

In this section, I would describe our recent progress in fabricating novel micro-sized IV-VI QW structures which have vast applications in the field of micro-electromechanical systems (MEMS) that demands free standing micro-sized objects in various shapes and sizes. All these applications necessitate the requirement of precisely controlled thickness of epi-layers with smooth and uniform surfaces. This can be achieved by already well-established thin film deposition schemes such as molecular beam epitaxy (MBE) and metal-organic chemical vapor deposition (MOCVD). The experimental studies conducted by myself have been described here.

A controlled release of the thin film, grown by these deposition processes, from the substrate creates miniaturized objects for various device applications. This yielding of thin film from the substrate depends on the mismatch between the lattice parameters as well as temperature coefficients of expansion of the constituent epitaxial layers in the multilayer semiconductor structures and thereby an inherent biaxial strain[10] is generated. This strain has a significant effect on the electronic band structure[11] of the superlattice semiconductor. The geometry of these novel objects can be engineered by suitably

defining the discrepancy among internal stresses generated in multilayered thin films with the help of some fundamental processing parameters. The internal stress itself depends on the thickness of individual layer and etching environment which the sample has undergone. Micro and nano structured devices based on III-V semiconductors are already quite well realized in both industry as well as research fields. The fundamental theory for fabrication of such miniaturized structures is based on very popular "general" method[12]. Recently, by adapting this technological aspect, we could fabricate micro-sized rods and tubes on IV-VI semiconductor materials[13] [14]. The large surface area to volume ratio assists in heat dissipation, which is of utmost importance for IV-VI semiconductor because of their low thermal conductivity. The large refractive index of these materials can be useful in obtaining more optical confinement when used as waveguide. Recently, it was shown that the microstructure dimensions were a strong function of fabrication environment such as etching time, temperature etc[15].

3.4.2 Pulsed Mode Photoluminescence (PL) Emission from MQW Micropillars

Another important phase of those microfeatures included is the wavelength-sized micropillars[16] [17] [18] [19]. Compared to other geometries of such micro-sized devices, micropillars have the advantages of larger photon collection efficiencies and their wavelength-size microcavities. The free standing micropillar arrays based on the lead salt materials were manufactured with the purpose of better heat dissipation during their high temperature operations as efficient mid-infrared light emitters.
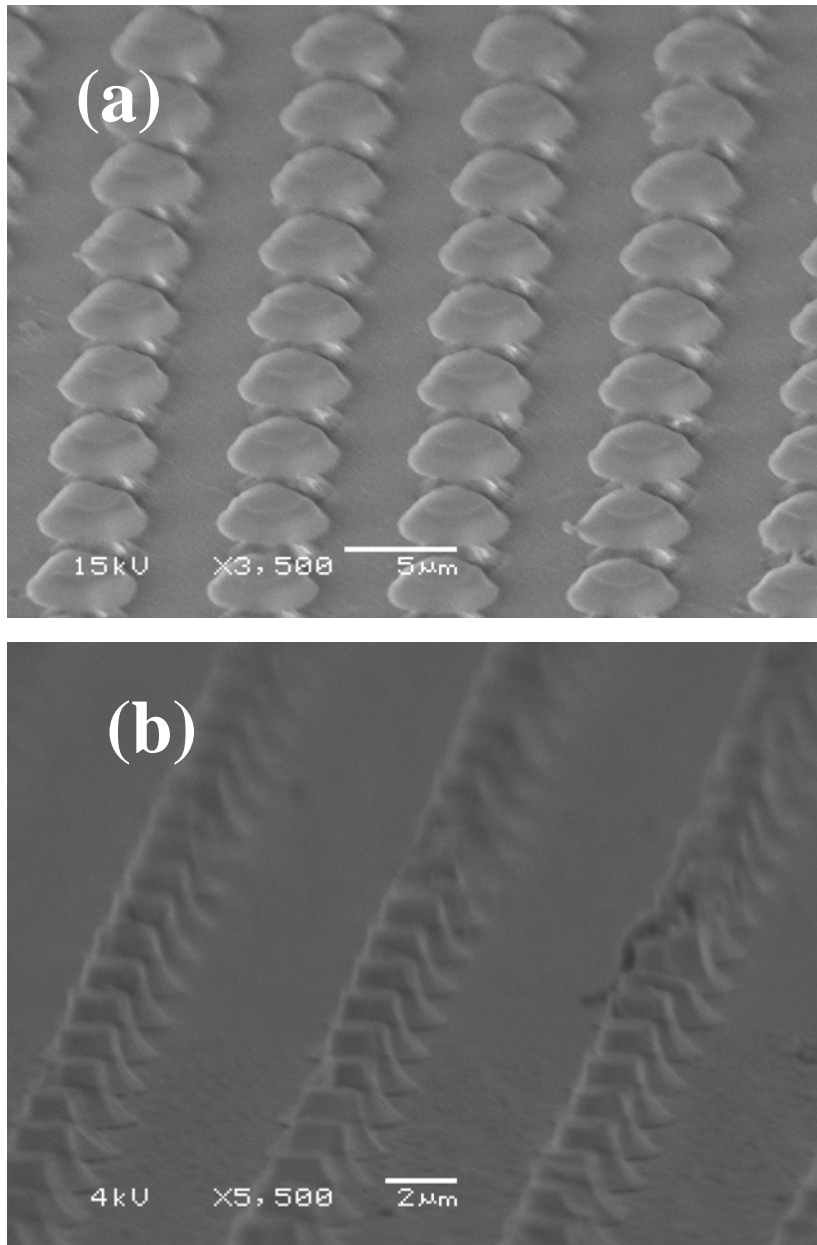
Fig. 3.20: SEM micrographs of the lead salt micropillar arrays of diameter 5.0 μm and inter-pillar spacing of 8.0 μm both (a) with photoresist, (b) without photoresist.

The micropillar sample was grown by molecular beam epitaxy (MBE) on BaF$_2$(111) substrate[20]. The as-grown sample consists of a 20 pair PbSe/Pb$_{0.97}$Sr$_{0.03}$Se multiple quantum well (MQW) structure. The epi-layer consisted of a multiple quantum well structure with a 22 nm thick PbSe quantum well and 25 nm thick Pb$_{0.97}$Sr$_{0.03}$Se barrier layer. After photolithography and consequent processing steps, pillars were formed on the epi-layer. The spacing between individual pillars (with an etching height of ~ 940 nm as shown in Fig. 3.20) was 8 μm, where the diameter of each pillar was 5 μm.
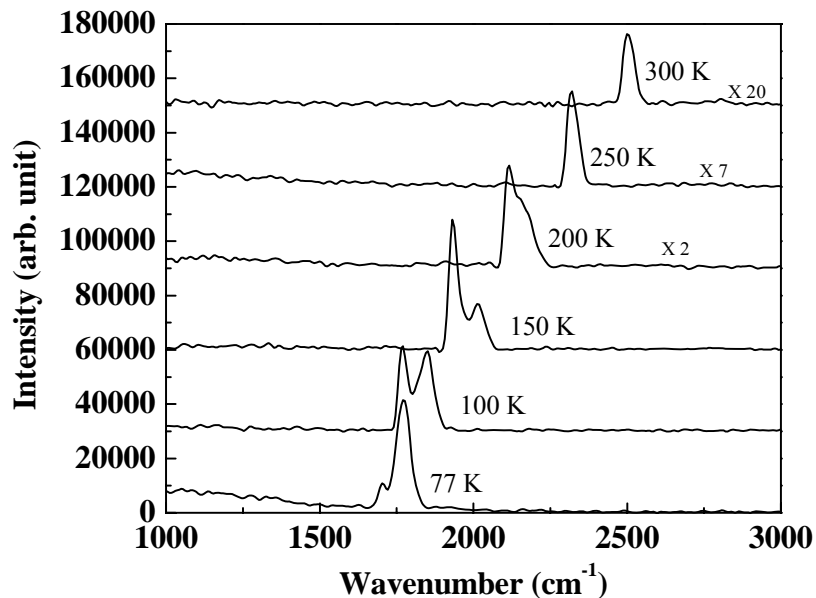
Fig. 3.21: PL spectra of micropillar array (pillar diameter = 5 μm and inter-pillar distance = 8 μm) at several heat-sink temperatures (Intensity at 200 K, 250 K and at 300 K were multiplied by 2, 7 and 20 times respectively).

The pulsed photoluminescence measurements on such pillar array were carried out at different heat sink temperature and were plotted in Fig. 3.21. The figure[21] exhibits a consistent blue-shifting of photoluminescence peak with the increase in heat sink temperature. The temperature tunability at the emission wavelength obtained from the

pillar sample was ~ 3.62 cm^{-1}/K. The trend of the reduction of spontaneous emission coming from the pillar sample with the corresponding reduction in temperature was noted. The linewidth was 49.16 cm^{-1} at 77 K, and this reduced to 34.27 cm^{-1} at 300 K. The strong PL emission emanating from the sample together with the regular PL peak shift with temperature indicated the MBE growth quality of the epi-layer was retained in the micropillar sample.

3.4.3 Fabrication of Lead Salt Microtubes and Microrods

Top PbSe layer rolling due to BaF$_2$ sacrificial layer etching at higher temperature

BaF$_2$ etched from side resulting in PbSe buffer layer rolling
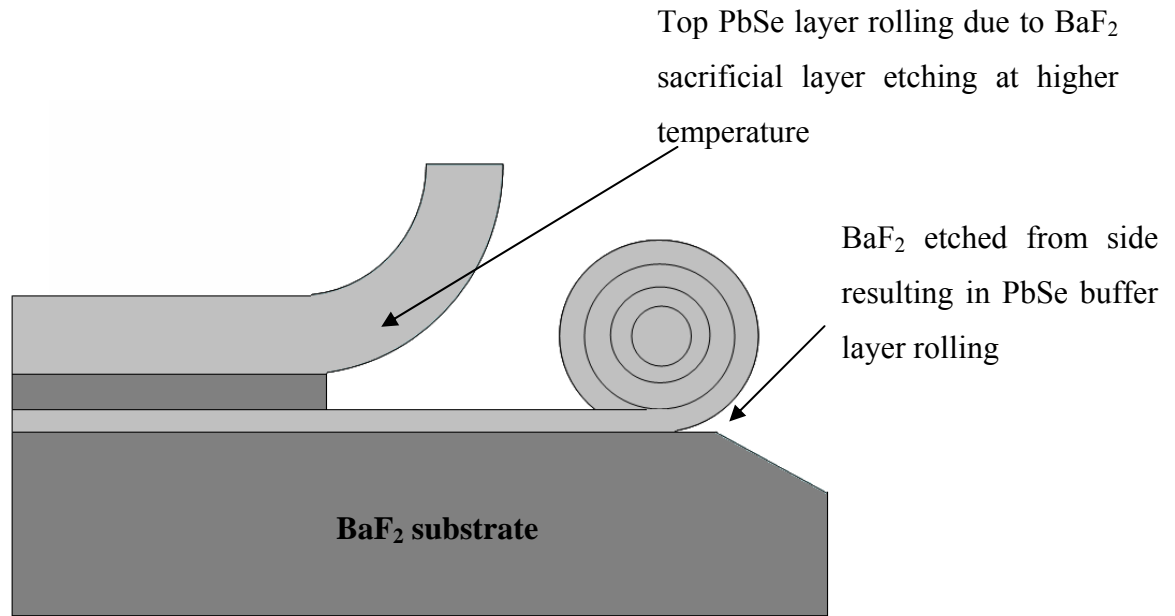
BaF$_2$ substrate

Fig. 3.22: Schematic diagram of microtube or microrod formation.

Lead salt epi-layers of various thicknesses are grown on a polished (111) BaF$_2$ substrate. The entire multilayer structure generally consists of a thin PbSe buffer layer (~ 0.7 μm) as well as a thin BaF$_2$ (~ 0.4 μm) sacrificial layer. The sacrificial layer of BaF$_2$,

lattice-matched with the PbSe layer, could be etched with DI water, and as a result, the top single-crystalline PbSe layer will roll-up taking the shape of microtubes/rods as illustrated elsewhere[22]. At low temperature, BaF_2 substrate etched away more from the edges of the sample and thereby the PbSe buffer layer started rolling into micro-cylinders but due to the slower etching rate of BaF_2 sacrificial layer top PbSe layer only grew cracks on it. But upon increasing the DI water temperature, the etching rate of the sacrificial layer enhances resulting in the folding back of top PbSe layer into rods. Wet etching of BaF_2 layer guiding to the microtube/rod building is pictorially depicted in Fig. 3.22. The change in such microcylinder dimension can be achieved by suitable alteration of initial epitaxial layer thickness and etching time.

3.4.4   Optical Characterization of Microtubes/rods

In order to carry out the optical characterization, a single free-standing microrod of 342.96 μm long with a diameter of 17.28 μm is glued by silver paste on copper ribbon (Fig. 3.23(a)) in order to have means for heat dissipation during the measurement at room temperature. Pulsed PL excitation is then carried out by a 1.064 μm Nd:YAG laser (τ_{pulse} = 30 ns, pulse repetition rate = 10 Hz) which generates TEM_{00} mode incident normally on the sample surface.

The lasing power density is 44.31 kW/cm^2 and the spot-size of the laser was focused to 5.0 mm, with the help of a 2″-diameter CaF_2 lens, which is well enough to cover the entire area of the sample. The PL emission is collected at a resolution of 16 cm^{-1} onto InSb detector, cooled by liquid nitrogen through a series of optical mirrors, perpendicular to the rod axis and parallel to the direction of excitation. Measurements are

accomplished on various places on both the microrod as well as its reference sample (before processing of rods) in order to judge the repeatability of the results. There has been 4.01 times reduction in the PL intensity from the rod sample compared to its reference as seen from Fig. 3.23(b). The excited surface area of the reference sample (19.63×10^6 μm^2) is calculated to be 2563 times larger than that of the microrod sample (7659.86 μm^2).
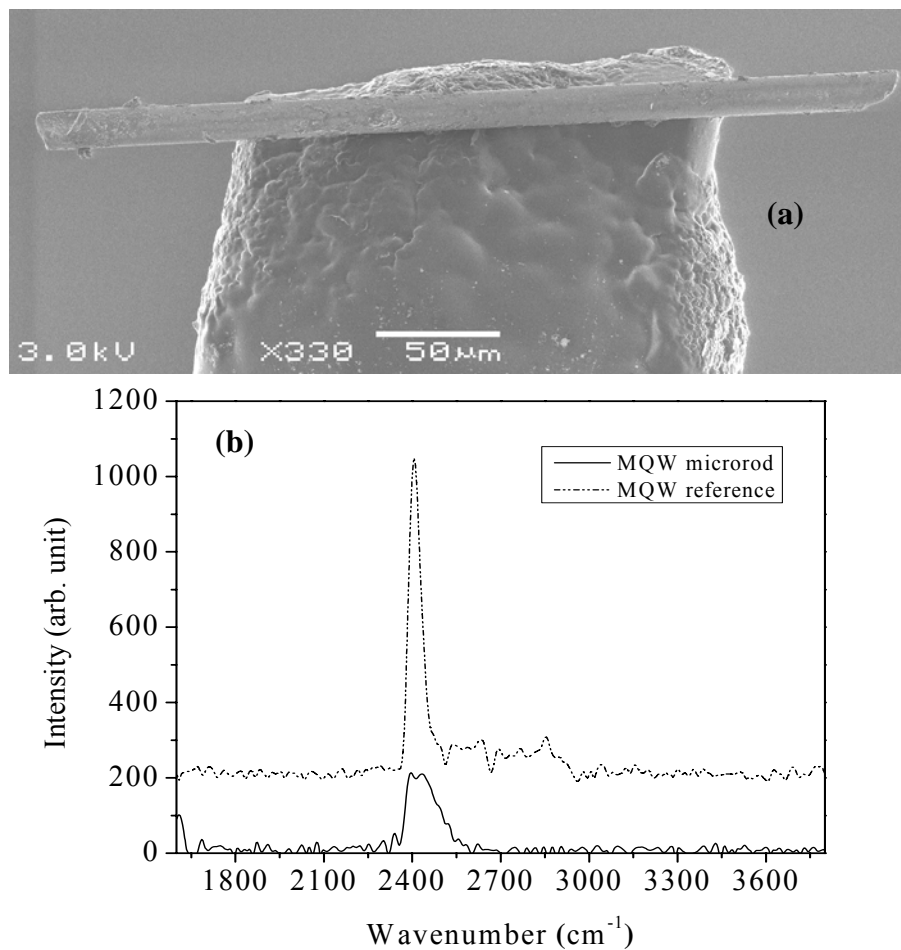
Fig. 3.23: (a) SEM micrograph of the microrod mounted on copper ribbon with silver paste during its optical characterization, (b) PL spectra from mounted MQW microrod and its reference sample.

In case of cylindrical morphologies compared to its planar counterpart, there is always an enhancement factor of ten[23] in light extraction efficiency due to the internal reflection occurring inside the structure itself from various facets formed on their own. Thus by taking all these things into considerations and also assuming that the total emitted light from the sample is collected at the detector, there is a confirmed enhancement by 64 factor[24] in pulsed PL power density from microrod. Although there have not been adequate theories to account for this huge intensity gain factor, this is undoubtedly promising for future high power opto-electronic devices.

One of the major applications of mid-infrared opto-electronic devices is in the field of chemical and industrial gas sensing[25] [26] [27]. A large number of fundamental molecular vibrations as well as most of the first overtones take place in the mid-infrared region (2.5 - 25 μm) of electromagnetic spectrum. The nature of the spectral bands in this frequency region is likely to be sharp, distinct and have very high values of absorption coefficients; thereby leaving specific "footprint" for individual small gas molecule in the mixture. Therefore this necessitates manufacturing novel devices that show narrow and sharp PL peak at room temperature. This can be achieved by utilizing the well-established fiber-optics technology which not only restrict the light by the virtue of its waveguide nature but also improves signal power by boosting the signal to noise ratio. This is illustrated by comparing the pulsed PL spectra from a single microtube both before and after inserting in a hollow quartz fiber.
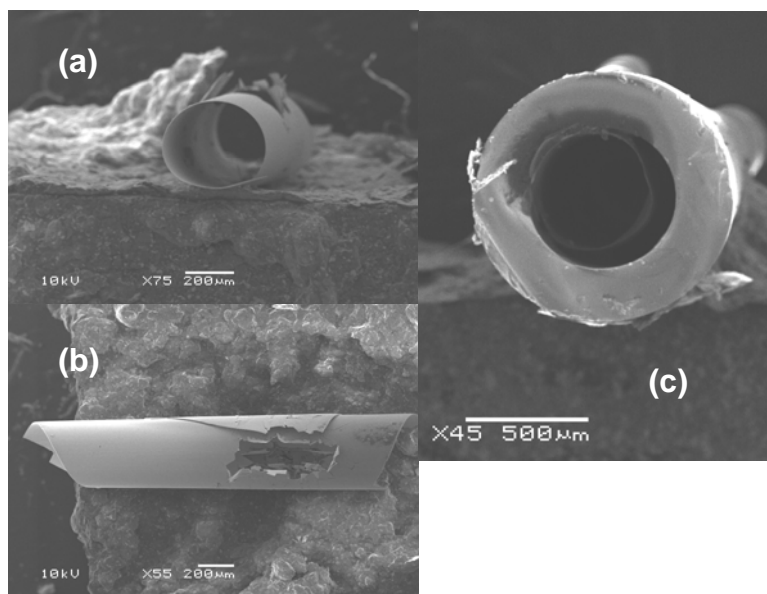
Fig. 3.24: SEM images of MQW microtube (a) cross-section, (b) surface (some portions damaged due to high-power laser excitation), (c) cross-sectional view of microtube inserted inside silica fiber.
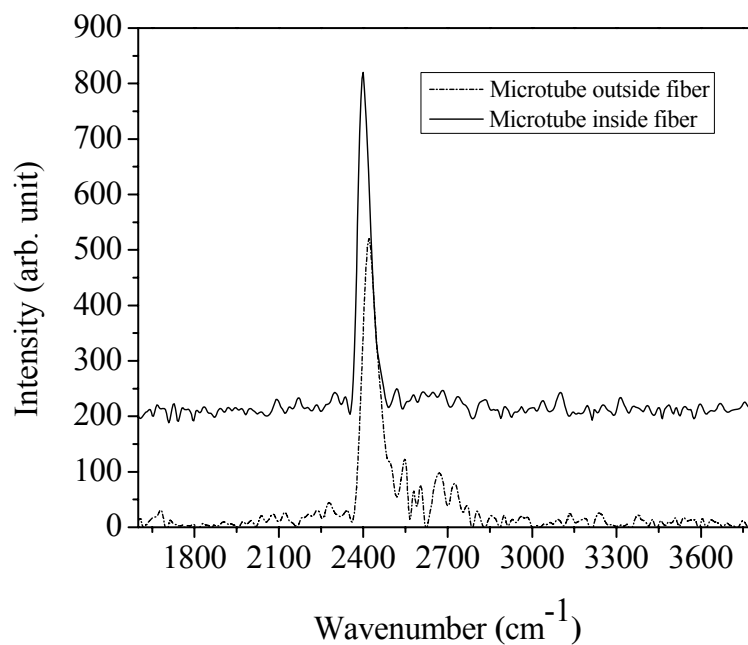
Fig. 3.25: Comparative analysis of photoluminescence spectra at room temperature from MQW microtube inserted inside silica glass fiber as well as outside fiber.

94

SEM images of the morphological views of microtube (diameter = 480 μm) both outside and inside of hollow quartz fiber (diameter = 1051.11 μm) are shown in Fig. 3.24. The pulsed lasing power used for optical characterization is 397.33 kW/cm^2. The emitted light from the microtube samples is collected parallel to the rod axis and perpendicular to the direction of excitation. Fig. 3.25 describes an increase of the light emission by a factor of 1.19 together with a narrower linewidth of PL peak due to the optical confinement nature of glass fiber. These all signify that the microstructures are very robust in nature and they can be easily handled while implementing into any devices. The increment in light emission power coupled with the reduction in optical linewidth is obviously encouraging for mid-infrared industrial and research applications.

3.5.   Conclusions

The modern epitaxial technology that allows high quality alternating material growth and advanced laser concepts is resurrecting IV-VI mid-IR lasers. The [110] and [111] oriented QW laser structure combined with much improved substrate thermal conductivity as well as the low Auger recombination promise the success of the lead-salt mid-IR lasers. The noteworthy success in mid-IR opto-electronic research based on lead salt QW structures holds the promise of a compact, highly efficient laser/detector system in the not too distant future. Recent developments in the experimental studies on lead salt materials mostly on lattice matched BaF$_2$ substrates are mentioned. First time achievement of an electrically excited edge emitting QW laser on PbSnSe substrate is described. Novel fabrications of free standing microstructures in the form of rod, tube and pillar, having vast applications in MEMS and NEMS, are reported. These light

emitting devices will eventually lead to many applications such as a high efficiency, field-portable, mid-IR laser spectroscopy systems.

3.6.   References

[1] J. F. Butler, A. R. Calawa, R. J. Phelan, Jr., T. C. Harman, A. J. Strauss, and R. H. Rediker, "PbTe Diode laser," *Appl. Phys. Lett.*, vol. 5, pp. 75-77, 1964.

[2] Z. Shi, X. Lv, F. Zhao, A. Majumdar, D. Ray, R. Singh, X. J. Yan, "[110] Orientated lead salt midinfrared lasers," *Appl. Phys. Lett.*, vol. 85, pp. 2999-3001, 2004.

[3] H. Zogg and A. Ishida, Infrared Detectors and Emitters: Materials and Devices, Chapter-3, Ed. Peter Capper, C. T. Elliott, Springer, 2000.

[4] F. Zhao, X. Lu, J. C. Keay, D. Ray, R. Singh, A. Majumdar, X. Yan, Z. Shi, "MBE growth and characterization of IV-VI semiconductor thin-film structures on (1 1 0) BaF_2 substrates," *J. Crys. Growth*, vol. 285, pp. 54-58, 2003.

[5] J. E. Ayers, "The measurement of threading dislocation densities in semiconductor crystals by X-ray diffraction," *J. Crys. Growth.*, vol. 135, pp. 71-77, 1994.

[6] A. Majumdar, H. Z. Xu, S. Khosravani, F. Zhao, L. Jayasinghe, Z. Shi, "High power light emission of IV–VI lead salt multiple-quantum-well structure grown by molecular-beam epitaxy on <111> BaF_2 substrate," *Appl. Phys. Lett.*, vol. 82, pp. 493-495, 2003.

[7] S. Mukherjee, D. Li, D. Ray, F. Zhao, S. L. Elizondo, S. Jain, J. Ma, Z. Shi, "Fabrication of an Electrically Pumped Lead-Chalcogenide Mid-Infrared Laser on a [110] Oriented PbSnSe Substrate," *IEEE Photon. Technol. Lett.*, vol. 20, pp. 629-631, 2008.

[8] D. Ray, Ph.D Dissertation, University of Oklahoma, 2007.

[9] A. Majumdar, H. Z. Xu, F. Zhao, J. C. Keay, L. Jayasinghe, S. Khosravani, X. Lu, V. Kelkar, and Z. Shi, "Bandgap energies and refractive indices of Pb1–xSrxSe," J. Appl. Phys., vol. 95, pp. 939-942, 2004.

[10] K. Kubota, P. O. Vaccaro, N. Ohtani, Y. Hirose, M. Hosoda, T. Aida, "Photoluminescence of GaAs/AlGaAs micro-tubes containing uniaxially strained quantum wells," *Phys. E*, vol. 13, pp. 313-316, 2002.

[11] M. Grundmann, "Nanoscroll formation from strained layer heterostructures," *Appl. Phys. Lett.*, vol. 83, pp. 2444-2446, 2003.

[12] O. G. Schmidt, N. Y. Jin-Phillipp, "Free-standing SiGe-based nanopipelines on Si (001) substrates," *Appl. Phys. Lett.*, vol. 78, pp. 3310-3312, 2001.

[13] A. Majumdar, Z. P. Guan, F. Zhao, D. Li, D. Ray, S. Jain, S. Mukherjee, Z. Shi, "Fabrication of freestanding semiconductor multiquantum-well microtubes," *Appl. Phys. Lett.*, vol. 88, pp. 171111-1-3, 2006.

[14] S. Jain, S. Mukherjee, Z. P. Guan, D. Ray, F. Zhao, D. Li, Z. Shi, "Fabrication of free-standing PbSe micro-rods," *Phys. E*, vol. 39, pp. 120-123, 2007.

[15] S. Mukherjee, S. Jain, F. Zhao, J. P. Kar, D. Li, Z. Shi, "Strain oriented microstructural change during the fabrication of free-standing PbSe micro-rods," *J. Mat. Sc. Mat. Electron.*, vol. 19, pp. 237-240, 2008.

[16] B. Gayral, J. M. Gerard, A. Lemaitre, C. Dupuis, L. Manin, J. L. Pelouard, "High-*Q* wet-etched GaAs microdisks containing InAs quantum boxes," *Appl. Phys. Lett.*, vol. 75, pp. 1908-1910, 1999.

[17] J. P. Reithmaier, G. Sek, A. Loffler, C. Hofmann, S. Kuhn, S. Reitzenstein, L. V. Keldysh, V. D. Kulakovskii, T. L. Reinecke, A. Forchel, "Strong coupling in a single quantum dot-semiconductor microcavity system," *Nat.*, vol. 432, pp. 197-200, 2004.

[18] L. A. Graham, D. L. Huffaker, D. G. Deppe, "Spontaneous lifetime control in a native-oxide-apertured microcavity," *Appl. Phys. Lett.*, vol. 74, pp. 2408-2410, 1999.

[19] D. G. Deppe, L. A. Graham, D. L. Huffaker, "Enhanced spontaneous emission using quantum dots and an apertured microcavity," *IEEE J. Quant. Electron.*, vol. 35, pp. 1502-1508, 1999.

[20] S. Mukherjee, S. Jain, F. Zhao, J. P. Kar, Z. Shi, "Photoluminescence studies from micropillars fabricated on IV-VI multiple quantum-well semiconductor structure," *J. Microelec.*, vol. 38, pp. 1181-1184, 2007.

[21] S. Mukherjee, S. Jain, J. P. Kar, Z. Shi, "Superior performances from fabricated microstructures on MBE-grown IV-VI lead salt materials for mid-infrared applications," *2007 International Workshop on Physics of Semiconductor Devices*., pp. 413-416, 2007.

[22] O. G. Schmidt, K. Eberl, "Erratum: Thin solid films roll up into nanotubes," *Nat.*, vol. 412, pp. 42, 2001.

[23] J. Nurnus, U. Vetter, J. Koenig, R. Glatthaar, A. Lambrecht, F. Weik, J. W. Tomm, "Optically pumped mid infrared emitters built using surface structured PbSe epitaxial layers," *Proceedings of the SPIE*., vol. 5840, pp. 212-220, 2005.

[24] S. Mukherjee, S. Jain, F. Zhao, J. P. Kar, D. Li, Z. Shi, "Enhanced photoluminescence from free-standing microstructures fabricated on MBE grown PbSe–PbSrSe MQW structure," *Microelec. Eng.*, vol. 85, pp. 665-669, 2008.

[25] D. Weidmann, F. K. Tittel, T. Aellen, M. Beck, D. Hofstetter, J. Faist, S. Blaser, "Mid-infrared trace-gas sensing with a quasicontinuous-wave Peltier-cooled distributed feedback quantum cascade laser," *Appl. Phys. B*, vol. B79, pp. 907-913, 2004.

[26] D. Richter, D. G. Lancaster, R. F. Curl, W. Neu, F. K. Tittel, "Compact mid-infrared trace gas sensor based on difference-frequency generation of two diode lasers in periodically poled LiNbO$_3$," *Appl. Phys. B*, vol. B67, pp. 347-350, 1998.

[27] S. McCabe, B. D. MacCraith, "Novel mid-infrared LED as a source for optical fibre gas sensing," *Elect. Lett.*, vol. 29, pp. 1719-1721, 1993.

CHAPTER 4

PHOTONIC BANDGAP DEFECT STRUCTURE: CAVITY WITHOUT CLEAVING

4.1.   Background

For a few decades, lead chalcogenide diodes have been one of the most popular and commercially available semiconductor MIR lasers. However, due to the low operating temperatures and low external efficiencies, the performances of lead salt lasers could not reach the desired level. Even at low cryogenic heat-sink temperature, lasing output powers for single mode operation are less than a few mWs. Moreover, an affinity towards multimodal operation and mode hopping is quite familiar. The threshold level of laser operation for IV-VI materials is enhanced due to the existence of four-fold L-valley degeneracy near band extrema. The degeneracy does not get lifted off for [100] orientation which is the most common growth orientation for QW laser structures. This, in turn, limits exploiting the supreme advantages of lead chalcogenide materials for high temperature and long wavelength operation, i.e., reduced threshold level originating from a low nonradiative recombination rate. Also, [100] growth orientation leads to inferior epitaxial material quality because it does not allow the dislocation gliding phenomenon.

From Chapter 2, it can be seen that the QW gain threshold is minimum for [111] lead salt crystal orientation compared to its other two counterparts. Therefore, this orientation is more suitable for higher temperature laser operation of lead salt materials. Experimentally lead salt vertical cavity surface emitting laser (VCSEL) grown on (111)

BaF$_2$ substrate[1] have exhibited superior performance. Those VCSELs have demonstrated pulsed-mode operation near room temperature. Lasing output power as high as 300 mW and threshold density as low as 10.5 kW/cm^2 were achieved[2]. Pulsed laser emission at elevated temperature from VCSELs on a (111) substrate was obtained[3] [4]. The continuous wave (CW) lasing at 4.03 µm was observed up to 230 K. The minimum value of threshold excitation density of 2.6 kW/cm^2 has been measured at 190 K, 65 °C lower than that of the pulsed operation.

However, the design complexity of distributed Bragg reflectors (DBRs) during MBE fabrication and low power operation severely limit the popularity of VCSELs while realizing long wavelength and high power lasing devices. The best growth substrate for realizing high temperature devices is silicon (Si). Si (thermal conductivity = 1.56 W/cm K) has almost 78 times higher thermal conductivity than lead salt materials (thermal conductivity = 0.02 W/cm K) at 300 K. Moreover, by using Si one can reduce manufacturing cost of device fabrication as well as avail of the established device fabrication technologies on this substrate. Unlike lead salt materials, the natural cleavage plane for Si is (111). Therefore, in order to fabricate a lasing device, there is a necessity to adopt some valid technology which does not undergo a cleaving process while making a Fabry-Perot resonating cavity.

The best solution in this regard is achieved by implementing the idea of well-known photonic bandgap (PBG) methodology. The physics of PBG does not depend on crystal growth orientation. The PBG scheme demonstrates a perfect optical analogy of the semiconductor bandgap where the electric potential distribution is governed by a

periodicity of regularly distributed lattice dielectric medium (mainly air) in another highly contrasting dielectric medium. This helps in the confinement of light modes by creating a specific frequency bandgap which in other ways opens a new horizon of tailoring the light-matter interaction in the crystal lattice. Due to the existence of the bandgap effect in photonic crystals, optical waves corresponding to the bandgap frequency are forbidden[5] to propagate whereas waves outside this range are allowed to propagate. This basically provides a provision for suitably engineering the crystal design and localizing light modes within a semiconductor slab. The size of the bandgap is determined by two factors: the dielectric contrast of the constituent materials that build up the photonic crystal and the higher dielectric material filling fraction[6]. Several research studies[7] [8] [9] [10] [11] regarding photonic crystal fabrication and characterizations in the semiconductor structure are cited in the literature.

4.2. Introduction

A periodic arrangement of atoms and molecules is known as a crystal. If a tiny basic building block of atoms or molecules is repeated in space, a crystal lattice structure will be formed. Quite similar to the crystal structure, if the dielectric constant of a material system is periodically altered in space it is known as a photonic crystal (PC). It is well known that all semiconductor materials have a specific energy bandgap between the conduction and valence band. Electrons and holes are "forbidden" to occupy any energy level within the bandgap. In a similar way, a photonic crystal possesses a "forbidden" frequency band in which no propagation of electromagnetic waves is possible. Based on the number of directions the dielectric periodicity is exhibited, a one-,

two-, or three- dimensional photonic crystal or photonic bandgap structure is generated. Light scattering occurring inside a PBG structure can produce many photonic phenomena analogous to the electronic behavior inside crystals.

A PBG crystal structure is analogous to a normal crystal lattice in terms of atomic periodicity, except that the periodicity is of the order of a micrometer rather than a fraction of a nanometer. The implementation of the PBG effect to achieve a semiconductor laser by controlling spontaneous emission was demonstrated by Yablonovitch in 1987[12]. The fundamental idea behind the concept was to design a photonic structure in order to originate a frequency bandgap that coincides with the semiconductor spontaneous emission. Since that time, the concept of PBG phenomena is well adopted and practiced all over the world. Various significant applications[13] [14] [15] of PBG phenomena are noticed to obtain millimeter and microwave frequencies in order to achieve desired performances for antennas and waveguides.

4.3.   Finite Difference Time Domain (FDTD) Method

The FDTD method is a well established mathematical analysis tool which is extensively implemented for integrated and diffractive optical device simulations. Through rigorous and accurate numerical solution of electromagnetic Helmholtz's equations, this methodology helps in modeling light propagation, diffraction and scattering phenomena, and polarization and reflection effects inside a crystal. It also assists in modeling material anisotropy and dispersion without the requirement of any presumed field behavior. The FDTD method is a very powerful simulation tool that provides effective analysis of sub-micron devices with very finite structural details. The

miniaturization of device dimension helps in light confinement and consequently, the large dielectric constant difference of the semiconductor materials to be implemented in a typical device design.

4.4. Two Dimensional FDTD Equations

Opti-FDTD software is implemented to perform the FDTD simulation for the lead salt PBG structure. The FDTD methodology is fundamentally based on numerical solutions to electromagnetic Helmholtz's equations. As shown in Fig. 4.1, the photonic structure is arranged in the X-Z plane[16]. The light propagation inside the device is considered to be along the Z-direction. The Y-direction is considered to be infinite. This fundamental approximation removes all the $\partial/\partial y$ partial derivatives from electromagnetic Maxwell's equations and divides them into two independent sets of numerical equations. These are known as transverse electric (TE) and transverse magnetic (TM) equations.
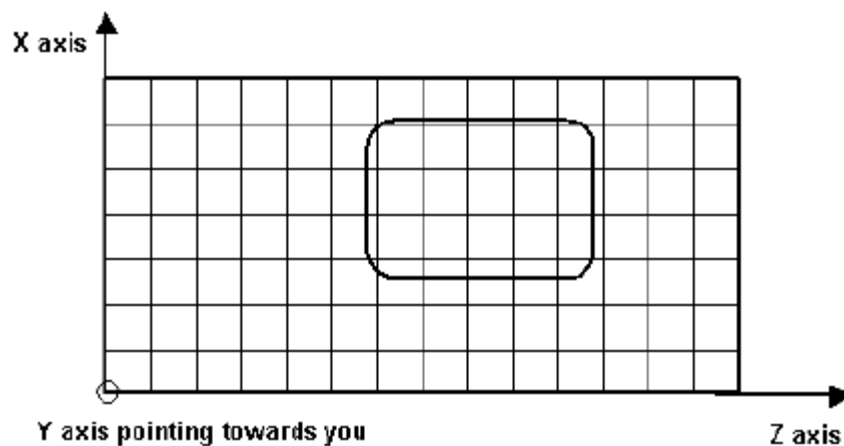
Fig. 4.1: Numerical representation of the 2D computational domain.

The spatial steps in the X- and Z-directions are designated as Δx and Δz, respectively. Each mesh point in the crystal lattice structure is linked with a specific type of dielectric material (i.e., lead salt substrate or air) and contains information about its basic properties, such as dielectric constant and dispersion parameters.

4.4.1. TE Waves
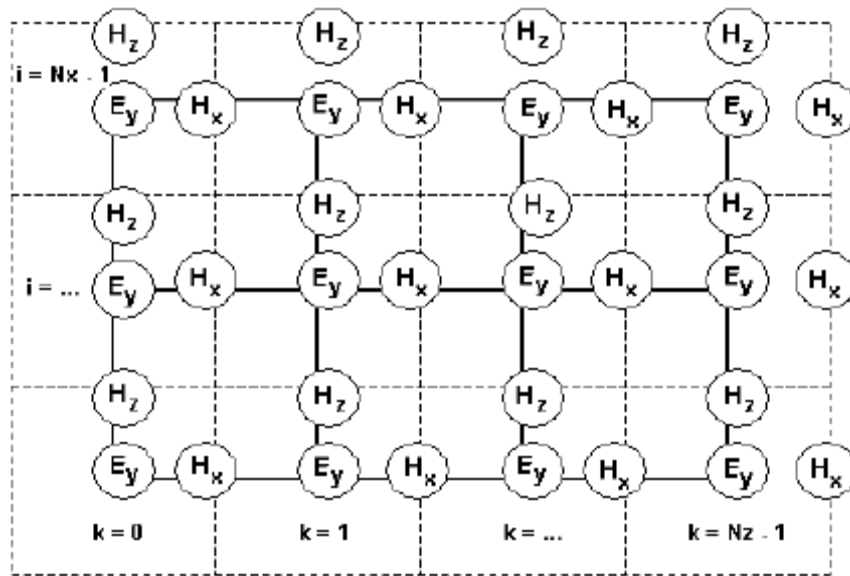
Fig. 4.2: Position of the TE fields in the computational domain.

For the two-dimensional TE case in the X-Z plane, electric and magnetic field components like E_y, H_x and H_z would exist. The electromagnetic equations in lossless media are given as:

$$\frac{\partial E_y}{\partial t} = \frac{1}{\varepsilon}\left(\frac{\partial H_x}{\partial z} - \frac{\partial H_z}{\partial x}\right)$$

$$\frac{\partial H_x}{\partial t} = \frac{1}{\mu_0} \frac{\partial E_y}{\partial z}$$

$$\frac{\partial H_z}{\partial t} = -\frac{1}{\mu_0} \frac{\partial E_y}{\partial x} \tag{4.1}$$

where $\varepsilon = \varepsilon_0 \varepsilon_r$ is the dielectric permittivity of the crystal lattice medium and μ_0 is the vacuum magnetic permeability. ε_0 and ε_r are the vacuum permittivity and the relative permittivity of the crystal medium, respectively. The refractive index of the medium is given by $n = \sqrt{\varepsilon_r}$.

Each component of the electromagnetic field inside the crystal lattice structure is represented by a two-dimensional (2D) array - $E_y(i,k)$, $H_x(i,k)$ and $H_z(i,k)$ - equivalent to the 2D mesh grid demonstrated in Fig. 4.1. The indices i and k designate step size in space along the X- and Z- directions, respectively. Fig. 4.2 illustrates the distribution of the TE field components in the mesh structure in account. The distribution model of the TE field pattern is explained as follows. The E_y field, as shown in Fig. 4.2, coincides in space with the mesh node location in Fig. 4.1. The solid lines in Fig. 4.2 symbolize the mesh in Fig. 4.1. The E_y field is designated to be the center of the FDTD cell in space. Each FDTD shell is indicated by dashed lines in Fig. 4.2. The magnetic field components, H_x and H_z, form the cell edges. The positions of the E_y field is associated with the integer values of indices i and k. The locations of the H_x field is associated with integer values of i and (k + 0.5) indices. Similarly, the H_z field is associated with integer (i + 0.5) and k indices. Implementing numerical discrimination of

the field components and applying them in the first derivative of equation (4.1), results in the following relation:

$$\frac{E_y^n(i,k) - E_y^{n-1}(i,k)}{\Delta t} = \frac{1}{\varepsilon \Delta z}\left[H_x^{n-\frac{1}{2}}\left(i,k+\frac{1}{2}\right) - H_x^{n-\frac{1}{2}}\left(i,k-\frac{1}{2}\right)\right]$$

$$- \frac{1}{\varepsilon \Delta x}\left[H_z^{n-\frac{1}{2}}\left(i+\frac{1}{2},k\right) - H_z^{n-\frac{1}{2}}\left(i-\frac{1}{2},k\right)\right] \tag{4.2}$$

The total set of numerical equations (4.1) takes the following form in the Cartesian co-ordinate system:

$$E_y^n(i,k) = E_y^{n-1}(i,k) + \frac{\Delta t}{\varepsilon \Delta z}\left[H_x^{n-\frac{1}{2}}\left(i,k+\frac{1}{2}\right) - H_x^{n-\frac{1}{2}}\left(i,k-\frac{1}{2}\right)\right]$$

$$- \frac{\Delta t}{\varepsilon \Delta x}\left[H_z^{n-\frac{1}{2}}\left(i+\frac{1}{2},k\right) - H_z^{n-\frac{1}{2}}\left(i-\frac{1}{2},k\right)\right]$$

$$H_x^{n+\frac{1}{2}}\left(i,k+\frac{1}{2}\right) = H_x^{n-\frac{1}{2}}\left(i,k+\frac{1}{2}\right) + \frac{\Delta t}{\mu_0 \Delta z}\left[E_y^n(i,k+1) - E_y^n(i,k)\right]$$

$$H_z^{n+\frac{1}{2}}\left(i+\frac{1}{2},k\right) = H_x^{n-\frac{1}{2}}\left(i+\frac{1}{2},k\right) - \frac{\Delta t}{\mu_0 \Delta x}\left[E_y^n(i+1,k) - E_y^n(i,k)\right] \tag{4.3}$$

The scheme is actually based on implementing Yee's[17] numerical approach to establish central difference approximations for both temporal and spatial derivatives. The superscript n denotes the time steps used in the numerical algorithm. The space sampling for the calculation is done on a sub-micron scale. To ensure numerical stability of the mathematical calculation in the absorbing medium, the Courant-Friedrichs-Levy (CFL) condition[18] was utilized as follows:

$$\Delta t \leq 1 \bigg/ \left(c \sqrt{1/(\Delta x)^2 + 1/(\Delta z)^2} \right) \tag{4.4}$$

4.4.2. TM Waves
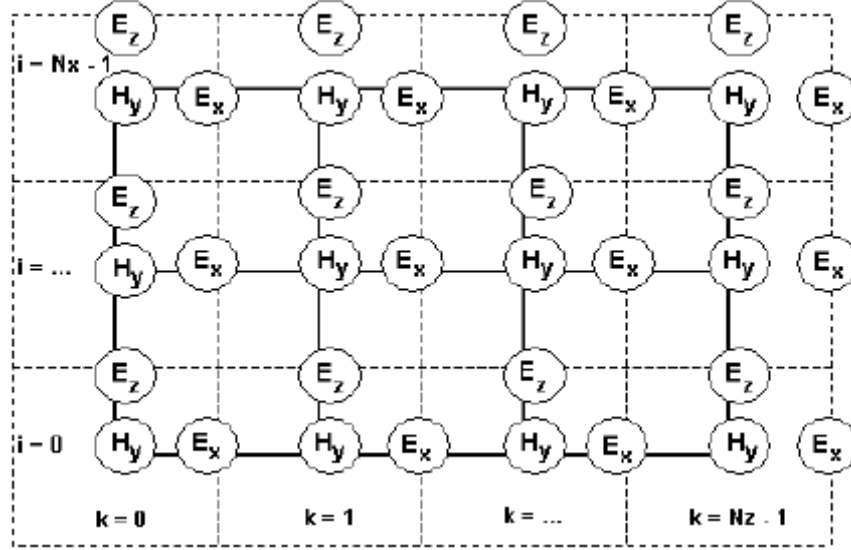
Fig. 4.3: Position of the TM fields in the computational domain.

Similarly, for the 2D TM case in the X-Z plane, electric and magnetic field components like E_x, H_y and E_z would exist. The Helmholtz's equations in lossless media are given as:

$$\frac{\partial H_y}{\partial t} = -\frac{1}{\mu_0} \left(\frac{\partial E_x}{\partial z} - \frac{\partial E_z}{\partial x} \right)$$

$$\frac{\partial E_x}{\partial t} = -\frac{1}{\varepsilon} \frac{\partial H_y}{\partial z}$$

$$\frac{\partial E_z}{\partial t} = \frac{1}{\varepsilon} \frac{\partial H_y}{\partial x} \tag{4.5}$$

108

The distribution of the TM field components in the computational domain is shown in Fig. 4.3. In this case, the electric field components E_x and E_z form the FDTD cell edges. The magnetic field component H_y is associated with the center of the FDTD cell. The numerical equations in the TM algorithm can be demonstrated in a similar way to equation (4.3).

4.5.   Plane Wave Expansion (PWE) Method

The band structure of the lead salt PBG lattice for both TE and TM modes are plotted with the help of very popular PWE method. By this methodology, the Maxwell's equation in a transparent, time invariant, source-less, and non-magnetic medium can be described as:

$$\nabla \times \frac{1}{\varepsilon(\vec{r})} \nabla \times \vec{H}(\vec{r}) = \frac{\omega^2}{c^2} \vec{H}(\vec{r}) \qquad (4.6)$$

where $\varepsilon(\vec{r})$ is the dielectric permittivity which is a function of space. c is the speed of light in vacuum, and $\vec{H}(\vec{r})$ is the optical magnetic field vector having a definite angular frequency ω. The time dependence of $\vec{H}(\vec{r})$ is designated by a term $e^{i\omega t}$. Equation (4.6) is known as the "master" equation[19]. This equation represents a Hermitian eigen value problem.

According to the Bloch theorem, the magnetic field can be represented in a medium with infinite periodicity as:

$$\vec{H}(\vec{r}) = e^{i k \vec{r}} \vec{h}_k(\vec{r}) \qquad (4.7)$$

where $\vec{h}(\vec{r}) = \vec{h}(\vec{r} + \vec{R})$ for all possible arrangements of crystal lattice vectors $\vec{R}$. Thus, combining equations (4.6) and (4.7), one can obtain:

$$\left(\nabla + i\vec{k}\right) \times \left[\frac{1}{\varepsilon_{\vec{r}}}\left(\nabla + i\vec{k}\right)\right] \times \vec{h}_k = \frac{\omega^2}{c^2}\vec{h}_k \tag{4.8}$$

Equation (4.8) is the fundamental equation which one can solve to get the dispersion relation inside a particular crystal lattice structure. This equation is generally transformed into a finite domain by simply expanding the magnetic field in a finite basis of simple plane waves. Several methodologies[20] [21] have already been adopted in solving the final discretized problem. The final solution of the discretized problem would result in a dispersion relation between modal frequencies and wave vector $\vec{k}$, generally plotted in the form of a band diagram.

4.6.   Finite Difference Method (FDM)

There are a number of numerical approaches available for the electromagnetic analysis of structures having complicated geometries and designs. Numerical schemes, such as finite element, finite difference, and boundary element methods, are well known and well established. However, most of these popular mathematical and analytical tools involve complex algebra and therefore, in order to find a numerical solution, they all prove to be time killer. Therefore, a fast and precise method for the modal analysis of a complicated structure, such as the PBG crystal lattice, has been implemented in this study.

The method fundamentally incorporates the finite difference (FD) scheme. It is based on the perturbation correction technique[22] [23], devised with a field convergence algorithm. This method removes the limitation of the FDTD scheme in obtaining individual modal field distributions. This limitation of FDTD arises because the source used in the method is an impulse function in the time domain covering an infinite spectrum, thus field solutions are a superposition of all possible modes. But FDM, through a small correction in field and mode index evaluates individual mode field solutions in the crystal lattice structure.

The concerned lead salt PBG structure is constructed with the usual discretization notation and index profile, $n^2(x, y) = n_{ij}^2$ where n_{ij} corresponds to the index profile along the cross-section of the lattice. Since the field at the boundaries must vanish, assuming an initial value of the field, e next to one boundary, approximate field distribution and mode index are calculated. After this primary calculation, taking these values as the initial conditions, the verification of the discretized Helmoltz's equation at all grid points by the basic mode convergence equation is carried out. The field value is represented by $e_{i,j}$ and can be given as:

$$e_{i,j} = \frac{e_{i,j+1} + e_{i,j-1} + e_{i+1,j} + e_{i-1,j}}{4 - (\Delta x)^2 k_0^2 \left(n_{i,j}^2 - n_{eff}^2 \right)} \tag{4.9}$$

In equation (4.9), k_0 is free space wave vector, $n_{i,j}$ is the refractive index at the computational point and n_{eff} is the effective refractive index of the semiconductor material. In this case, we assume $\Delta x = \Delta y$. Through a series of convergence scans, the

resulting field distribution yields a more accurate value of mode index[24], n_{effm} through the

equation

$$n_{effm}^2 = \frac{\int_{-\infty}^{+\infty}\int_{-\infty}^{+\infty} \left[\begin{array}{c} e_{i+1,j} + e_{i-1,j} + \dfrac{2\varepsilon_{i,j-1}}{\varepsilon_{i,j-1}+\varepsilon_{i,j}} e_{i,j-1} + \dfrac{2\varepsilon_{i,j+1}}{\varepsilon_{i,j+1}+\varepsilon_{i,j}} e_{i,j+1} \\[2mm] -\left\{ 4 + \dfrac{\varepsilon_{i,j}-\varepsilon_{i,j-1}}{\varepsilon_{i,j}+\varepsilon_{i,j-1}} + \dfrac{\varepsilon_{i,j}-\varepsilon_{i,j+1}}{\varepsilon_{i,j}+\varepsilon_{i,j+1}} - k_0^2(\Delta y)^2 \varepsilon_{i,j} \right\} e_{i,j} \end{array} \right] e_{i,j}\, dx\, dy}{k_0^2(\Delta y)^2 \int_{-\infty}^{+\infty}\int_{-\infty}^{+\infty} e_{i,j}^2\, dx\, dy} \qquad (4.10)$$

The aforesaid process of recurring convergence scan and consequent assessment

of the mode effective index is continued until a desired precision in the value of n_{effm} is

achieved. For very fast convergence, the algorithm is altered with a relaxation factor by

which the change in the field before and after convergence scans is added in the next step

of convergence. The method described above results in the scalar fields of the waveguide

modes. In order to get the solution for the polarized modes, the approximate modes can

be calculated through the TE and TM modal solution of the constituent slab waveguides.

For mode field correction, the FD discretization can simply be adapted by incorporating

the semivectorial Helmoltz's equation. In the case of the TE modes, the continuity

condition leaves the scalar Helmoltz's equation unchanged to represent the semi-vectorial

form. For the TM modes, the corresponding equation[25] is given as:

$$\left(\frac{\partial^2}{\partial y^2} + k_0^2 n^2 - \beta^2 \right) E_y + \frac{\partial}{\partial y}\left(E_y \frac{\partial}{\partial y} \log n^2 \right) = 0 \qquad (4.11)$$

Considering a three-point centered difference approximation for the operator

$\partial^2/\partial y^2$ and implementing a uniform sampling grid, the field in case of semi-vectorial

form, is converged to an *x*-polarized mode as given by the following convergence scan equation.

$$e_{i,j} = \frac{e_{i+1,j} + e_{i-1,j} + \dfrac{2\varepsilon_{i,j-1}}{\varepsilon_{i,j-1} + \varepsilon_{i,j}} e_{i,j-1} + \dfrac{2\varepsilon_{i,j+1}}{\varepsilon_{i,j+1} + \varepsilon_{i,j}} e_{i,j+1}}{4 - k_0^2 (\Delta y)^2 \left(\varepsilon_{i,j} - n_{eff}^2\right) + \dfrac{\varepsilon_{i,j} - \varepsilon_{i,j-1}}{\varepsilon_{i,j} + \varepsilon_{i,j-1}} + \dfrac{\varepsilon_{i,j} - \varepsilon_{i,j+1}}{\varepsilon_{i,j} + \varepsilon_{i,j+1}}} \tag{4.12}$$

From the field distribution, the n_{effm} is then calculated using the integral as in equation (4.13).

$$n_{effm}^2 = \frac{\displaystyle\int_{-\infty}^{+\infty}\int_{-\infty}^{+\infty} \left[\begin{array}{c} e_{i+1,j} + e_{i-1,j} + \dfrac{2\varepsilon_{i,j-1}}{\varepsilon_{i,j-1} + \varepsilon_{i,j}} e_{i,j-1} + \dfrac{2\varepsilon_{i,j+1}}{\varepsilon_{i,j+1} + \varepsilon_{i,j}} e_{i,j+1} \\[2mm] - \left\{ 4 + \dfrac{\varepsilon_{i,j} - \varepsilon_{i,j-1}}{\varepsilon_{i,j} + \varepsilon_{i,j-1}} + \dfrac{\varepsilon_{i,j} - \varepsilon_{i,j+1}}{\varepsilon_{i,j} + \varepsilon_{i,j+1}} - k_0^2 (\Delta y)^2 \varepsilon_{i,j} \right\} e_{i,j} \end{array} \right] e_{i,j}\, dx\, dy}{k_0^2 (\Delta y)^2 \displaystyle\int_{-\infty}^{+\infty}\int_{-\infty}^{+\infty} e_{i,j}^2\, dx\, dy} \tag{4.13}$$

In case of *y*-polarized mode, equations (4.12) and (4.13) are exactly followed with the indices i, j interchanged.

4.7.   Lead Chalcogenide Defect Cavity PBG Structure

The photonic semiconductor structure consists of a PbSe-Pb$_{0.98}$Sr$_{0.02}$Se multiple quantum well structure, grown on a BaF$_2$ substrate, which has arrays of dielectric air columns periodically distributed in hexagonal fashion on the surface (as shown in Fig. 4.4(a)). Fig. 4.4(b) demonstrates the symmetry points of the first Brillouin zone in the periodic hexagonal crystal. The structure has the following constituent material parameters: refractive indices are n_{PbSe} = 5.0 (bulk PbSe), n_{PbSrSe} = 4.6 (Pb$_{0.98}$Sr$_{0.02}$Se) and

$n_a = 1$ (air). The active layer is considered to have a $\lambda/2$ thickness, where λ is the emission wavelength. In order to choose an optimized design along two-dimensional crystal structure, scanning has been done to calculate modal band structure and the corresponding bandgaps in the crystal lattice for varying air-hole radius.
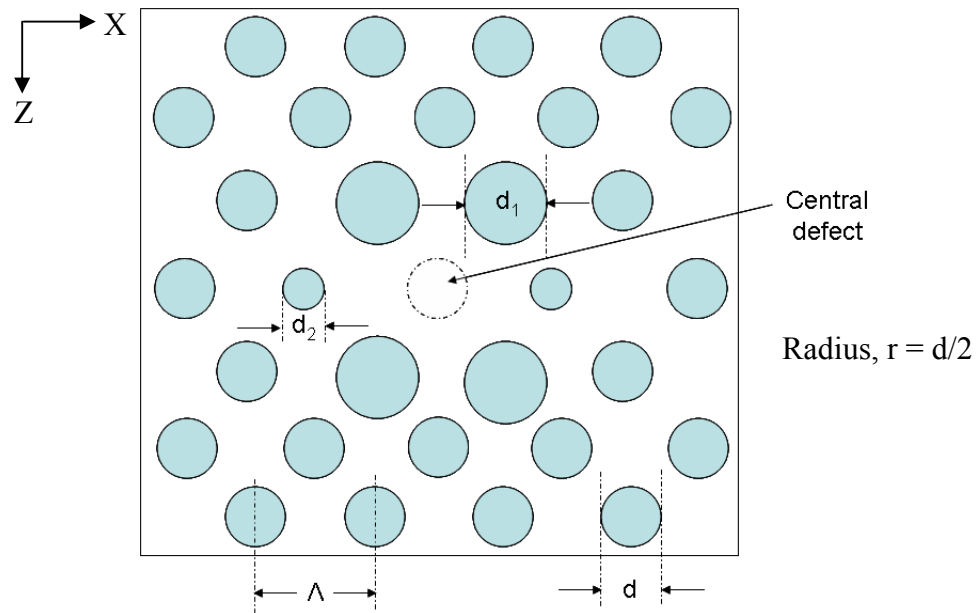
(a)
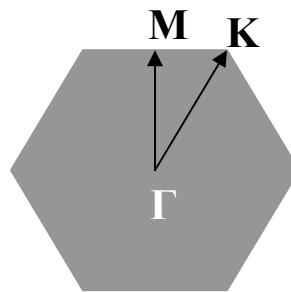
(b)

Fig. 4.4: (a) Top view of triangular photonic crystal lattice structure, (b) Schematic of first Brillouin zone for the hexagonal lattice pattern.
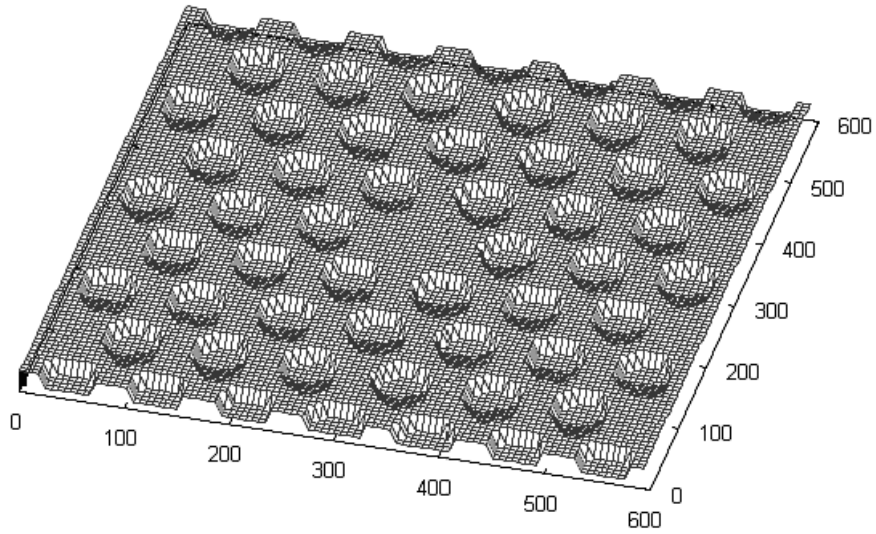
Fig. 4.5: Top View of refractive index variation over the cross-section of hexagonal crystal lattice.

The cross section of the designed hexagonal crystal lattice structure constructed during FDM simulation is illustrated in Fig. 4.5. The diagram illustrates the formation of a single defect inside the PC structure by omitting the central air-hole within a computational window of a 600×600 mesh points.

4.7.1. Mid Infrared Photonic Bandgap Formation

The bandgap structure is illustrated in Fig. 4.6 where all the frequency eigenvalues from the dispersion curves are combined along the single vertical line for each specific scanned value of radius. The crystal is optimally designed to have a

dielectric air-hole diameter (d) of 0.63 µm with a periodic lattice constant (∧) of 0.96 µm. The air-fraction (d/∧) in the photonic crystal plays an important role in creating the bandgap.

(a)

(b)
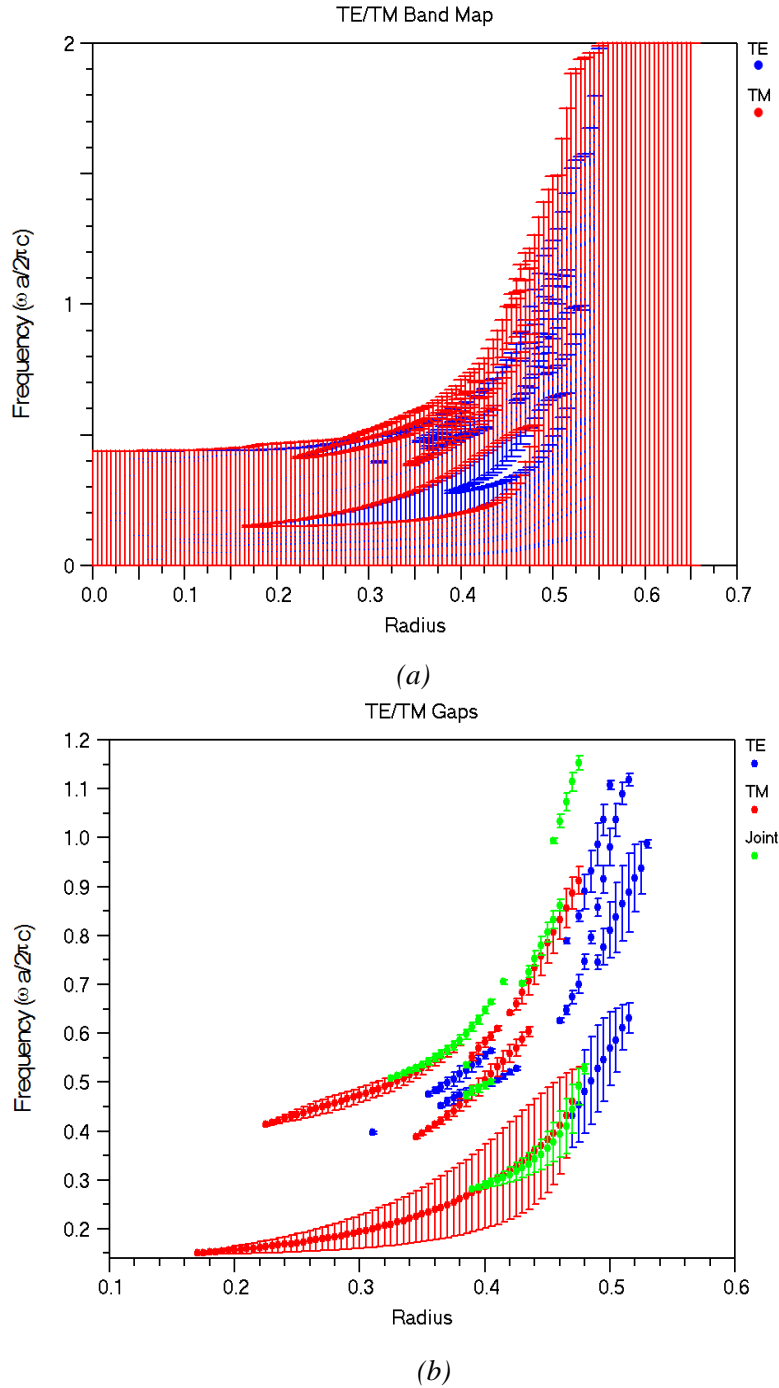
Fig. 4.6: (a) Reduced band map for TE and TM mode, (b) band map for TE, TM, and joint mode.

The band frequency tends to rise with the increase of air-fraction for a fixed lattice constant ($\wedge$) in the crystal, as can be seen in Fig. 4.6(a).

In Fig. 4.7, both transverse electric (TE) and transverse magnetic (TM) band structures are plotted with the help of the PWE method. However, it is mention-worthy that the resonating optical modes in such a periodically patterned crystal are not distinctively TE or TM but they can be thought as TE-like and TM-like[26]. The band diagrams in Fig. 4.7(b) demonstrate one narrow and another quite broad TM-like photonic bandgap exist in the structure, but no TE-like bandgaps. The bandgap values are populated in Table-4.1. Moreover, the broad TM bandgap covers the mid-infrared spectral region where room temperature photoluminescence from lead salts takes place. Therefore the focus is to engineer a defect cavity mode in this frequency bandgap region.

(a)

117

TM Band Structure

(b)
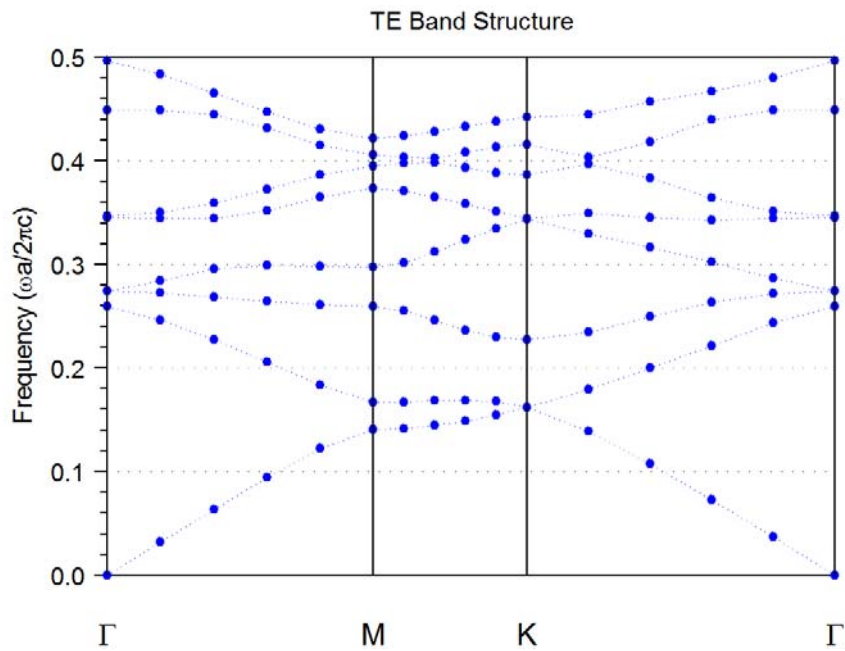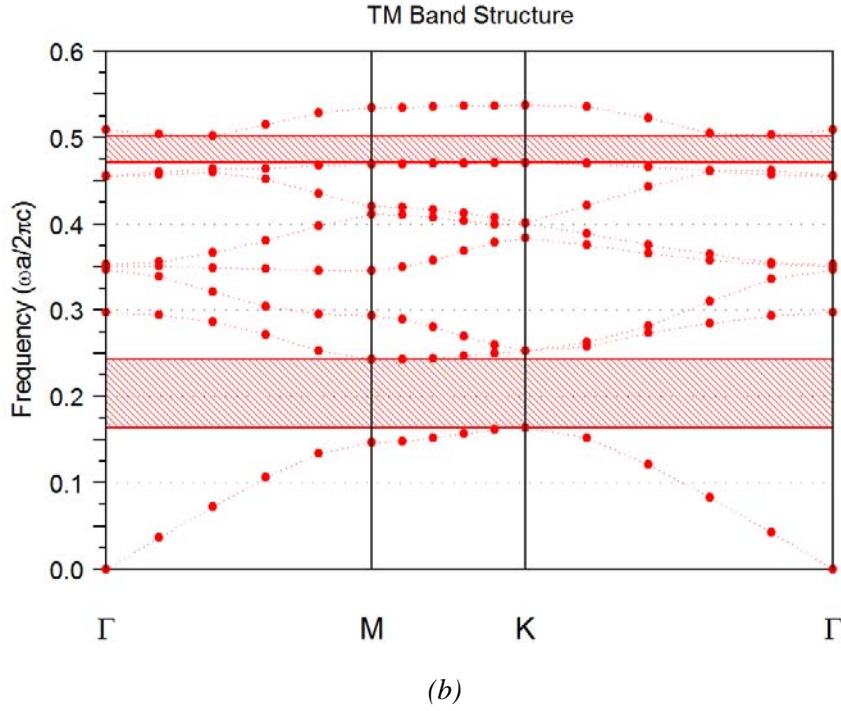
Fig. 4.7: Band structure of the photonic crystal for (a) TE and (b) TM polarized light.

Table-4.1: TM bandgaps in the hexagonal periodic photonic lattice structure on IV-VI lead salt semiconductor.

Serial Number	Bandgap
TM1	1.916 μm – 2.038 μm
TM2	3.959 μm – 5.872 μm

The defect cavity is designed (as illustrated in Fig. 4.4(a)) by omitting the central air column, four vertical (two on top and two at bottom) lattice atoms along the X-direction surrounding the central defect are made to have a diameter of 0.8 μm, two

adjacent horizontal atoms along the Z-direction surrounding the central defect are made to have a diameter of 0.46 μm.

4.7.2. Modal Analysis by FDM Scheme

To appreciate the confinement of modes to the central region, mode field distributions are calculated using the FDM technique. Different values of emission wavelength and crystal lattice parameters have been selected to optimize the variation in mode field distribution on changing these parameters. The final goal is to achieve a single modal laser emission from the lead chalcogenide defect cavity PC structure. It is noticed that the field distribution appears to be largely Gaussian for the single modal condition. However, when the emission wavelength becomes multi-modal, the field assumes a distribution different from the usual Gaussian shape. This can be seen in Fig. 4.8, which depicts the distribution of electric field for the fundamental and multi mode at emission wavelengths of 4.17 μm[27].

(a)

119

(b)
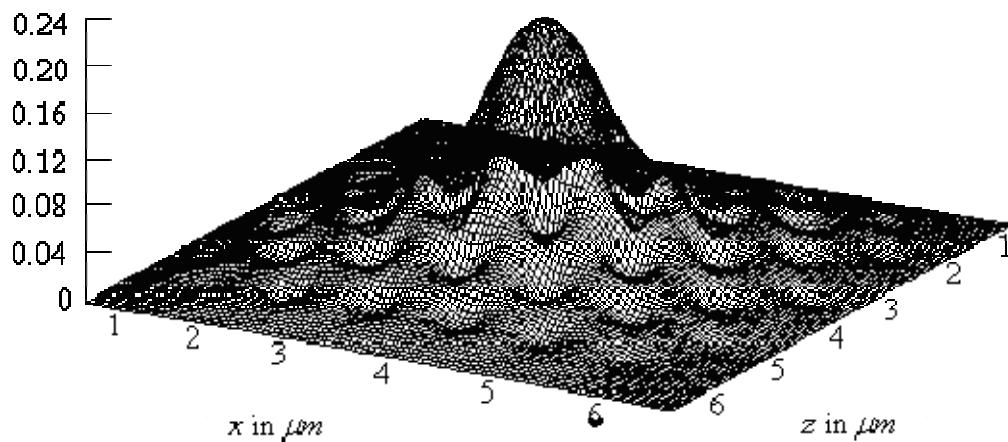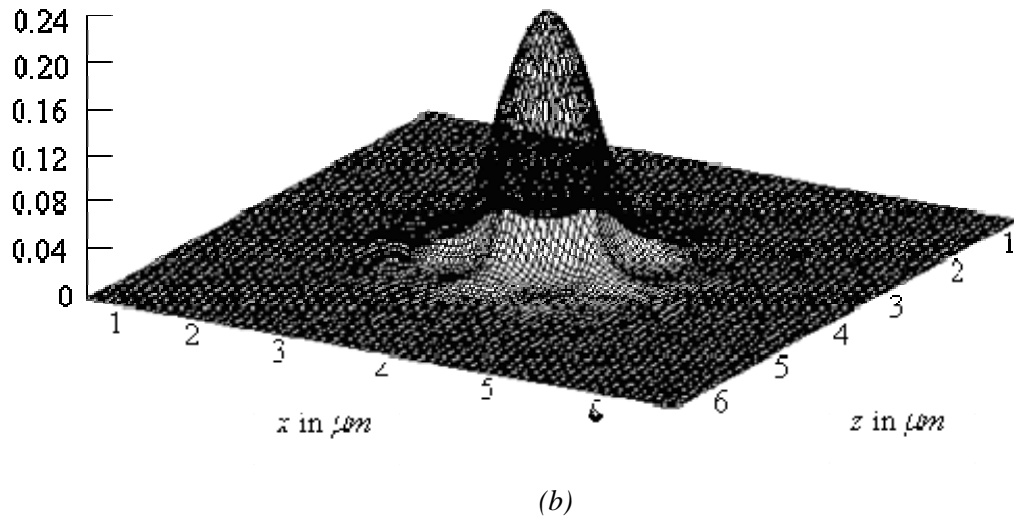
Fig. 4.8: Resonating electric field distribution at λ = 4.17 μm (a) when multi-modal, (b) when single modal.

The effective modal refractive index at the resonating condition is formulated to be ~ 4.04. FDM perturbation technique determines the field distribution in the crystal at a fixed wavelength and, therefore, it is quite challenging while determining the resonating wavelength for a specific optical cavity. This necessitates the deployment of an FDTD approach which produces a wideband response for the field distribution in the cavity by exciting the crystal with a Gaussian pulse. Moreover, by applying the FDTD approach, the results of the FDM approach could be verified.

4.7.3. Modal Analysis by FDTD Scheme

The uniaxial perfectly matched layer (UPML) absorbing boundary condition[28] [29] [30], which is a very efficient method in dealing with scattering by particles in vacuum, is implemented as the boundary layers outside the FDTD computational window. In order

to excite the photonic crystal structure, a Gaussian modulated continuous wave (GMCW) point source is considered, which can be expressed as:

$$E_{inc} = A. \exp\left[-0.5.(t - t_0)^2 / T^2\right] \sin(\omega t) \qquad (4.14)$$

where A is the input wave amplitude, T is the half width, ω is the angular frequency, t_0 is the time offset. The rigorous numerical analysis produces precise and efficient time domain response for the field distribution in the defect cavity.
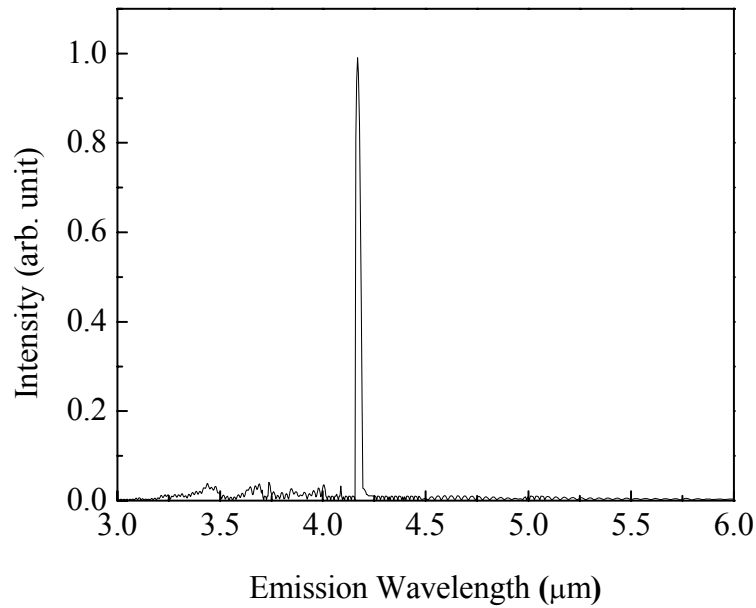
Fig. 4.9: Spectral response from DFT calculations after FDTD analysis of the resonating defect cavity.

To generate the spectral response corresponding to the time domain behavior, a discrete Fourier transform (DFT) is applied. This calculates spectral response for a specific wavelength, as shown by:

$$F(\omega) = \int_0^T F(t).\exp(-j\omega t)dt = \sum_{n=0}^{N} F(n).\exp(-j\omega n\Delta t).\Delta t \qquad (4.15)$$

where F(n) is the time domain response, N is the number of time steps. The spectral field obtained from the defect cavity (as in Fig. 4.4(a)) in the photonic crystal is seen to resonate at 4.17 μm and is plotted in Fig. 4.9. The result seems to be in exact correlation with the numerical results obtained from the FD perturbation correction analysis. The optimized quality factor for the resonating mode is calculated to be 5200.

4.8.   Experimental Steps for Air Hole Formation
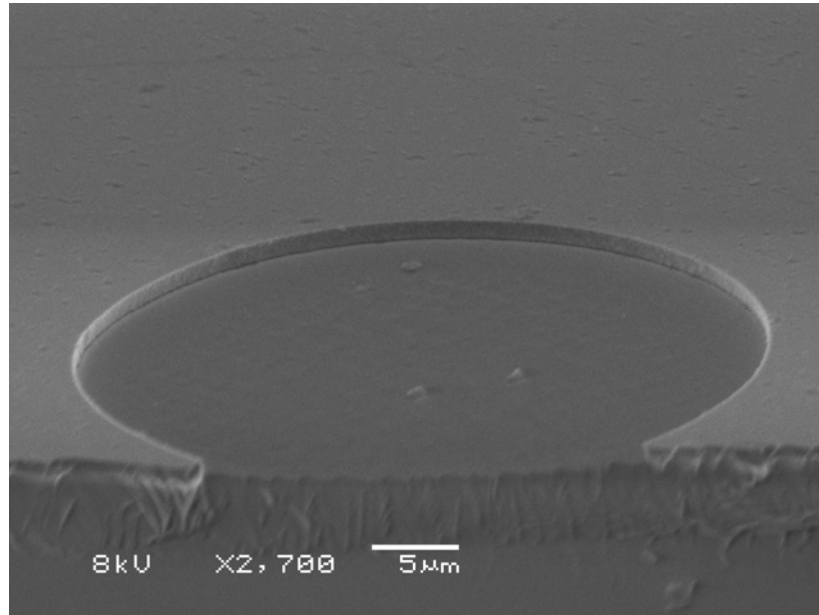
Fig. 4.10: Realization of air-hole by photolithography and wet etching method.

In order to realize a PC lasing cavity in the opto-electronics lab at OU, one has to employ contact lithography and the wet etching method. One of the most important

122

parameters of PC air-hole is the inclination of its side wall with the base substrate. During the theoretical simulation, it is always considered that the side wall is perfect in terms of the surface roughness and inclination. Even a minute alteration in these parameters affects the modal behavior of the defect cavity emission inside the crystal lattice structure. The surface roughness is not a problem for the wet etching method. The only challenge is the vertical inclination. In order to verify the initial presumption, a photo-mask was selected which would lead to an air-hole with a diameter of 50 μm, as shown in Fig. 4.10. It is to be noted that the dimension of this mask has nothing to do with the original theoretical PC laser dimension. A bigger air-hole mask was considered just to study the perfection of wet etching procedure.
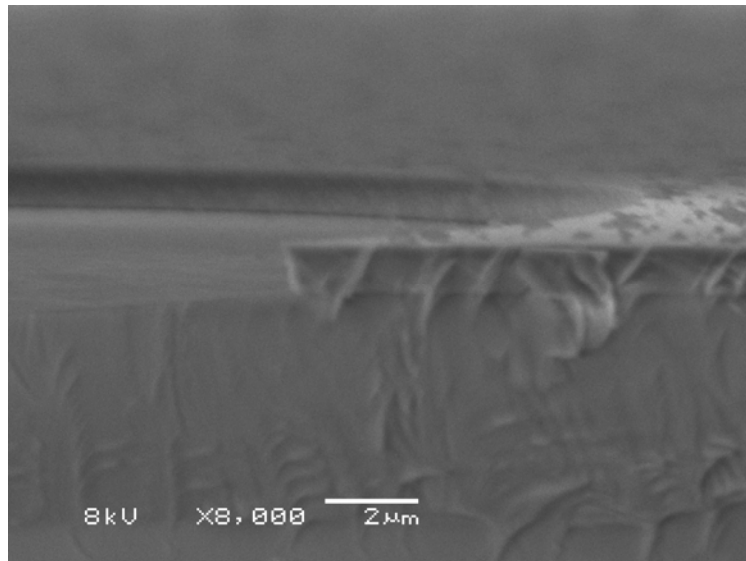
Fig. 4.11: Air-hole side wall inclination to base not exactly vertical after wet etching method.

The air-hole is etched on a PbSe single layer grown on a (111) BaF$_2$ substrate. From Fig. 4.11, it can be seen that the air-hole is not perfectly vertical to the base

substrate. Rather, it poses an acute angle with the base. Therefore, the wet etching method is proved to be unsuitable for PC laser structure fabrication. Thus, dry etching or plasma etching seems to be the only feasible option remaining to fabricate a PC lasing cavity on a lead salt substrate. A joint collaborative study with Penn State University is currently underway and the preliminary result of their dry etching procedure on OU MBE-grown lead salt material is illustrated in Fig. 4.12.
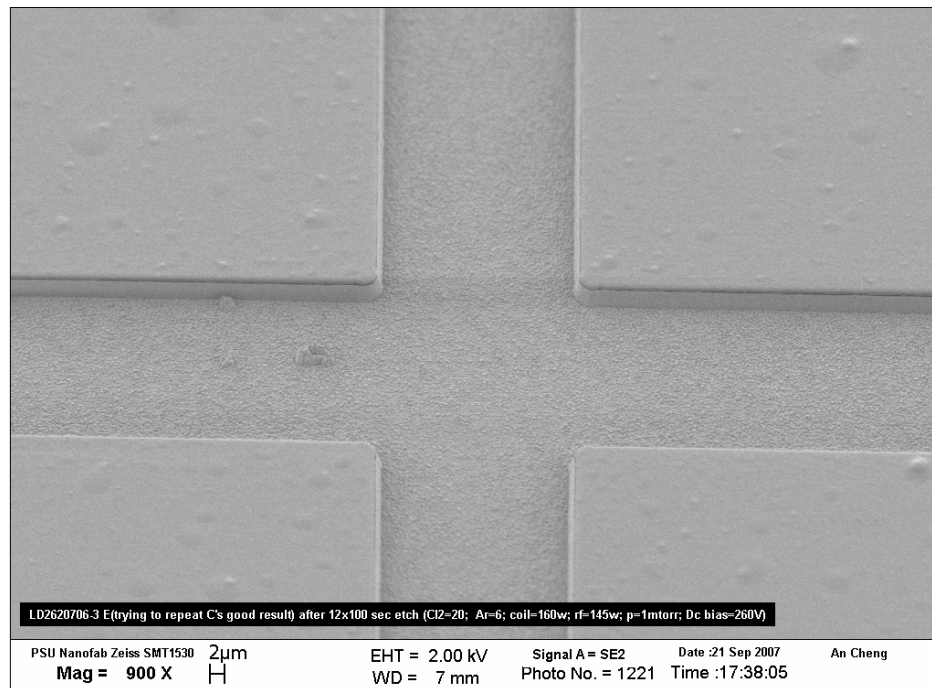
Fig. 4.12: Plasma etching of lead salt material (Courtesy: Penn State University).

4.9. Conclusions

In conclusion, a theoretical investigation of spontaneous mid-infrared emission from IV-VI semiconductor defect cavity in the hexagonal photonic crystal is elaborated in this chapter. The design is aimed to solve out challenges of the formation of resonating

cavity for lead salt materials fabricated on Si(111) or BaF$_2$(111) substrates. The band structure calculations of the periodic crystal are performed using the PWE method. Two approaches have been implemented to analyze and understand modal field distribution in the defect cavity. The FD perturbation correction method and FDTD algorithms are very popular and well-established mathematical tools for optical waveguide analysis. It has been demonstrated that the FDTD results reasonably agree with those obtained using the FD perturbation method. A single TM-like mode working at 4.17 μm, having an optimized Q-factor of 5200, resonates in the designed defect cavity. The prospective practical applications of the single mid-infrared emission are mainly in industrial trace-gas sensing systems and emission monitoring.

4.10. References

[1] Z. Shi, G. Xu, P. J. McCann, X. M. Fang, N. Dai, C. L. Felix, W. W. Bewley, I. Vurgaftman, and J. R. Meyer, "IV–VI compound midinfrared high-reflectivity mirrors and vertical-cavity surface-emitting lasers grown by molecular-beam epitaxy," *Appl. Phys. Lett.*, vol. 76, pp. 3688-3690, 2000.

[2] C. L. Felix, W. W. Bewley, I. Vurgaftman, J. R. Lindle, J. R. Meyer, H. Z. Wu, G. Xu, S. Khosravani, and Z. Shi, "Low-threshold optically pumped λ = 4.4 µm vertical-cavity surface-emitting laser with a PbSe quantum-well active region," *Appl. Phys. Lett.*, vol. 78, pp. 3770-3772, 2001.

[3] F. Zhao, H. Wu, L. Jayasinghe, and Z. Shi, "Above-room-temperature optically pumped 4.12 µm midinfrared vertical-cavity surface-emitting lasers," *Appl. Phys. Lett.*, vol. 80, pp. 1129-1131, 2002.

[4] H. Xu, F. Zhao, A. Majumda, L. Jayasinghe, and Z. Shi, ""High power midinfrared optically pumped PbSe–PbSrSe multiple-quantum-well vertical-cavity surface-emitting laser operation at 325 K," *Electron. Lett.*, vol. 39, pp. 659-661, 2003.

[5] J. D. Joannopoulos, R. D. Meade, and J. N. Winn, "Photonic Crystals, Modeling the Flow of Light," *Princeton University Press*, Princeton, N.J., 1995.

[6] J. D. Joannopoulos, P. R. Villeneuve, S. Fan, "Photonic crystals: putting a new twist on light," *Nat.*, vol. 386, pp. 143-149, 1997.

[7] T. Krauss, Y. P. Song, S. Thoms, C. D. W. Wilkinson, and R. M. DelaRue, "Fabrication of 2-D photonic bandgap structures in GaAs/AlGaAs," *Electron. Lett.*, vol. 30, pp. 1444-1446, 1994.

[8] T. F. Krauss, R. M. D. L. Rue, and S. Brand, "Two-dimensional photonic-bandgap structures operating at near-infrared wavelengths," *Nat.*, vol. 383, pp. 699-702, 1996.

[9] J. O'Brien, O. Painter, C. C. Cheng, R. Lee, A. Scherer, and A. Yariv, "Lasers incorporating 2D photonic bandgap mirrors," *Electron. Lett.*, vol. 32, pp. 2243-2244, 1996.

[10] T. Baba and T. Matsuzaki, "Fabrication and photoluminescence of GaInAsP/InP 2D photonic crystals," *Jpn. J. Appl. Phys.*, vol. 35, pp. 1348-1352, 1996.

[11] T. Hamano, H. Hirayama, and Y. Aoyyagi, "Optical characterization of GaAs 2D photonic bandgap crystal fabricated by selective MOVPE," in *Conference on Lasers and Electro-Optics*, vol. 11 of 1997 OSA Technical Digest Series (Optical Society of America, Washington, D.C.), pp. 528-529, 1997.

[12] E. Yablonovitch, "Inhibited spontaneous emission in solid state physics and electronics," *Phys. Rev. Lett.*, vol. 58, pp. 2059-2062, 1987.

[13] M. M. Sigalas, R. Biswas, Q. Li, D. Crouch, W. Leung, R. Jacobs-Woodbury, B. Laogh, S. Nielsen, S. McCalmont, G. Tuttle, K. M. Ho, "Dipole antennas on photonic band -gap crystals– experiment and simulation," *Microwave Opt. Tech. Lett.*, vol. 15, pp. 153-158, 1997.

[14] G. P. Gauthier, A. Courtay, and G. M. Rebeiz, "Microstrip antennas on synthesized low dielectric-constant substrates," *IEEE Trans. Antennas Propag.*, vol. 45, pp. 1310-1314, 1997.

[15] J. G. Maloney, M. P. Kesler, B. L. Shirley, and G. S. Smith, "A simple description for waveguiding in photonic bandgap materials," *Microwave Opt. Tech. Lett.*, vol. 14, pp. 261-265, 1997.

[16] Opti-FDTD user manual, Optiwave.

[17] K. S. Yee, "Numerical solution of initial boundary value problems involving maxwell's equations in isotropic media," *IEEE Trans. Antennas. Prop.*, vol. AP-14, pp. 302-307, 1966.

[18] A. Taflove and M. E. Brodwin, "Numerical solution of steady-state electromagnetic scattering problems using the time-dependent Maxwell's equations," *IEEE Trans. Microwave Theory Tech.*, vol. MTT-23, pp. 623-630, 1975.

[19] J. D. Joannopoulos, R. D. Meade, and J. N. Winn, "Photonic crystals, Molding the flow of light," *Princeton University Press*, 1995.

[20] S. G. Johnson, J. D. Joannopoulos, "Block-iterative frequency-domain methods for Maxwell's equations in a planewave basis," *Opt. Exp.*, vol. 8, pp.173-190, 2000.

[21] S. Guo, S. Albin, "Simple plane wave implementation for photonic crystal calculations," *Opt. Exp.*, vol. 11, pp.167-175, 2003.

[22] P. R. Chaudhuri, V. Paulose, C. Zhao, C. Lu, "Near-elliptic core polarization-maintaining photonic crystal fiber: modeling birefringence characteristics and realization," *IEEE Photon. Technol. Lett.*, vol. 16, pp. 1301-1303, 2004.

[23] P. R. Chaudhuri, A. K. Ghatak, B. P. Pal, C. Lu, "Fast convergence and higher-order mode calculation of optical waveguides: perturbation method with finite difference algorithm," *Opt. Las. Technol.*, vol. 37, pp. 61-67, 2005.

[24] A. W. Snyder, J. D. Love, "Optical waveguide theory," London:Chapman & Hall, pp. 487-513, 1983.

[25] K. Kawano, T. Kitoh, "Introduction to optical waveguide analysis," Chapter 4, New York:Wiley, 2001.

[26] O. Painter, J. Vuckovic, and A. Scherer, "Defect modes of a two-dimensional photonic crystal in an optically thin dielectric slab," *J. Opt. Soc. Am. B*, vol. 16, pp. 275-285, 1999.

[27] Shaibal Mukherjee, Gang Bi, Jyoti P. Kar, and Zhisheng Shi, "Two dimensional numerical analysis on mid-infrared emission from IV-VI lead salt photonic crystal microcavity," in Press, *Optica Applicata*, 2009.

[28] J. P. Berenger, "A perfectly matched layer for the absorption of electromagnetic waves," *J. Comput. Phys.*, vol. 114, pp. 185-200, 1994.

[29] D. S. Katz, E. T. Thiele, and A. Taflove, "Validation and extension to three dimensions of the Berenger PML absorbing boundary condition for FD-TD meshes," *IEEE Microwave Guid. Wave Lett.*, vol. 4, pp. 268-270, 1994.

[30] J. P. Berenger, "Three-dimensional perfectly matched layer for the absorption of electromagnetic waves," *J. Comput. Phys.*, vol. 127, pp. 363-379, 1996.

CHAPTER 5

MINORITY CARRIER LIFETIME MEASUREMENT

5.1. Background

The theory of recombination of an electron-hole pair through the formation of recombination centers (also known as "traps") was introduced in early 1950 by Hall[1] and Shockley and Read[2]. In 1960, a few years later, Hall detailed his original inventions.[3] In modern semiconductor and integrated circuit (IC) industries, lifetimes and diffusion lengths of carriers are routinely measured. Carrier lifetime is one of the important parameters providing characteristic information about semiconductor defect densities. In theory, there is no lower limit of bulk defect density estimated by lifetime measurement techniques. Moreover, minority carrier lifetime is considered as one of the essential figures of merit of opto-electronic devices mainly photo detectors.

In a broad sense, carrier lifetime can be classified into two major categories: recombination lifetimes and generation lifetimes.[4] The fundamental concept of recombination lifetime (τ_r) applies when excess carriers decay due to the occurrence of electron and hole recombination. The notion of generation lifetime (τ_g) holds when there is a scarcity of carriers, e.g. the case of space charge region of a reverse biased device and the device attempts to reach an equilibrium. Thus, by definition an electron-hole pair ceases to exist after a time τ_r. On the other hand, a new electron-hole pair is created after an average time τ_g.

When these generation and recombination mechanisms take place in bulk semiconductor, they are characterized by τ_g and τ_r. When they happen at the surface, they are designated by the surface generation velocity (S_g) and the surface recombination velocity (S_r). Bulk as well as surface generation or recombination process takes place simultaneously and therefore it is extremely difficult to separate them. The measured lifetimes are thus always effective lifetimes comprising of both bulk and surface components.

The bulk recombination rate R would symbolize the non-linear variation of the carrier densities from their equilibrium states. Throughout this chapter, we consider a *p*-type lead salt semiconductor material and are mainly concerned with the characteristic behavior of minority electrons. By restricting our numerical calculations to linear, quadratic, and 3rd order terms, R can mathematically be expresses as follows:

$$R = A(n - n_0) + B(pn - p_0 n_0) + C_p(p^2 n - p_0^2 n_0) + C_n(pn^2 - p_0 n_0^2) \tag{5.1}$$

where $n = n_0 + \Delta n$ and $p = p_0 + \Delta p$.

n_0 and p_0 are the equilibrium electron and hole densities respectively. Δn and Δp are excess electron and hole densities accordingly. A, B, C_p, and C_n are arbitrary constants. In case, there is no trapping inside the semiconductor $\Delta p = \Delta n$ and therefore equation (5.1) can be simplified to

$$R = A\Delta n + B(p_0 + \Delta n)\Delta n + C_p(p_0^2 + 2p_0\Delta n + \Delta n^2)\Delta n + C_n(n_0^2 + 2n_0\Delta n + \Delta n^2)\Delta n$$

(5.2)

In equation (5.2) several terms containing n_0 have been disregarded because $n_0 \ll p_0$ in a p-type lead salt material. The recombination lifetime is given as follows:

$$\tau_R = \frac{\Delta n}{R} \tag{5.3}$$

To be more specific, the various recombination mechanisms occurring inside the lead salt semiconductor material[5] are Shockley-Read-Hall (SRH) recombination, radiative recombination, stimulated recombination, and Auger recombination.

5.2.   Shockley-Read-Hall (SRH) Recombination

A deep defect energy level might affect semiconductor recombination lifetime by providing an additional recombination path for carriers (generally non-radiative path), or might misrepresent the lifetime measurement by behaving as a trapping center. The difference between a trap and a recombination center depends on the relative probability of a captured carrier being thermally released or attracting and combining with a free carrier from the opposite band. The rate equations guiding the free carrier concentrations during recombination via a recombination or trapping center are given as

$$\frac{dn}{dt} = G_n - R_p = E_n F N_T - C_n n(1-F)N_T,$$

$$\frac{dp}{dt} = G_p - R_p = E_p(1-F)N_T - C_p pF N_T \tag{5.4}$$

where E_n and E_p are emission rates and C_n and C_p are capture coefficients electron and hole respectively, N_T is the density of recombination centers, F is the fraction of those centers occupied by electrons.

In thermal equilibrium state, thermal emission rates and capture rates of both electrons and holes are related as shown below:

$$E_n F_0 = C_n (1 - F_0) n_0,$$

$$E_p (1 - F_0) = C_p F_0 p_0 \qquad (5.5)$$

where n_0, p_0 and F_0 are the corresponding values of n, p and F at thermodynamic equilibrium condition. At this condition, the following expressions hold true:

$$\frac{(1 - F_0)}{F_0} = \frac{1}{g} \exp\left(\frac{E - E_F}{kT}\right) \qquad (5.6)$$

$$n_0 = N_C \exp\left(-\frac{E_C - E_F}{kT}\right),$$

$$p_0 = N_V \exp\left(-\frac{E_F - E_V}{kT}\right) \qquad (5.7)$$

where g is the degeneracy factor, E_F is the Fermi energy level, k is the Boltzmann constant, T is temperature, N_C and N_V are the effective density of states in the conduction and valence band, E_C and E_V are the conduction band minimum and the valence band maximum, respectively. Thus equation (5.5) can be expressed as:

$$E_n = C_n n_1, \ E_p = C_p p_1 \tag{5.8}$$

$$\text{where, } n_1 = N_C \frac{1}{g} \exp\left(-\frac{E_C - E_T}{kT}\right) \text{ and } p_1 = N_V \frac{1}{g} \exp\left(-\frac{E_T - E_V}{kT}\right) \tag{5.9}$$

When thermodynamic equilibrium energy becomes equal to Fermi energy level, then both n_1 and p_1 symbolize the density of electrons in the conduction band and holes in the valence band, respectively. Considering steady-state conditions under which $\frac{dn}{dt} = \frac{dp}{dt} = 0$, then according to equation (5.4) it can be stated that the rates of effective recombination of electrons and holes are equal. Mathematically this can be written as:

$$R = R_n - G_n = R_p - G_p \tag{5.10}$$

Following above equation, the fraction of occupied recombination centers or traps under steady-state conditions can be expressed in terms of the densities of electrons and holes as shown below:

$$F = \frac{n_1 C_n + p_1 C_p}{C_n(n + n_1) + C_p(p + p_1)} \tag{5.11}$$

Considering that the density of traps or recombination centers smaller compared to n_0, p_0, n_1 or p_1 and the carrier neutrality is conserved ($\Delta n = \Delta p$), the effective recombination rate of is written as[6]:

$$R = \frac{C_n C_p N_T \left(np - n_i^2\right)}{C_n \left(n + n_1\right) + C_p \left(p + p_1\right)} \tag{5.12}$$

where n_i is the intrinsic carrier concentration. The lifetimes of electron and hole are given by the following equation:

$$\tau_{n0} = \frac{1}{C_n N_T} \;,\; \tau_{p0} = \frac{1}{C_p N_T} \tag{5.13}$$

From equations (5.12) and (5.13), the lifetime in SRH model can be represented as[7]:

$$\tau_{SRH} = \tau_{p0} \frac{n_0 + n_1 + \Delta n}{p_0 + n_0 + \Delta n} + \tau_{n0} \frac{p_0 + p_1 + \Delta p}{p_0 + n_0 + \Delta p} \tag{5.14}$$

The SRH statistics are modified by the possible presence of bound excitons at the recombination centers. In the case, where three different states co-exist at the recombination center i.e., the empty one, occupied one and bound excited one, the effective recombination of an electron-hole pair is represented as:

$$R = \frac{C_n C_p N_T \left(np - n_i^2\right)}{C_n \left(n + n_1\right) + C_p \left(p + p_1\right) + \tau_x C_n \left\{C_p np + \rho \left(n + n_1\right)\right\}} \tag{5.15}$$

In the above equation, τ_x is the lifetime of excitons localized at the recombination or defect centers. The hole capture coefficient Cp, which is pursued by the exciton creation, and the probability ρ of thermal emission of holes from the bound exciton state at the recombination center into the valence band are interrelated by $\rho = C_p N_V \exp\left(-\frac{E_x}{kT}\right)$, where E_x is the binding energy of the bound exciton. Typical values of the lifetime for

lead salt materials lie in the range from 50 ns to microseconds depending on the sample temperature.[8]

5.3. Auger Recombination

Auger recombination is a non-radiative recombination mechanism which is particularly important at excitation densities of free charge carriers in a semiconductor material. There are two distinct classifications of the Auger recombination: the direct recombination and the indirect recombination alias the impurity Auger recombination[6]. During the direct Auger recombination process, the recombination energy of an electron-hole pair is directly absorbed by a third carrier by Coulomb interaction rather than being transferred to the crystal lattice. The Auger recombination rate is directly proportional to the product of the concentrations of involved carriers and can be given as

$$R_n = \gamma_n n^2 p \text{ and } R_p = \gamma_p p^2 n \tag{5.16}$$

both for n-type and p-type semiconductor materials, respectively. The Auger coefficients γ_n and γ_p are elementary quantities of a semiconductor governing the least probable rates of non-radiative recombination. A large energy of the order of the bandgap E_G and a large momentum of the order of $\sqrt{2m_{eff}^* E_G}$ (m_{eff}^* is the effective mass of the charge particle) are generally transmitted to the third carrier involved in the recombination mechanism. As a result, only charge carriers with a large overall kinetic energy could participate in the direct Auger recombination mechanism. Therefore, there is always an existence of an

energy threshold (E_{th}) value for the Auger recombination process. The process

probability is directly proportional to $\exp\left(-\dfrac{E_{th}}{kT}\right)$.

Due to the existence of an energy threshold, the direct Auger recombination mechanism is prevalent only in case of narrow bandgap semiconductor materials. For other semiconductor materials, indirect Auger recombination process, which takes place via creating a defect center, is favorable. In case of the indirect Auger recombination process, which involves a single defect or bound state, there are four different classifications. The classifications are eeh_de, hhe_dh, ehe_de, and ehh_dh. Here e and h indicate free electrons and holes, e_d and h_d designate electrons and holes localized at the defect centers.
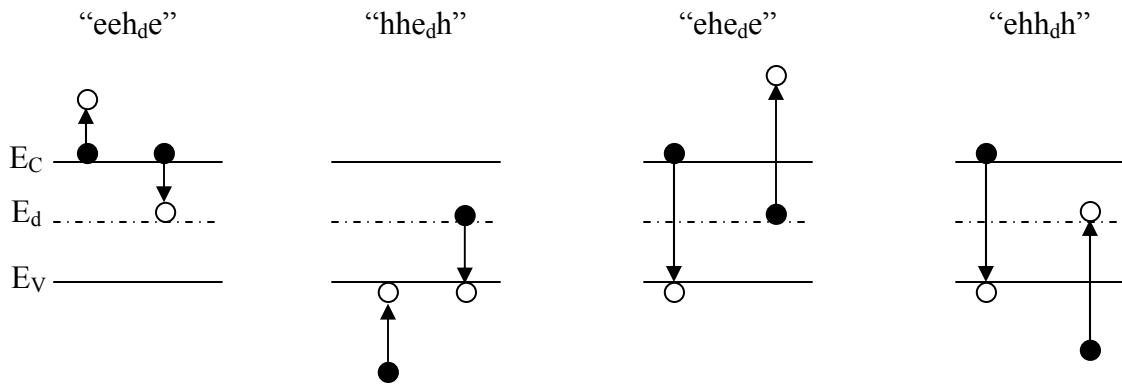
Fig. 5.1: Various indirect Auger recombination processes incorporating the creation of one localized defect state. Arrows denote the direction of electron transitions.

The first three letters indicate the charge carriers in the initial state and the fourth one is related to the charge carrier that receives the energy released due the recombination process. The indirect Auger recombination mechanism is pictorially depicted in Fig. 5.1.

The rate of Auger recombination is characterized by four Auger coefficients C_i (I = 1, 2, 3, 4):

$$R_1 = T_1 n^2 p_d, R_2 = T_2 p^2 n_d, R_3 = T_3 npn_d, \text{ and } R_4 = T_4 npp_d \qquad (5.17)$$

where p_d is the density of holes localized at acceptors and n_d is the density of electrons localized at donors. In order to carry out numerical evaluation of the Auger coefficients, the wavefunctions associated with the localized electrons and holes has to be calculated.

5.4.   Radiative Recombination

The radiative recombination rate is proportional to the product of the electron and the hole concentration of a semiconductor material. This phenomenon comes into consideration when the excitation carrier densities exceed the doping density. The radiative recombination rate is mathematically expressed as

$$R_r = Bn^2 \qquad (5.18)$$

where B is the radiative recombination constant. Typical range of B is ~ 8×10^{11} cm^3/sec for lead salt materials.

5.5.   Stimulated Recombination

The case of stimulated emission comes into the picture for a degenerate carrier system with quasi-Fermi energy levels shifted into the valence and conduction bands. By mathematical equation, the necessary condition for the occurrence of this phenomenon is given as:

$$E_f^C + E_f^V > 0 \tag{5.19}$$

where E_f^C and E_f^V are the quasi-Fermi energy levels of electrons and holes in conduction and valence band, respectively. The spontaneously emitted photons get amplified in the inverted sample. This results in an exponential rise in photon number and a decline in the carrier concentration. The stimulated emission decreases the carrier density quite efficiently. The reduction of the carrier concentration, however, is governed by the threshold value defined by equation (5.19). The photon amplification per length is represented as:

$$g(\hbar\omega) = \alpha_0(\hbar\omega)\left[1 - f_e\left(\frac{E_C - E_f^C}{kT}\right) - f_h\left(\frac{E_V - E_f^V}{kT}\right)\right] \tag{5.20}$$

If the excited carrier concentration is higher than the threshold condition for stimulate emission, the photons emitted spontaneously from the semiconductor material along a direction parallel to the surface would get amplified with high efficiency. This in turn reduces the density of carriers below threshold. The temporal development of the carrier concentration because of the presence of stimulated recombination is also expected to exhibit a threshold like characteristic.

5.6. Plasmon Recombination

This recombination mechanism is critically important for very high density values of excited charge carriers in the semiconductor materials. The plasmon energy, in general, exceeds the bandgap energy. The carrier recombination process takes place by

emission of plasmons. In lead chalcogenide materials such as PbSe and PbTe, carrier densities above 10^{19} cm^{-3} are required for an efficient plasmon recombination.[9] This value of carrier density is almost one order of magnitude higher than the highest excitation density considered in general lifetime measurement methods. For smaller plasmon energies, the recombination through this mechanism is insignificant.

5.7. Minority Carrier Lifetime Measurement by Photoconductive Decay (PCD) Method

The minority carrier lifetime is one of the key components influencing the opto-electronic properties of the semiconducting material. Various methods [10] [11] have been considered to measure carrier lifetime for IV-VI materials. Among these the photo-current decay (PCD) method, a popular scheme which is widely utilized in estimating carrier recombination lifetimes for many semiconductor materials and configurations[12] [13] [14] [15], is employed to evaluate the minority carrier lifetime in PbSe thin films grown on a BaF$_2$(111) substrate. In the PCD method, a constant current is passed through PbSe samples with the help of two gold ohmic contacts made on the PbSe sample itself. Excess carriers are generated by pulsed laser for a brief period of time. The photoconductivity change ($\Delta\sigma$), carrying the signature of minority carrier lifetime, is represented by a voltage drop (ΔV) on a fast cathode ray oscilloscope.

5.7.1. Fundamental Principle of PCD Method

In the actual experimental scheme, a constant current (I) is sent between two gold ohmic stripe contacts made separated by a distance, L, on the substrate, in our case on

PbSe sample. The dark voltage drop, i.e., the voltage drop across the sample when it is not excited by pulsed laser can be given by:

$$V_D = \frac{IL}{A\sigma_D} \; , \tag{5.21}$$

where σ_D is the dark conductivity of the sample, A is the area of cross-section on the sample through which current passes. When PbSe sample is illuminated by Q-switched laser, the sample conductivity is increased to σ due to the generation of excess carrier. Upon termination of pulsed laser illumination, the decay of voltage between the contacts (ΔV) is measured as a function of time as represented by:

$$\Delta V = \frac{IL}{A\sigma_D}\frac{\Delta\sigma}{\sigma} \; , \tag{5.22}$$

where $\Delta\sigma = \sigma - \sigma_D$ (5.23)

Under low-level injection, σ_D would be sufficiently large and $\Delta\sigma \ll \sigma_D$. Thus, the change in voltage drop, ΔV, would be controlled by the decay mechanism of $\Delta\sigma$ in time domain. The decay in $\Delta\sigma$ carries the signature of the exponential decay of minority carrier concentration, generated by laser excitation, to its thermal equilibrium value with a time constant τ. This τ represents the minority carrier lifetime of the semiconductor, comprised of three components:

$$\frac{1}{\tau} = \frac{1}{\tau_R} + \frac{1}{\tau_{NR}} + \frac{1}{\tau_S} = \frac{1}{\tau_R} + \frac{1}{\tau_{NR}} + \frac{2S}{t} \tag{5.24}$$

where τ_R is the radiative recombination lifetime, τ_{NR} is the non-radiative recombination lifetime (generally takes place via deep recombination centers), τ_S is the surface recombination lifetime, S is surface recombination velocity (SRV), and t is the thin film thickness. The PL decay curve therefore represents the total minority carrier lifetime, not only radiative lifetime (τ_R), for example.

5.7.2. Surface Passivation of PbSe

Epitaxial narrow bandgap IV-VI lead salt materials (such as PbSe) are popularly used to make infrared opto-electronic devices. The quality of thin-film surface preparation is critical to the fabrication and performance of such devices. It is well-known that surface impurities on the exposed area of thin films have damaging effects on the semiconducting behavior of such materials. One significant affect of such surface states is observed in the degradation of the spectral resolution of infrared photodetectors due to the occurrence of surface leakage current generated by the presence of conducting surface impurities. Other important factors which diminish device functionality are related to various surface noises[16]. These limitations could be avoided by covering the exposed material surface with a suitably thin passivation layer, one which is preferably lattice matched with the base material. Various chemical and electrochemical processes have already been developed to passivate different III-V and II-VI materials such as GaAs[17][18][19], InP[20], HgCdTe[21][22] etc. Surface passivation of PbSe by evaporating ZnSe is reported[23], but that surface treatment technique proved ineffective. Unlike III-V and II-VI materials, the effect of surface passivation on IV-VI semiconductor thin films has not been extensively studied.

In this chapter, we study the implementation of CaF_2 as a new surface passivation layer for MBE-grown PbSe single crystalline thin films on a BaF_2(111) substrate. Water-insoluble CaF_2 is chosen as the passivation layer due to its ease of epitaxial growth on PbSe thin films in the MBE. In addition, the CaF_2 passivated structure does not complicate the processing steps for device fabrication. The purpose of this study is to investigate the influence of surface passivation on the basic properties of semiconducting opto-electronic devices including photoluminescence (PL) intensity and minority carrier lifetime.

5.7.3. Sample Preparation

The growth of PbSe thin films on BaF_2(111) substrates are initiated via MBE growth of a thin (20 Å) buffer layer of CaF_2 (lattice constant = 5.44 Å). The substrate temperature is kept constant at 375 $^\circ$C, and the PbSe growth rate of 2.0 μm/h is maintained where, during the growth process, the Se to PbSe beam flux ratio is fixed at 10%. For this study, two p-type single-crystalline PbSe samples are grown on BaF_2(111) substrates with thicknesses of 4.5, and 6.5 μm. These samples are designated as Sample A and Sample B respectively.

In each MBE run, a set of seven samples are put inside the chamber for PbSe growth. Each time after the growth process is completed; all PbSe samples are taken outside of the MBE chamber. Three samples are kept in ultra-vacuum for future optical and electrical characterization related to this study and the remaining four samples are thoroughly blown by high purity N_2 gas and re-inserted into the MBE chamber in order to grow a thin (200 Å) CaF_2 passivation layer on the surface of the p-type PbSe thin films.

A chemical solution of de-ionized water and sulphuric acid (in the ratio of 40:1 by volume) is taken to remove the CaF_2 passivation layer on top of PbSe in order to make gold ohmic contacts.

5.7.4. Results and Discussion

Laser excitation of samples are performed using a 1.064 µm Q-switched Neodymium:Yttrium-Aluminium-Garnet (Nd:YAG) pulsed laser (τ_{pulse} = 30 ns, pulse repetition rate = 10Hz). The average excitation power on the sample surface used for optical measurement is 0.2 µW, and the spot-size diameter is focused to 4.0 mm on the sample. Considering that each photon of the pump laser creates a new electron-hole pair, the value of the initial average non-equilibrium excited carrier concentration (N_0) can be determined by[24]

$$N_0 = 0.65 \times \frac{\lambda E_P}{hc} \frac{4}{\pi r^2} (1-R) \frac{1-\exp(-\alpha d)}{d} \tag{5.25}$$

where the absorption coefficient (α) at the pumping wavelength (λ=1.064 µm) is 5×10^4 cm^{-1}, h is Planck's constant, c is light velocity in vacuum, and d is penetration depth of pump laser (in our case, $d \approx 1.0$ µm), E_p is lasing pulse energy. R is the reflection coefficient of thin film surface and can be calculated as

$$R = \left[\frac{n-1}{n+1} \right]^2 \tag{5.26}$$

where n is the relative refractive index of PbSe (n = 5). The value of initial excited carrier density (N_0) for Sample A is therefore calculated to be 1.2×10^{16} cm^{-3}. The carrier

mobility and bulk concentration at 77 K and 300 K are populated in Table-5.1. We consider that the smooth, thin passivation layer (200 Å) of CaF_2 would have negligible effect on the pump power absorption by PbSe samples.

Table-5.1: Carrier mobility and bulk concentration at 77 K and 300 K, and thickness of Sample A and Sample B.

Sample	Mobility $(cm^2.V.s)$ at 77 K	Mobility $(cm^2.V.s)$ at 300 K	Thickness (μm)	Bulk conc. (cm^{-3}) at 77 K	Bulk conc. (cm^{-3}) at 300 K
Sample A	6659.2	274.6	4.5	8.8×10^{16}	3.0×10^{17}
Sample B	6597.0	221.3	6.5	8.5×10^{16}	3.1×10^{17}

The lifetime measurement unit has a time resolution of 4 ns. In order to minimize measurement error in lifetime for a particular temperature, ten measurement data are taken for a single PbSe sample and the lifetime is represented by taking the average of those measurements. Fig. 5.2 represents the evaluation of minority carrier lifetime by the exponential fitting to the ΔV decay curve considered after the laser excitation stops. The lifetime values calculated for Sample A, with and without CaF_2 passivation, are 839.5±20.2 ns and 666.3±28.1 ns respectively at 77 K.
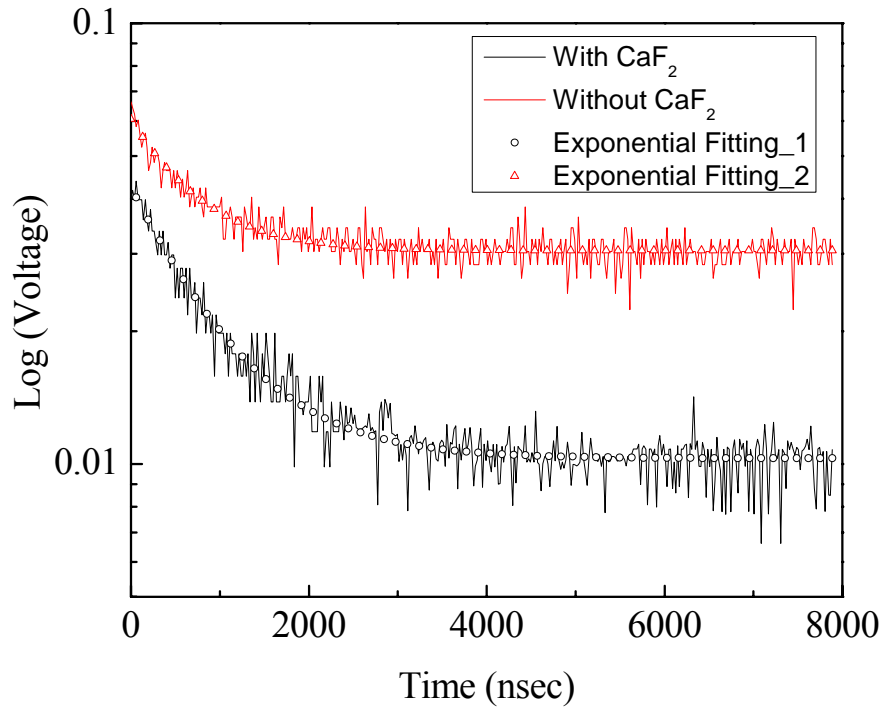
Fig. 5.2: Exponential fitting to voltage decay curve before and after CaF₂ surface passivation and thereby calculating minority carrier lifetime.

The effect of CaF_2 passivation on minority carrier lifetime for both PbSe samples at various temperatures is illustrated in Fig. 5.3. The improvement in minority carrier lifetimes after surface passivation is comparatively more significant at low temperature than at high temperature values. Even if the lifetime improvement after surface passivation is well within error margin at elevated temperature, there is a consistent trend of increasing lifetime due to CaF_2 passivation.
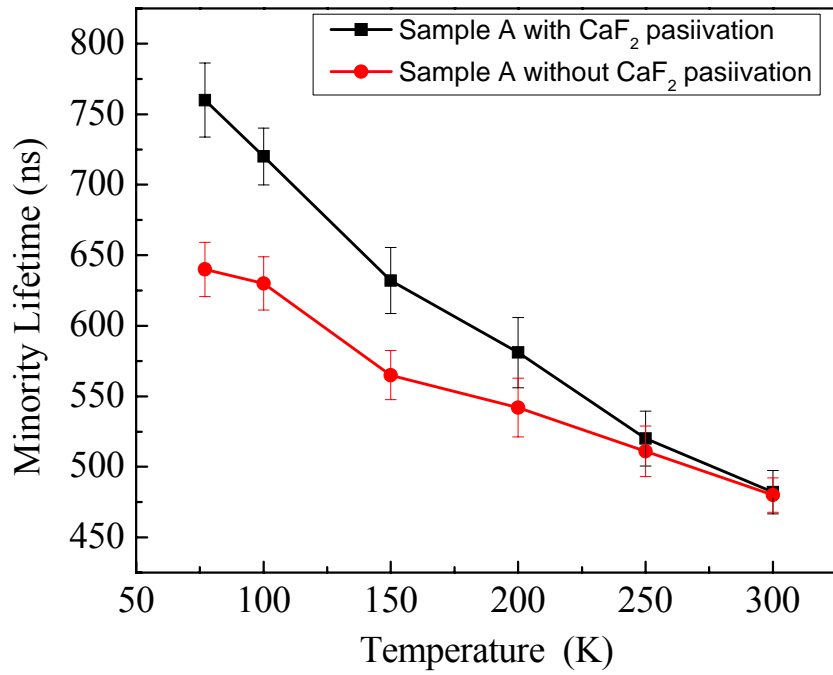
(a)
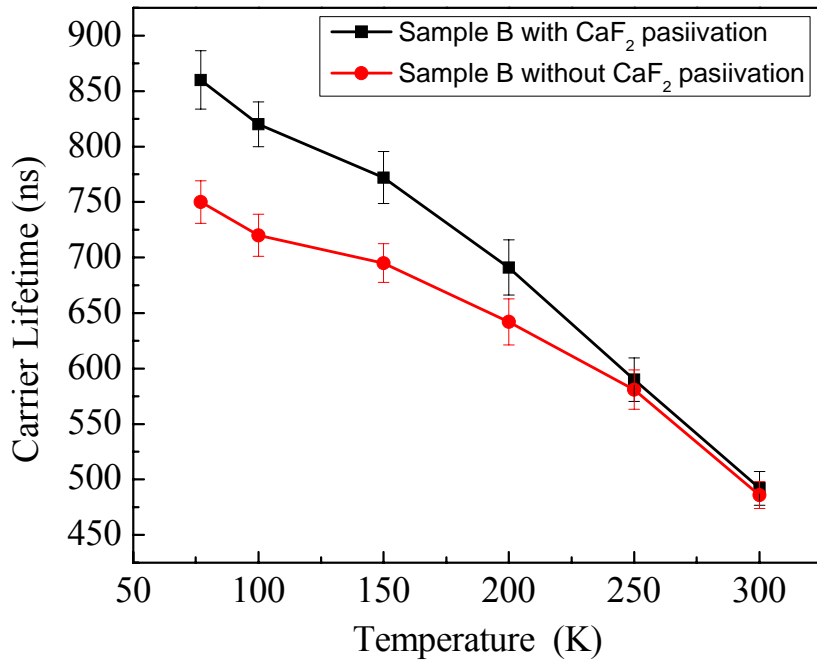
(b)

Fig. 5.3: Minority carrier lifetimes measured by PCD method before and after CaF$_2$ passivation at various temperatures for (a) Sample A, and (b) Sample B.

The lasing power density used to carry out the optical characterization for PbSe samples is 44.31 kW/cm^2. The spontaneous emission emanating from the sample is made to fall on a Kolmar liquid nitrogen-cooled photovoltaic mercury cadmium telluride (MCT) detector equipped with a fast pre-amplifier. With the help of Fourier transform infrared (FTIR) spectrometer, time-resolved infrared spectra are recorded in step-scan mode by using PAD 82a transient digitizer board. The photoluminescence (PL) spectra is calculated at an optical resolution of 16 cm^{-1} and co-added four times. The PL measurements are performed at various heat sink temperatures from 77 K to 300 K in steps; spontaneous emissions from both thin-film samples with and without passivating layers are compared. It is noteworthy that the optical measurement parameters were kept constant in regards to characterizing one sample with a passivation layer and comparing the result with its non-passivated counterpart. Fig. 5.4 shows the pulsed photoluminescence from both PbSe samples at various temperatures, both before and after CaF$_2$ surface passivation.
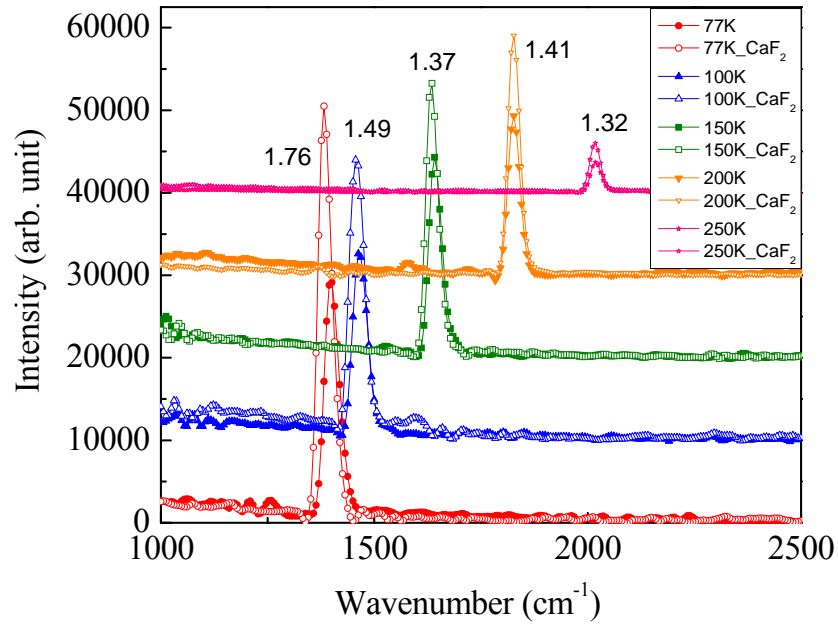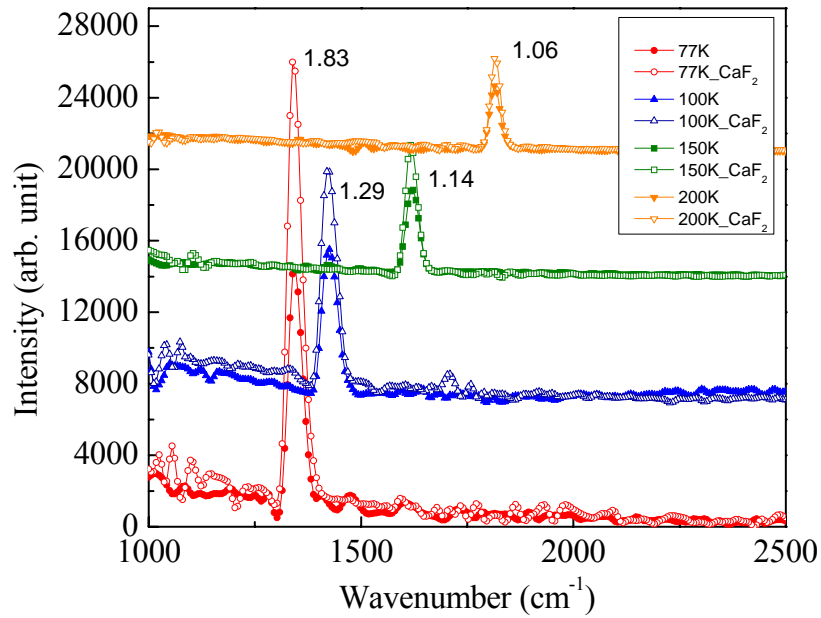
Fig. 5.4: PL intensity from PbSe epilayers on a BaF$_2$-substrate with and without CaF$_2$ passivation at various temperatures for (a) Sample A, and (b) Sample B.

Pulsed PL intensity from the PbSe samples increases after surface passivation for both samples. For example, from Fig. 5.4(a), the increment in PL intensity from Sample A shows a maximum improvement of 1.76 times at 77 K after CaF_2 passivation. The PL enhancement reduces steadily with the increase in heat-sink temperature. The PL intensity at 300 K, however, is quite weak and does not show improvement after passivation. Similarly, Sample B demonstrates a 1.83-fold enhancement in PL intensity at 77 K after passivation and the improvement gradually reduces with temperature as shown in Fig. 5.4(b). Light extraction efficiency [25] from PbSe sample is calculated to be 1.12%, whereas that from CaF_2-passivated sample is only 0.80%. Therefore calibrated enhancement should be an enhancement in PL intensity after surface passivation.

From the measurement results, the effect of surface passivation on minority carrier lifetime and PL intensity of PbSe thin film samples is comparatively more significant at low values of heat-sink temperature than at high temperature. In principle, the values of radiative and non-radiative lifetime are not influenced by the introduction of CaF_2 as a passivating layer. As seen from Fig. 5.3, surface recombination velocity, which is inversely proportional to lifetime (as from equation 4), is the only parameter that is improved after passivation. The influence of surface states on lifetime is minimized by CaF_2 passivation, the effect of which is demonstrated by improved minority carrier lifetimes as well as PL intensities from the passivated thin film samples. Thus surface passivation for lead salt material is critically important, especially at low temperature, in regards to device fabrication as is the case with II-VI, and III-V materials. Further studies will involve growing a thin CaF_2 passivation layer on PbSe epilayer grown on Si substrate.

5.8. Conclusions

A study the effects of CaF_2 surface passivation on minority carrier lifetime and PL intensity from PbSe thin films grown on BaF_2 substrates at various heat-sink temperatures is reported. Results of a PCD study on the measurement of minority carrier lifetime in PbSe are described. Minority carrier lifetimes (τ) and pulsed photoluminescence intensities are increased after surface passivation for both samples. However, the improvement is comparatively more significant at low temperature than at high temperature. This may indicate that surface passivation for Pb-salt materials are not as critical as its II-VI and III-V counterparts at high temperature of device operation. Therefore, device fabrication for Pb-salt materials at elevated temperature could be relatively more cost-effective with a higher-yield.

5.9.   References

[1] R.N. Hall, "Electron-Hole Recombination in Germanium," *Phys. Rev.*, vol. 87, pp. 387, 1952.

[2] W. Shockley and W. T. Read, "Statistics of the Recombinations of Holes and Electrons," *Phys. Rev.*, vol. 87, pp. 835–842, 1952.

[3] R. N. Hall, "Recombination Processes in Semiconductors," *Proc. IEE*, vol. 106B, pp. 923–931, 1960.

[4] D. K. Schroder, "The Concept of Generation and Recombination Lifetimes in Semiconductors," *IEEE Trans. Electron Dev.*, vol. ED-29, pp. 1336–1338, 1982.

[5] R. Klann, T. Hofer, R. Buhleier, T. Elsaesser, J. W. Tomm, "Fast recombination processes in lead chalcogenide semiconductors studied via transient optical nonlinearities," *J. Appl. Phys.*, vol. 77, pp. 277-286, 1995.

[6] V. N. Abakumov, V. I. Perel, and I. N. Yassievich, "Nonradiative recombination in semiconductors," North-Holland, Amsterdam, 1991.

[7] W. Shockley and W. T. Read, "Statistics of the Recombinations of Holes and Electrons," *Phys. Rev.*, vol. 87, pp. 835-842, 1952.

[8] G. Nimtz, "Recombination in narrow-gap semiconductors," *Phys. Rep.*, vol. 63, pp. 265-300, 1980.

[9] M. Mocker and O. Ziep, "Intrinsic recombination in dependence on doping concentration and excitation level," *Phys. Stat. Sol. B*, vol. 115, pp. 415-425, 1983.

[10] J. W. Tomm, K. H. Herrmann, H. Bottner, M. Tacke, and A. Lambrecht, "A luminescence study in the $Pb_{1-x}Eu_xSe$ system," *Phys. Stat. Sol. A*, vol. 119, pp. 711-719, 1990.

[11] P. Berndt, D. Genzow, K. H. Herrmann, "Recombination analysis in 10 mu m $Pb_{1-x}Sn_xTe$," *Phys. Stat. Sol.A*, vol. 38, pp. 497-503, 1976.

[12] C. H. Wang, K. Misiakos, and A. Neugroschel, "Minority-carrier transport parameters in n-type silicon," *IEEE Transac. Elec. Dev.*, vol. 37, 1314-1322, 1990.

[13] B. Schlicht, R. Dornhaus, G. Nimtz, L. D. Haas, T. Jakobus, "Life time measurements in PbTe and PbSnTe," *Sol. Stat. Elec.*, vol. 21, pp. 1481-1485, 1978.

[14] L. X. He, K. P. Martin, and R. J. Higgins, "Persistent photocurrent decay mechanisms by capture of photoelectrons in GaAs-$Al_xGa_{1-x}As$ heterostructures," *Phys. Rev. B*, vol. 36, pp. 6508-6519, 1987.

[15] D. E. Ioannou, "SEM-EBIC and traveling light spot diffusion length measurements: normally irradiated charge-collecting diode," *IEEE Transac. Elec. Dev.*, vol. ED-30, pp. 577-580, 1983.

[16] K. Chattopadhyay, M. Hayes, J. -O. Ndap, A. Burger, W. J. Lu, H. G. McWhinney, T. Grady, and R. B. James, "Surface passivation of cadmium zinc telluride radiation detectors by potassium hydroxide solution," *J. Elec. Mat.*, vol. 29, pp. 708-712, 2000.

[17] J. Yota and V A. Burrows, "Chemical and electrochemical treatments of GaAs with Na_2S and $(HN_4)_2S$ solutions: a surface chemical study," *J. Vac. Sci. Technol. A*, vol. 11, pp. 1083-1088, 1993.

[18] V. N. Bessolov, A. F Ivankov, E. V. Konenkova, M. V Lebedev, and V. S. Strykanov, "Kinetics of GaAs (100) surface passivation in aqueous solutions of sodium sulfide," *Semincond.*, vol. 30, pp. 201-206, 1996.

[19] X. Y. Hou, W. Z. Cai, Z. Q. He, P H. Hao, Z. S. Li, X. M. Ding, and X. Wang, "Electrochemical sulfur passivation of GaAs," *AppI. Phys. Lett.*, vol. 60, pp. 2252-2254, 1992.

[20] L. J. Gao, J. A. Bardwell, Z. H. Lu, M. J. Graham, and P R. Norton, "Anodic passivation of p-InP (100) in (NH4)2Sx solution," *J. Electrochem. Soc.*, vol. 142, pp. L14-L16, 1995.

[21] J. P Ziegler, J. M. Lindquist, and J. C. Hemminger, "The interface chemistry of HgCdTe passivated with native sulfide layers grown from nonaqueous and aqueous polysulfide solutions," *J. Vac. Sci. Technol. A*, vol. A7, pp. 469-473, 1989.

[22] T. Ipposhi, K. Takita, K. Masuda, H. Kudo, and S. Seki, "Hg content and thermal stability of the anodic sulfide films on $Hg_{1-x}Cd_xTe$ investigated by 30-40-MeV O^{5+} ion backscattering," *J. Appl. Phys.*, vol. 63, pp. 132-135, 1988.

[23] P. Collot, F. Nguyen-Van-Dau, V. Mathet, "Monolithic integration of PbSe IR photodiodes on Si substrates for near ambient temperature operation," *Semicond. Sci. Technol.*, vol. 9, pp. 1133-1137, 1994.

[24] J. O. Drumm, B. Vogelgesang, G. Hoffmann, C. Schwender, N. Herhammer, and H. Fouckhardt, "Temperature and carrier density dependence of Auger recombination in a 3.4 μm InAs/GaSb/AlSb type-II laser device," *Semicond. Sci. Technol.*, vol. 17, pp. 1115-1122, 2002.

[25] S. M. Sze, "Physics of Semiconductor Devices," 2nd edition, p694, , Wiley, New York, 1981.

CHAPTER 6

SUMMARY AND FUTURE WORK

6.1. Summary

The research elaborated by this dissertation has described a theoretical model which evaluates gain from the quantum well structure based on IV-VI lead salt semiconductor material in the second chapter. The calculation is carried out utilizing the very popular Kane's double band model. The modal gain of the QW structure, with both for finite and infinite well, for different growth orientation is calculated by keeping the injected sheet carrier charge density as constant. The carrier effective masses at L points in the Brillouin zone along [100], [110], and [111] orientations are implemented in generating modal gains for the respective QW orientations. The subband energy levels together with the corresponding quasi Fermi energy levels are evaluated and plotted for a specific orientation and QW parameters.

The modern epitaxial technology that allows high quality alternating material growth and advanced laser concepts is resurrecting IV-VI mid-IR lasers. The [110] and [111] orientated QW laser structure combined with much improved substrate thermal conductivity as well as the low Auger recombination promise the success of the lead-salt mid-IR lasers. The third chapter described some work in the domain of recent developments of IV-VI lead salt light emitting devices. An electrically excited QW laser on [110] oriented lead salt substrate is described for the first time in the literature.

Fabrications of novel microstructures in the form of rod, tube and pillar, having enormous applications in MEMS and NEMS, are reported.

In the fourth chapter, a theoretical investigation of spontaneous mid-infrared emission from IV-VI semiconductor defect cavity in the hexagonal photonic crystal is elaborated in this chapter. The design is aimed to solve out challenges of the formation of resonating cavity for lead salt materials fabricated on Si(111) or BaF_2(111) substrates. The band structure calculations of the periodic crystal are performed using PWE method. FD perturbation correction method and FDTD algorithms have been implemented to analyze and understand modal field distribution in the defect cavity. These are very popular and well-established mathematical tools for optical waveguide analysis. FDTD results reasonably tally with the simulation results by FD perturbation method. By thorough and accurate calculation, a single TM-like mode is achieved at 4.17 µm, having an optimized Q-factor of 5200, resonates in the designed defect cavity.

The fifth chapter describes a study concerning the effects of CaF_2 surface passivation on minority carrier lifetime and PL intensity from PbSe thin films grown on BaF_2(111) substrates. Minority carrier lifetimes and pulsed photoluminescence intensities from PbSe samples are increased after CaF_2 surface passivation. However, the improvement is comparatively more significant at low temperature than at high temperature. This may indicate that surface passivation for Pb-salt materials are not as critical as its II-VI and III-V counterparts at high temperature of device operation. Therefore, device fabrication for Pb-salt materials at elevated temperature could be relatively more cost-effective with a higher-yield.

6.2. Future Work

The laser emission from the [110] lead chalcogenide MQW structure is multi-modal. Moreover, the highest heat sink temperature at which the lasing could be achieved is 158 K. In order to do away with multi-modal emissions, narrow stripe contact in the range of 5 - 10 µm could be considered. Formation of a cleaved Fabry-Perot cavity on a BaF_2 substrate which has larger thermal conductivity than Pb-salt materials has been demonstrated by our group. These BaF_2 substrates could be extensively implemented as a growth substrate in order to realize high temperature infrared devices in future.

A theoretical study regarding the formation of photonic crystal defect cavity on lead salt materials has been conducted. The motivation is to demonstrate high temperature continuous wave lasing emission from laser structure based on silicon substrates. Further theoretical study covering the three dimensional laser structure is required in order to precisely calculate the modal pattern and other relevant parameters of the laser emission from the PC structure. More experimental studies could be conducted to realize these lead-salt based PC devices for real world applications.

A thorough analysis regarding the measurement of minority carrier lifetime of PbSe samples grown on $BaF_2(111)$ is elaborated. Photoconductive decay method has been implemented to carry out the lifetime measurements of the samples at various heat sink temperatures. A study on the effects of CaF_2 surface passivation is carrier out. A similar study of surface passivation on lead chalcogenide materials on Si substrate is needed. Moreover, the effect of surface passivation by other materials such as Si_3N_4 could be considered. The minority carrier lifetime measurement set-up established during

this study could be utilized to measure carrier lifetimes for future laser and detector materials.

APPENDIX I

ACRONYMS

APSYS Commercial software, written by the CROSSLIGHT Inc., for solving numerical simulations for QW structure

BMS Beam splitter

CB Conduction band

CMP Chemical mechanical polishing

CW Continuous wave

DBR Distributed Bragg reflector

DFT Discrete Fourier transform

DH Double heterostructures

DI De-ionized

DOS Density of states

FD Finite difference

FDM Finite difference method

FDTD Finite difference time domain

FET Field effect transistor

FTIR Fourier transform infrared

FWHM Full width at half maximum

GMCW Gaussian modulated continuous wave

HRXRD High reflection X-ray diffraction

IC Integrated circuit

IR Infrared

LPE Liquid phase epitaxy

MBE Molecular beam epitaxy

MCT Mercury-Cadmium-Telluride

MEMS Micro-electromechanical systems

MIR Mid-infrared

MOCVD Metal organic chemical vapor deposition

MQW Multiple quantum well

NDA Non disclosure agreement

Nd:YAG Neodymium:Yttrium-Aluminium-Garnet

NEMS Nano-electromechanical systems

Opti-FDTD Commercial software, written by the Optiwave Company, for solving Maxwell's equations by the finite difference time domain method

OU University of Oklahoma

PBG Photonic bandgap

PC Photonic crystal

PCD Photoconductive decay

PL Photoluminescence

PRF Pulse repetition frequency

PWE Plane wave expansion

QC Quantum cascade

QW Quantum well

RHEED Reflection high energy electron diffraction

SEM Scanning electron microscope

SQW Single quantum well

SQW-GRINSCH Single quantum well graded index separate confinement heterostructures

SRH Shockley-Read-Hall

3D Three-dimensional

TE Transverse electric polarization

TEM Transverse electro-magnetic

TM Transverse magnetic polarization

2D Two-dimensional

VB Valence band

VCSEL Vertical cavity surface emitting laser

VPE Vapor phase epitaxy

APPENDIX II

LIST OF PUBLICATIONS

Listed below are publications that took place during my stay at the University of Oklahoma.

BOOK/BOOK CHAPTER

1. **Shaibal Mukherjee**, Shelly L. Elizondo, Lee A. Elizondo, and Zhisheng Shi, "Recent developments of PbSe-based IV-VI semiconductor quantum well structures," in press, Invited author of a chapter for the book "**Quantum Wells: Theory, Fabrication and Applications**," NOVA Publisher, ISBN: 978-1-60692-557-7, 2009.

2. **Shaibal Mukherjee**, Donghui Li, and Zhisheng Shi, "IV-VI light emitting devices," Book, to be submitted, Research Signpost, 2009.

INVITED JOURNAL REVIEW PAPERS

1. **Shaibal Mukherjee**, Zhisheng Shi, "State-of-the-art IV-VI Semiconductor Light-Emitting Devices in Mid-Infrared Opto-Electronic Applications," *IETE Technical Review*, vol. 26, pp. 236-245, 2009.

2. **Shaibal Mukherjee**, Pallabi Mukherjee, Musharraf Zaman, "Comparative Study of Engineering Annual Research Expenditures in Selected Big 12 Universities – A Review from USA," under peer review, *IETE Technical Review*, 2009.

JOURNAL PAPERS

1. **S. Mukherjee**, A. Gautam, Z. Q. Li, S. Li, S. L. Elizondo, and Z. Shi, "Accurate Calculation of PbSe-PbSrSe QW Gain for Different Crystal Orientations," to be communicated to *Physical Review B*, 2009.

2. **S. Mukherjee**, D. Li, G. Bi, J. Ma, A. Gautam, S. L. Elizondo, F. Zhao, G. Yu, B. Weng and Z. Shi, "CaF$_2$ surface passivation of lead selenide grown on BaF$_2$," under peer review, *Applied Physics Letters*, 2009.

3. A. Gautam, **S. Mukherjee**, and S. Ram, "Controlled novel route to synthesis and characterization of silver nanorod," in press, *Journal of Nanoscience and Nanotechnology*, 2009.

4. **Shaibal Mukherjee**, Gang Bi, Jyoti P. Kar, and Zhisheng Shi, "Two dimensional numerical analysis on mid-infrared emission from IV-VI lead salt photonic crystal microcavity," in Press, *Optica Applicata*, 2009.

5. D. Li, **S. Mukherjee**, J. Ma, G. Bi, D. Ray, F. Zhao, S. L. Elizondo, G. Yu and Z. Shi, "Edge-Emitting Lead Salt Mid-Infrared Laser Structure on BaF$_2$ [110] Substrate," in press, *Journal of Electronic Materials*, 2009.

6. D. Li, J. Ma, **S. Mukherjee**, B. Gang, F. Zhao, S. L. Elizondo, and Z. Shi, "A new in-situ surface treatment during MBE-grown PbSe on CaF$_2$/Si(111) heterostructure," *Journal of Crystal Growth*, vol. 311, pp. 3395-3398, 2009.

7. J. Ma, D. Li, G. Bi, F. Zhao, S. Elizondo, **S. Mukherjee**, and Z. Shi, "Nature of growth pits in lead salt epilayers grown by molecular beam epitaxy," *Journal of Electronic Materials*, vol. 38, no. 2, pp. 325-329, 2009.

8. J. P. Kar, G. Bose and S. Tuli, A. Dangwal, **S. Mukherjee**, "Growth of AlN films and its process development for the fabrication of acoustic devices and micromachined structures," in press, *Journal of Materials Engineering and Performance*, 2009.

9. J. P. Kar, **S. Mukherjee**, G. Bose and S. Tuli, "Impact of post-deposition annealing on the surface, bulk and interface properties of RF sputtered AlN films," in press, *Materials Science and Technology*, 2009.

10. **S. Mukherjee**, D. Li, D. Ray, F. Zhao, S. L. Elizondo, S. Jain, J. Ma, and Z. Shi, "Fabrication of an Electrically Pumped Lead-Chalcogenide Mid-Infrared Laser on a [110] Oriented PbSnSe Substrate," *IEEE Photonics Technology Letters*, vol. 20, no. 8, pp. 629-631, 2008.

11. F. Zhao, **S. Mukherjee**, J. Ma, D. Li, S. L. Elizondo, and Z. Shi, "Influence of oxygen passivation on optical properties of PbSe thin films," *Applied Physics Letters*, vol. 92, no. 211110, pp. 1-3, 2008.

12. X. J. Wang, C. Fulk, F. Zhao, D. Li, **S. Mukherjee**, Y. Chang, R. Sporken, R. Klie, Z. Shi, C. H. Grein, and S. Sivananthan, "Characterization of PbSnSe/CdTe/Si (211) Epilayers Grown by Molecular Beam Epitaxy," *Journal of Electronic Materials*, vol. 37, no. 9, pp. 1200-1204, 2008.

13. **S. Mukherjee**, S. Jain, F. Zhao, J. P. Kar, D. Li, and Z. Shi, "Strain oriented microstructural change during the fabrication of free-standing PbSe micro-rods," *Journal of Materials Science: Materials in Electronics*, vol. 19, pp. 237-240, 2008.

14. **S. Mukherjee**, S. Jain, F. Zhao, D. Li, J. P. Kar, and Z. Shi, "Enhanced photoluminescence from free-standing microstructures fabricated on MBE grown PbSe – PbSrSe MQW structure," *Journal of Microelectronic Engineering*, vol. 85, pp. 665-669, 2008.

15. J. P. Kar, G. Bose, S. Tuli, J. M. Myoung, and **S. Mukherjee**, "Morphological investigation of aluminum nitride films on various substrates for MEMS applications," in press, *Journal of Surface Engineering*, 2008.

16. S. Elizondo, F. Zhao, J. Kar, J. Ma, J. Smart, D. Li, **S. Mukherjee**, and Z. Shi, "Dielectric Charge Screening of Dislocations and Ionized Impurities in PbSe and MCT," *Journal of Electronic Materials*, vol. 37, no. 9, pp. 1411-1414, 2008.

17. J. P. Kar, **S. Mukherjee**, G. Bose, S. Tuli, "Effect of inter-electrode spacing on structural and electrical properties of RF sputtered AlN films," *Journal of Materials Science: Materials in Electronics*, vol. 19, pp. 261-265, 2008.

18. **S. Mukherjee**, S. Jain, F. Zhao, J. P. Kar, and Z. Shi, "Photoluminescence studies from micropillars fabricated on IV-VI multiple quantum-well semiconductor structure," *Journal of Microelectronics*, vol. 38, pp. 1181-1184, 2007.

19. S. Jain, **S. Mukherjee**, Z. P. Guan, D. Ray, F. Zhao, D. Li, and Z. Shi, "Fabrication of free-standing PbSe micro-rods," *Physica E*, vol. 39, pp. 120-123, 2007.

20. L. A. Elizondo, Y. Li, A. Sow, R. Kamana, H. Z. Wu, **S. Mukherjee**, F. Zhao, Z. Shi and P. J. McCann, "Optically Pumped Mid-Infrared Light Emitter on Silicon," *Journal of Applied Physics*, vol. 101, no. 104504, pp. 1-6, 2007.

21. A. Majumdar, Z. P. Guan, F. Zhao, D. Li, D. Ray, S. Jain, **S. Mukherjee**, and Z. Shi, "Fabrication of freestanding semiconductor multiple quantum-well microtubes," *Applied Physics Letters*, vol. 88, no. 171111, pp. 1-3, 2006.

CONFERENCE PAPERS/POSTERS

1. Gang Bi, Fanghai Zhao, Jiangang Ma, **Shaibal Mukherjee**, Donghui Li, and Zhisheng Shi, "Modelling of the potential profile for the annealed polycrystalline PbSe film," Progress in Electromagnetic Research Symposium (*PEERS) 2009*, Beijing, China, March 23-27, 2009.

2. **Shaibal Mukherjee**, Pallabi Mukherjee, "A Comparative Analysis of Engineering Research Expenditures in Selected Big 12 Universities," *2008 American Society for Engineering Education (ASEE) Midwest Section Annual Conference*, University of Tulsa, OK, September 17-19, 2008.

3. F. Zhao, **S. Mukherjee**, J. Ma, D. Li, S. Elizondo, G. Bi, Z. Shi, "Influence of oxygen passivation on optical and electrical properties of PbSe thin films," 2008 U.S. Workshop on the Physics and Chemistry of II-VI Materials, The American Physical Society, Las Vegas, Nevada, United States, November 11-13, 2008.

4. D. Li, J. Ma, G. Bi, **S. Mukherjee**, F. Zhao, S. Elizondo, Z. Shi, "Influence Growth defects and In-situ surface treatments of epitaxially grown PbSe on silicon," 2008 U.S. Workshop on the Physics and Chemistry of II-VI Materials, The American Physical Society, Las Vegas, Nevada, United States, November 11-13, 2008.

5.   L. A. Elizondo, P. J. McCann, S. L. Elizondo, F. Zhao, **S. Mukherjee**, Z. Shi, J. C. Keay, and M. B. Johnson, "Quantum Effects in IV-VI Semiconductor Nanostructures," *University of Oklahoma Research and Performance Day*, Norman, OK, March 29, 2008.

6.   L. A. Elizondo, P. J. McCann, S. L. Elizondo, F. Zhao, **S. Mukherjee**, Z. Shi, J. C. Keay, and M. B. Johnson, "Quantum Effects in IV-VI Semiconductor Nanostructures," *Oklahoma EPSCoR, NanoFocus & NSF EPSCoR – Annual State Conference*, Oklahoma City, OK, March 6–7, 2008.

7.   **S. Mukherjee**, S. Jain, J. P. Kar, F. Zhao, and Z. Shi, "Superior performances from fabricated microstructures on MBE-grown IV-VI lead salt materials for mid-infrared applications," *proceedings of IEEE Express, 14th International Workshop on the Physics of Semiconductor Devices (IWPSD)*, Mumbai, India, December 16-20 , 2007.

8.   **S. Mukherjee**, "Novel semiconductor microstructures for mid-infrared applications," *poster presentation, Graduate Student Research and Creativity Endeavors/poster session*, University of Oklahoma, Norman, April 6, 2007.

9.   S. Jain, **S. Mukherjee**, Z. P. Guan, D. Ray, F. Zhao, D. Li, and Z. Shi, "Fabrication of Free-standing micro and nano objects from epitaxially grown PbSe film," *International Congress of Nanotechnology*, Sacramento, CA (USA), November 1, 2006.

10. D. Ray, Z.P. Guan, F. Zhao, S. Jain, **S. Mukherjee**, D. Li, and Z. Shi, "Antireflection Coating for Photo-Pumped IV-VI Semiconductor Light Emitting Devices," *proceedings of SPIE*, October 13, 2006.